Doctoral Dissertation

Real-Time Future Response Predictions Considering Multiple Floating Bodies Based on Kalman Filter Algorithm: A Digital Twin Application for Offshore Wind-Farm

（カルマンフィルタを用いた複数浮体応答のリアルタイム将来予測 ～デジタルツイン技術のウィンドファームへの応用～）

Rodhiatul Isnaini (28J20824)
Supervisor: Prof. Kazuhiro Iijima

Committee members:

飯島　一博（主査）
大沢　直樹
千賀　英敬

June 2023

Department of Naval Architecture and Ocean Engineering
Division of Global Architecture
Graduate School of Engineering
Osaka University

Abstract

The current study examines the potential of forecasting future waves and responses by expanding the Kalman filter algorithm through the inclusion of spatial distance between two points. The proposed idea is projected to be implemented as a part of the digital twin of a wind farm. However, before the future predictions are investigated, the Kalman filter algorithm feasibility to be utilized at floating offshore wind turbine is scrutinized. The Kalman filter works by estimating the coefficients of elementary waves by incorporating response data from a floating offshore wind turbine (FOWT). In this algorithm, the state variables are defined as the coefficients of elementary waves, while the FOWT's responses are used as the observed data. The observation matrix in the algorithm is determined based on the response transfer functions. Two different designs of semisubmersible FOWT structures are chosen as the subject structures for the first part of the study. Here, the impact of different types and locations of measurements on the accuracy of wave prediction generated by the filter is examined. The discussion also addresses the effects of nonlinearity resulting from the combined load of wind and waves. Overall, it can be concluded that the algorithm's performance heavily relies on the transfer functions employed in all the analyzed case study. After confirming the algorithm workability in the context of FOWT, an experiment on a 2D tank using simplified floating models is carried out to confirm the effectiveness of the Kalman filter based future predictions after spatial distance between two points is introduced. When the causality limitation is met, it is discovered that the model can predict future waves in the range of 3-10 s or several wave cycles ahead, depending on the distance between the points. By adopting a scaling factor of 1/100, this translates to an estimation of waves occurring 30-100 s ahead. The predictive time for future waves increases as the distance between the points becomes greater. Additionally, the study investigates response predictions using wave prediction data. The results demonstrate high accuracy in response prediction, with an even longer forecasted future time (80-120 s ahead, given a 1/100 scale ratio) compared to the predicted future time for waves.

Table of contents

List of Figures

List of Tables

Chapter 1
Introduction

1.1 Background

Wind energy is a more well-established renewable energy source compared to other resources alongside with solar, particularly in terms of its technological advancements (IRENA, 2019). While onshore wind energy technology is more mature, offshore wind energy has gained increasing interest due to its numerous advantages (Ellabban, Abu-Rub, & Blaabjerg, 2014; Esteban, Diez, López, & Negro, 2011; Esteban, López-Gutiérrez, & Negro, 2020). Compared to onshore wind farms, offshore wind farms offer benefits such as greater wind resources and reduced visual impact. Currently, bottom-fixed foundations are commonly used for offshore wind turbines. However, as wind farms move towards deeper waters, floating foundations are expected to become more prevalent (Sánchez, López-Gutiérrez, Negro, & Esteban, 2019; Wu, et al., 2019). Despite the advantages of deeper water wind cultivation, floating offshore wind turbines (FOWTs) face challenges, particularly in terms of economics (Tillenburg, 2021; Ciuriuc, Rapha, Guanche, & Domínguez-García, 2022). The installation costs of FOWTs are significantly influenced by operation expenditures, with operation and maintenance (O&M) expenses accounting for a significant portion of the total cost (Butterfield, Musial, Jonkman, & Sclavounos, 2005; Castellà, 2020). The installation and operation of FOWTs are complex tasks due to factors such as site accessibility and design intricacies.

The concept of a digital twin (DT) system is expected to be employed to enhance safety and operational efficiency throughout the various stages of implementing a floating offshore wind farm. The concept of DT was first introduced by Grieves in 2003 and aims to monitor the real-time status of a physical system by utilizing data from sensors and feeding it into a digital representation of the system (Wang, et al., 2021). Several reports have explored the technical aspects of applying DT technology to offshore wind turbines (Ciuriuc, Rapha, Guanche, & Domínguez-García, 2022; Wang, et al., 2021). It has become evident that a crucial component in developing a robust digital twin is the algorithm used to process the collected data and make predictions about important parameters. In this case, an algorithm capable of identifying environmental conditions, particularly the incident wave, plays a vital role. The wave prediction needs to be performed in real-time and should be both reliable and efficient. To provide a solution to this problem, estimation of the coefficients for regular waves based on the

assumption that the wave can be decomposed into a Fourier series of regular waves using Kalman filter is proposed in this study. Later on, this information is used for future predictions at x away. Structural responses are incorporated, and an inverse problem approach is employed to estimate the incident wave by utilizing transfer functions (TFs). The state variables in the Kalman filter are defined as the coefficients of the elementary waves, while the measurement data serve as the observation variables. Transfer functions are employed to describe the observation matrix within the Kalman filter algorithm and are predetermined. More details about the Kalman filter algorithm are provided in Chapter 2. Additionally, to provide further context, Figure 1.1 is given to provide the idea of DT for wind farm conceptualized by the author. This dissertation only focuses on the future wave and response predictions indicated by the red box on the aforementioned figure.

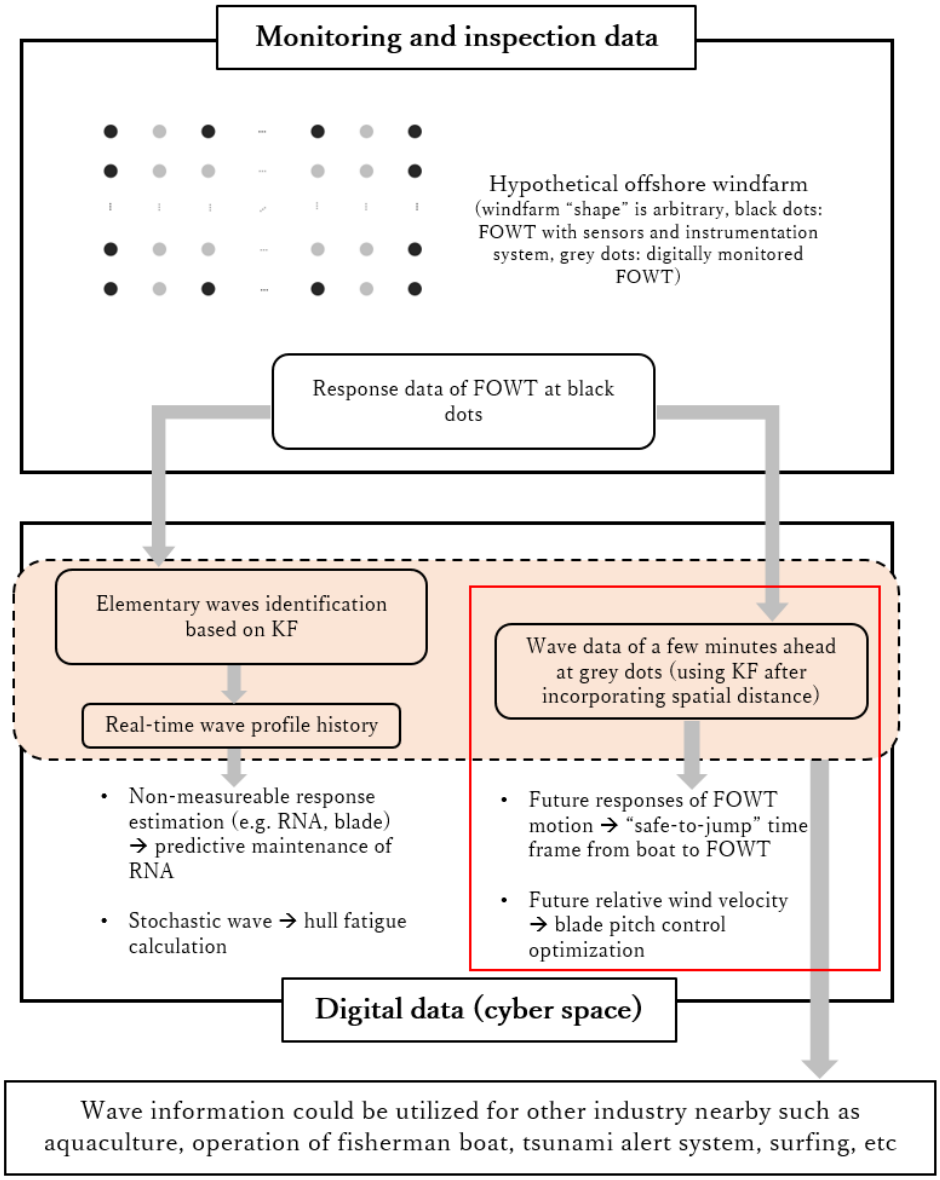

Figure 1. 1 The proposed concept of DT for wind farm

As stated above, a real-time wave prediction using Kalman filter is carried out in this study. However, the main goal of this study is to investigate the feasibility of finding future predictions (wave and response) when the Kalman filter algorithm is extended. The Kalman filter provides real-time wave history at a reference point, which can be used to predict future waves at other points based on spatial distance. Figure 1.3 is provided to illustrate the concept. Figure 1.3(a) represents a hypothetical offshore wind farm with multiple floating offshore wind turbines (FOWTs). The black dots indicate selected FOWTs where the Kalman filter algorithm is used to identify incoming waves. The real-time wave data obtained from the Kalman filter are then utilized to predict future waves and responses at other FOWTs (grey dots), particularly those within the inner perimeter. Implementing this approach in a wind farm can enhance monitoring and maintenance efficiency as not all FOWTs require physical sensors and instrumentation systems, potentially reducing monitoring costs and bringing the digital twin concept closer to reality.

Additionally, knowing the real-time future wave allows for precise determination of the "safe-to-jump-to-FOWT" time frame, enhancing the safety of maintenance crews. To carry out the maintenance and service of offshore windfarm, Service Operations Vessel (SOV) is deployed to the windfarm. SOVs are equipped with heave-compensated “walk-to-work” gangways as seen in Figure 1.2(a), and small (typically 10-ton) cranes to transfer equipment onto the platform's base. SOVs also serve purpose as on-site accommodations for workers with typical capacity around 40 people. The majority of SOVs are designed and equipped with smaller vessels or typically referred as daughter vessels. The primary function of these vessels is to transport small crews to offshore wind turbine installations for day trips focused on operations, maintenance visits, and inspections hence also referred as Crew Transfer Vessel (CTV). Since CTVs are much smaller than SOVs, it is not equipped with “walk-to”work” gangways as seen in Figure 1.2(b). Consequently, precise determination of the "safe-to-jump-to-FOWT" time frame becomes crucial in this case. One of the most common method to reach the decision for maintenance crew members to safely access or disembark from offshore wind turbines typically is via direct observation by experienced crew members and vessel operators. They rely on their knowledge and skills to interpret visual cues such as wave height, wave patterns, and surface conditions. Though visual observations are often used in combination with other methods (such as weather forecast) to gain a qualitative understanding of the sea state, human errors cannot be surely eliminated. Hence, knowing the real-time wave profile—especially the future wave of a few minutes ahead, is truly beneficial to ensure higher level of safety.

Last but not least, by knowing the future wave height, it becomes possible to estimate the future relative wind velocity, which is valuable for optimizing blade pitch control and improving energy generation efficiency. Blade pitch control is a critical mechanism in offshore wind

turbines that helps optimize their performance and ensures safe operation in varying wind conditions. The primary function of blade pitch control is to adjust the angle or pitch of the turbine blades to regulate the amount of power captured from the wind. By controlling the blade pitch angle, the wind turbine can optimize its power output, maximize energy capture from the wind, and maintain a safe operating range. Blade pitch control is especially crucial in high wind conditions to prevent over-speeding and potential damage to the turbine. Based on this, it becomes apparent that the knowledge of future wind velocity at tower top relative the substructure motion in wave is helpful so that the blade pitch control mechanism can operate accordingly.

(a)

(b)

Figure 1. 2 (a) Service Operation Vessel (SOV) (b) Crew Transfer Vessel (CTV)

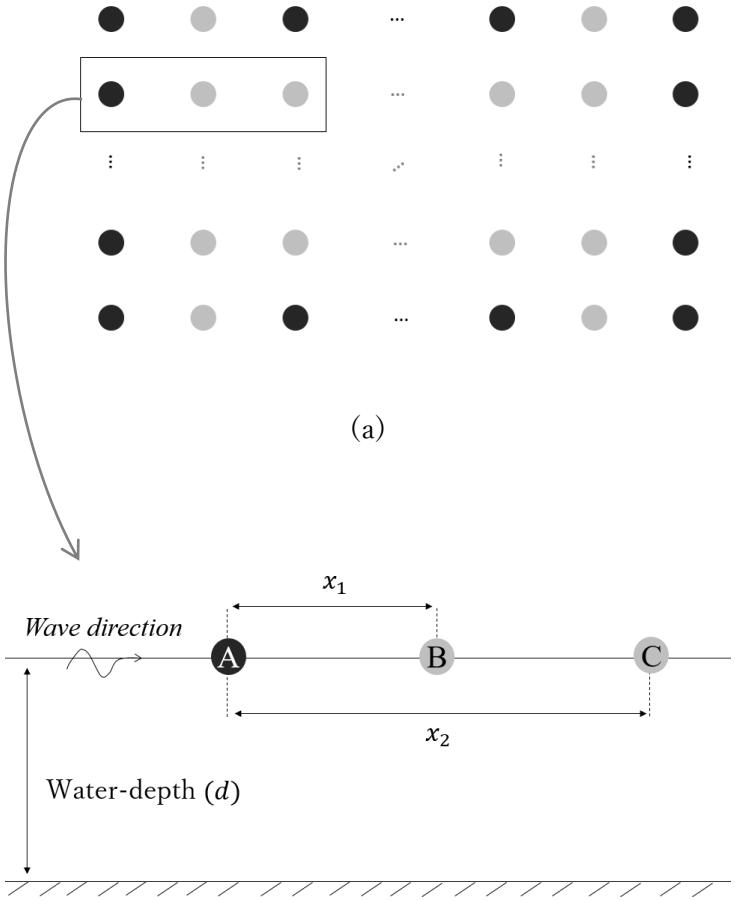

Figure 1. 3 Visualizations of the concept (a) A hypothetical offshore wind farm (b) Point locations assumed for the 2D tank test

Before investigating the application of Kalman filter for future predictions, the employability of the Kalman filter for wave prediction with FOWT as subject structure is first evaluated. Compared to ships, modeling the structure of a FOWT is more complex due to its unique shape and size. Therefore, the first part of the study is set to investigate the feasibility and effectiveness of implementing the Kalman filter for wave prediction in the context of FOWTs. Here, two different semisubmersible types of FOWT are taken into accounts, where the main difference lies on the corresponding TFs in which one of the designs generally has less pronounced resonance peak compared to the other (see Chapter 3).

As mentioned, response data from the FOWT are crucial for the Kalman filter algorithm. Two types of measurement data are used: numerically generated data and experimental data. However, the experiment data provided are only for one of the designs, with further limitation.

The numerical data are generated using the NK-UTWind program, which simulates FOWT structural responses in the time domain, taking into account hydrodynamic and aerodynamic loads. Two load models are considered: one considering only hydrodynamic loads and another considering both aerodynamic and hydrodynamic loads. These models are used to assess the algorithm's performance under different levels of complexity and uncertainty. The presence of aerodynamic damping introduces nonlinearity in the FOWT's structural response due to the interaction between waves and wind. For experimental data, measurements are obtained from a 1/50 scaled model tested in a towing tank.

Next, based on the concept illustrated in Figure 1.3(a), a 2D tank test was developed to simulate a partial aspect of the idea of digital twin implementation for wind farm. Introducing multiple bodies with spatial distance is necessary since it is found that carrying out future wave prediction without taking into account a spatial distance will produce a very short future predictable time (1-2 cycles ahead only). In this experiment, three simplified floating models were used (see Chapter 5), focusing on the black box area in Figure 1.3(a) and further explained in Figure 1.3(b). Point A represents the reference point where the Kalman filter algorithm is implemented, and future wave predictions are made for points B and C, located at distances x_1 and x_2 away from A. By knowing the wave at point A (or to be more specific, the elementary wave coefficients), the future wave and responses at points B and C can be calculated based on the wave at point A. This approach can be viewed as a variation of the convolution integral, which determines wave history at one point based on the wave at another point using an impulse response function (Davis & Zarnick, 1966). However, it is important to address the issue of causality, as the impulse response function does not inherently satisfy causality. Causality implies that a signal can be physically realized in real time, which is crucial for time-dependent water wave prediction. A subsequent study by Iida & Minoura (Iida & Minoura, 2022) discovered that introducing the assumption of finite-depth water can eliminate the non-causality. In this part of the study, the limitation of causality based on these findings is taken into consideration.

1.2 Objectives

The objectives of this dissertation are described as follows:

- To investigate the possibility of employing a linear filter, i.e. the Kalman filter to predict the wave surrounding FOWT using responses as input.
- To investigate the effect of the nonlinearity from the coupling of wave and wind loads on the filter ability to predict the correct wave input.
- To find the common grounds on what exactly influence the filter ability to give a high accuracy prediction results by taking into accounts two different design of semisubmersible type of FOWTs with different response characteristics.

- To investigate the possibility of extending the Kalman filter algorithm to estimate the future waves and responses on the multiple floating systems after spatial distance is introduced.

1.3 Organization of the thesis

In Chapter 1, the background, motivation, and problem statements of the study are elaborated.

In Chapter 2, the theory of the Kalman filter algorithm and its modelling for the wave prediction adopted in this study is given. The chapter begins with an explanation of the filter origin and its general formulation. The explanation followed by previous studies on the wave prediction based on the Kalman filter algorithm, be it a prediction carried out using a more similar modelling or a completely different modelling. The last section of this chapter explains the modelling approach of the Kalman filter algorithm adopted in this study. Shortly, the wave is assumed to be linear, hence, the wave is decomposable into many elementary waves based within the range of the spectrum. The Kalman filter is prescribed to predict the Fourier coefficients of the elementary waves. Structural response is incorporated as the inputs and TFs are used to relate the input and output of the filter.

In Chapter 3, wave predictions based on the aforementioned Kalman filter algorithm is undertaken. In this chapter, FOWT is adopted as the subject structure. Since this study projects that the wave predictions should be incorporated as part of the digital twin of a wind farm, it is important to firstly investigate the employability of the Kalman filter itself for wave predictions surrounding FOWT. In this case, the semisubmersible type of FOWT is adopted. Further, two different designs of the semisubmersible FOWT are taken into account. These designs are referred as Semisub-A and Semisub-B. The main difference between the two designs lay on the corresponding TFs, with Semisub-B having less pronounced peak in the amplitude domain compared to Semisub-A.

First, a fully linear approach between the wave and response using Semisub-A design are taken into account to investigate the frequency discretization influences to the filtering results accuracy and time. Next, reference and input data containing different level of nonlinearity from NK-UTWind simulations are used. Predictions on both design are carried out to understand the effects of the TFs to the filtering results. The presence of aerodynamic loads that effect the trend of the amplitude domain TFs is incorporated as well. Lastly, an experimental based data limited to Semisub-A design is taken into account to predict the wave around the structure, where the wave reference data are also from the same experiment.

In Chapter 4, causality limitation that dictates the experiment set-up is given. The way of the

Kalman filter algorithm being extended to obtain future predictions is also discussed in this chapter. In the beginning, the non-causality phenomenon arisen in the water waves prediction is explained. This is done via discussing a water wave prediction based on the convolution integral. Shortly, when wave prediction using convolution integral is first introduced, it is found that non-causality appears in the impulse response function of the integral. Later on, it was found that the non-causality will be negligible given a long enough distance of the two points involved in the wave predictions, that is, when the two points distance divided by the water depth should be at least equal to 3. Hence, causality limitation was born. Since the convolution integral is very much comparable to the Fourier series prediction, this limitation can be used to ensure causality in the Kalman filter based prediction. Next, the basis of the algorithm extension to obtain the future predictions is discussed. This extension is prescribed centering around the spatial distance of multiple floating bodies.

In Chapter 5, the future prediction results based on the experiment in a 2D flume tank are presented. The chapter begins with the description on the subject structure and tank set-up. The tank set-up is dictated by the causality limitation discussed in the Chapter 4. The explanation on the measurement system involved in the experiment is also provided in this chapter. The experiment accounts for the rigid body response given regular and irregular (JONSWAP spectrum) wave cases. The TFs retrieved from the experiment is compared with numerical TFs from an in-house code developed based on the boundary element method. After the TFs are confirmed, the wave prediction on point A (see Figure 1.3) is undertaken. The results from the Kalman filter algorithm is compared with the wave time series from experiment. Next, the future wave predictions at point B and C are carried out. Similarly, the future wave predictions based on the Kalman filter results are compared to the experiment wave data. Lastly, since the future wave at point B and C are known, the future response at the two points then can be estimated as well. The accuracy is found by comparing the results based on the Kalman filter predictions with the response time series obtained in the experiment.

In Chapter 6, the conclusion of the current study is discussed, as well as the suggestions for future work.

Chapter 2
Theoretical background

2.1 Random process and general Kalman filter algorithm

Kalman filter was first introduced by R. E. Kalman in the 1960 as an algorithm that is meant to solve linear filtering problem recursively, particularly for cases concerning random process (Kalman, 1960). In the aforementioned published article, the Kalman filter is especially prescribed to help eliminating problems encountered when Wiener filter is used to resolve the prediction, separation, or detection of a random signal. Wiener filter itself is a statistical-based approach linear predictor introduced by Norbert Wiener, with its resourcefulness includes the ability to estimate a random process using an observed process with noise that is correlated to the targeted random process itself (Dogariu, Benesty, Paleolugu, & Ciochină, 2021). However, in his article (Kalman, 1960), Kalman notes that when a prediction of random signals and/or separation of random signals from random noise are done using Wiener's formulation (Wiener, 1949), a Wiener-Hopf integral equation is bound to come across. Though different approaches (Zadeh & Ragazzini, 1950; Darlington, 1958; Lanning & Battin, 1956) have been introduced to find the Wiener filter's specification that is able to perform the prediction, separation, or detection of a random signals effectively, Kalman argues that formulating a method which solves the Wiener problem given the practical limitations is needed. Hence, the Kalman filter algorithm is externalized.

Like in most linear filtering methods, the notions of *state* and *state transition* are emphasized in the Kalman filter algorithm. This simply means that the linear systems will be described via its first order differential equations systems. When a random function is assumed to be the output of a dynamic system excited by an independent Gaussian random process, the concept of *state* then can be introduced. Intuitively, this refers to the known quantitative information needed from the past behavior of a system to predict its future tendency. To enumerate the transformation of one state into another state as time passes, a *state transitions* is then required to be introduced.

$$\frac{d\mathbf{x}}{dt} = \mathbf{F}(t)\mathbf{x} + \mathbf{D}(t)\mathbf{u}(t) \quad (2.1)$$

$$\mathbf{y}(t) = \mathbf{M}(t)\mathbf{x}(t) \quad (2.2)$$

$$\mathbf{x}(t+1) = \mathbf{A}(t+1;\, t)\mathbf{x}(t) + \mathbf{u}(t) \quad \cdots\cdots (2.3)$$

Mathematically, a linear dynamic system can be described via its general vector differential equation. This is further shown in Equation (2.1) and (2.2), where **x** represents the state vector of the system (its components are known as the state variables), **u** is the system's input vector, **y** is the system's output vector, and **F**, **D**, **M** are the matrix functions—with **M** is specifically referred as the observation matrix in the Kalman filter algorithm. Figure 2.1 is presented to visually explain the interpretation of Equation (2.1) and (2.2) via its matrix block diagram. Next, if the system is assumed to be stationary and the input **u** is constant for every sampling period and described as a vector-valued, independent, zero-mean Gaussian random process, Equation (2.1) then can be discretized and transformed to Equation (2.3), where **A** defines the state transition matrix.

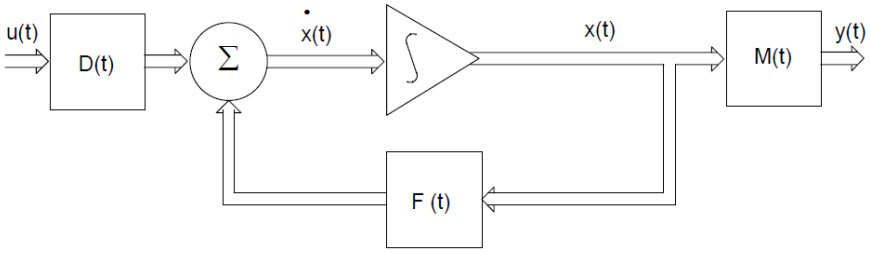

Figure 2. 1 Matrix block diagram of the general linear continuous-dynamic system *(Kalman, 1960)*

After the state-space model (Equation 3) and measurement model (Equation 2) of the dynamic system are prescribed, the filtering the can be carried out. However, for the sake of understanding the study presented in this report, several adjustments that are deemed to be suitable are undertaken. Firstly, the variable t is now altered to n to avoid confusion between the time variable and the number of sampling (due to the discretization of the process). Other than that, **v** and **w** are now introduced as process and measurement noise vector, respectively. These noises are assumed to be independent Gaussian process with zero-mean. Lastly, a dynamic modelling that validates the termination of system's input as a separate entity **u** is also considered. Hence, Equation (2.2) and (2.3) are now respectively Equation (2.5) and (2.4).

$$\mathbf{x}(n+1) = \mathbf{A}\mathbf{x}(n) + \mathbf{v}(n) \quad \cdots\cdots (2.4)$$

$$\mathbf{y}(n) = \mathbf{M}\mathbf{x}(n) + \mathbf{w}(n) \quad \cdots\cdots (2.5)$$

Since the targeted state to be predicted is essentially a random process rooted in the probability theory, it is only natural that the Kalman filter works based on the propagation of the mean (**x**) and covariance (**P**) of the state through time (Simon, 2006). The filtering itself is composed out of two steps, i.e. *prediction* and *correction* step. Its full algorithm is given in the Equation (2.6) until (2.10). Here, the mean and covariance of the state are what the filter tries to estimate in the prediction step (results from this step are indicated with tilde, ~). This part of the algorithm is shown in the Equation (2.6) and (2.7). After the state properties are calculated in the prediction step, its results then will be used as the input in the correction step (results from this step are indicated with caret, ^). The process of the correction step is defined by Equation (2.8) until (2.10). Here, the prediction results are essentially updated and compared with the data from observation (or measurement). Other than that, the prediction results are also weighted with the Kalman gain (**K**), hence producing the more accurate filtering results. In these equations, **Q**, **R** and **I** are respectively the system noise covariance, the observation noise covariance, and an identity matrix. A further reading may be necessary to understand the derivation and theory behind the Kalman filter algorithm. However, a simplified chart to provide an understanding on how the algorithm works is given in Figure 2.2.

$$\tilde{\mathbf{x}}(n+1) = \mathbf{A}\hat{\mathbf{x}}(n) \quad \cdots\cdots (2.6)$$

$$\tilde{\mathbf{P}}(n+1) = \mathbf{A}\hat{\mathbf{P}}(n)\mathbf{A}^T + \mathbf{Q} \quad \cdots\cdots (2.7)$$

$$\mathbf{K} = \tilde{\mathbf{P}}(n+1)\mathbf{M}(n+1)^T\left(\mathbf{M}(n+1)\tilde{\mathbf{P}}(n+1)\mathbf{M}(n+1)^T + \mathbf{R}\right)^T \quad \cdots\cdots (2.8)$$

$$\hat{\mathbf{x}}(n+1) = \tilde{\mathbf{x}}(n+1) + \mathbf{K}\left(\mathbf{y}(n+1) - \mathbf{M}\tilde{\mathbf{x}}(n+1)\right) \quad \cdots\cdots (2.9)$$

$$\hat{\mathbf{P}}(n+1) = \left(\mathbf{I} - \mathbf{K}\,\mathbf{M}(n+1)\right)\tilde{\mathbf{P}}(n+1) \quad \cdots\cdots (2.10)$$

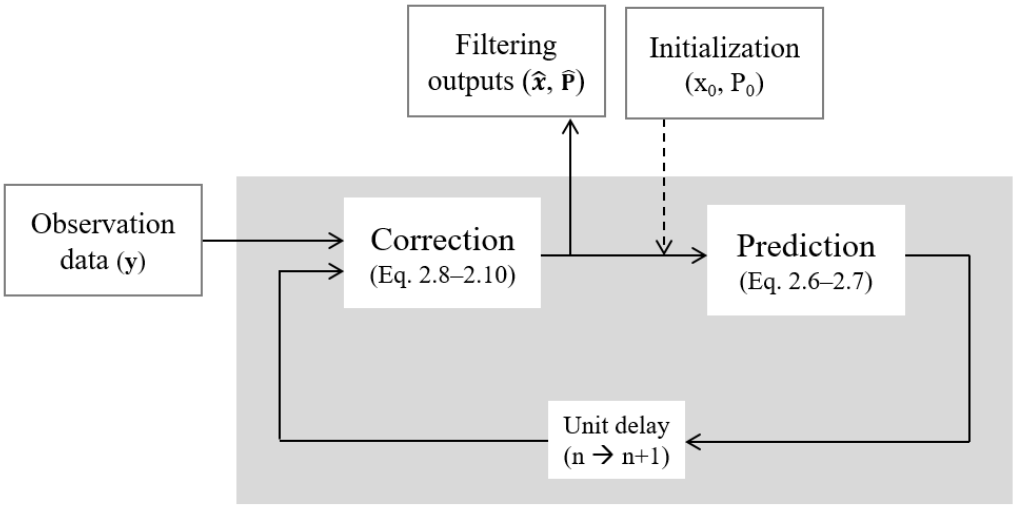

Figure 2. 2 Simplified chart of the Kalman filtering process

2.2 Previous studies on Kalman filter-based wave prediction

Since its algorithm is first introduced, Kalman filter has been a subject of interest—especially from the industrial electronics community and it also has been introduced and utilized in engineering fields since the 1970s for various industry applications (Auger, et al., 2013). Meanwhile, though the industry application of Kalman filter-based wave prediction is still very limited—if not non-existent, there has been a considerable amount of studies dedicated to explore the possibility on using this algorithm for wave prediction. In this section, several selected studies are summarized to give further context on the proposed utilization of the Kalman filter in this study and its characteristics compared to the precedent research.

Emmanouil, et al. conducted a study on the possibility to exploit Kalman filter as a complementary algorithm to enhance wave analysis and forecasting results when numerical atmospheric and ocean wave models are employed (Emmanouil, Galanis, & Kallos, 2012). To be more specific, the Kalman filter algorithm is used as post processes to minimize the systematic deviations of the wave model outputs. The North Atlantic Ocean is targeted in this study and the significant wave heights at different coordinate are prescribed as the state variables. Results show that this research is reasonably successful—though naturally with several limitations. Similarly, Pinto, et al. also investigate a Kalman filter algorithm to be assimilated to an ocean wave model (Pinto, Bernardino, & Pires Silva, 2005). The objective of this study is more or less the same as Emmanouil, et al. (Emmanouil, Galanis, & Kallos, 2012), i.e. to assist the wave model in finding the more accurate statistical sea-state forecast. The main different lies in the state-space modelling for the Kalman filter algorithm, with Pinto, et al. (Pinto, Bernardino, & Pires Silva, 2005) concentrate on specifying the wave energy over a smaller area as the state variables.

While the study of Kalman filter-based prediction for statistical wave is undoubtedly an important field of study, a real-time wave prediction outputs will be more beneficial given the problem statement of this study. Hanaki, et al. (Hanaki, Takaoka, & Minoura, 2022) have investigated the application of Ensemble Kalman filter (EnKF)—a variation of the Kalman filter algorithm for nonlinear prediction, to estimate added mass, damping coefficients, and wave-exciting force targeted for seakeeping purposes. Their method assumes that the wave-exciting forces are the input of the dynamic system modelling and EnKF is used to predict the parameters entitled to this force, among other state variables embedded to the filter. Though the prediction is targeted for a real-time result, the wave elevation history—that becomes the main prediction output in this present study, is needed to be known and/or measured beforehand for the EnKF to perform predictions.

Another study intended to investigate the Kalman filter algorithm for wave prediction is done by Pascoal & Soares (Pascoal & Soares, 2009). Here, the wave prediction is carried out by estimating the wave coefficients for every elementary waves that build the irregular waves as a whole based on the linear wave theory assumption. In their formulation, a vessel motions are used as the observation data for the Kalman filter algorithm. Later on, their work is validated by Pascoal, et al. (Pascoal, Perera, & Soares, 2017) based on the onboard sea-trial data of the Portuguese Navy Oceanographic vessel "NRP Almirante Gago Coutinho". The algorithm formulation of the present study is similar with the aforementioned studies, with the main difference lies in the fact that directional sea spectrum is selected as the main subject discussion in there, not the real-time wave elevation history.

2.3 Kalman filter modeling for real-time wave prediction

While the general explanation of the Kalman filter algorithm and its working mechanism are explained in 2.1, a particular modelling for the algorithm to make sense exclusive for a real-time wave prediction assumed in this study is not incorporated in the aforementioned chapter. Hence, a further explanation is included here. Firstly, it is necessary to note that the prediction here works based on the inverse problem, meaning that the wave is assumed to be an unknown input and it can be estimated if the system's outputs—manifested in the form of structural responses, are known.

To begin with, the ocean surface that follows the linear waves propagation is described. Based on this assumption, a function of angular wave frequency (ω) and heading direction (β) can be used to describe the irregular plane waves. Then, the wave elevation history evolving at every j-th position of $\mathbf{p_j} = (x_j, y_j)$ with its respective wave vector k at any time t can be expressed as Equation (2.11). Here, $A(\omega, \beta)$ is the complex amplitude of the elementary waves and i denotes the imaginary unit. When the irregular wave observed at a point of origin is assumed to be built based on the weighted sum of the elementary waves, Equation (2.11) then can be discretized. Consequently, the complex amplitudes are needed to be decomposed into wave coefficients a and b. Equation (2.12) shows the discretized version of Equation (2.11), with n_β and n_ω respectively denote the number of heading direction and elementary wave. The two wave coefficients of every elementary wave for every heading angle ($a_{p,q}$ and $b_{p,q}$) are then prescribed as the state variables in the Kalman filter algorithm (i.e. components of the state vector $\mathbf{x}$) in this study.

$$\eta(\mathbf{p_j}, t) = \mathrm{Re} \iint A(\omega, \beta)\, e^{i(\omega t - k.\mathbf{p_j})}\, d\omega\, d\beta \quad \cdots\cdots (2.11)$$

$$\eta(t) = \sum_{q=1}^{n_\beta} \sum_{p=1}^{n_\omega} a_{p,q}\, \cos(\omega_p t) + \sum_{q=1}^{n_\beta} \sum_{p=1}^{n_\omega} b_{p,q}\, \sin(\omega_p t) \quad \cdots\cdots (2.12)$$

$$Y(t) = \mathrm{Re} \iint H(\omega, \beta) A(\omega, \beta)\, e^{i(\omega t - k.\mathbf{p_j})}\, d\omega d\beta \quad \cdots\cdots (2.13)$$

$$Y(t) = \sum_{p=1}^{n_\beta} \sum_{q=1}^{n_\omega} a_{p,q}\, G(\omega_p, \beta_q) \cos \gamma_{pq} + \sum_{q=1}^{n_\beta} \sum_{p=1}^{n_\omega} b_{p,q}\, G(\omega_p, \beta_q) \sin \gamma_{pq} \quad \cdots\cdots (2.14)$$

where $\gamma_{pq} = \left(\omega_p t + \varphi(\omega_p, \beta_q)\right)$

Another important part of the Kalman filter algorithm is the observation matrix (**M**), as it directly links the state variables and observation data as illustrated in Equation (2.5). To prescribe the observation matrix, a response model is first needed to be described. In this study, the responses measured from the FOWT are assumed to be linear to the waves. The properties of these responses are expressed in the form of a transfer function exclusive for every measured location and observation type itself—e.g. strain, displacement, acceleration, etc. Mathematically, this can be written as Equation (2.13). Here, the transfer function is denoted as $H(\omega, \beta)$ and it is a function of angular frequency and heading direction. Oftentimes, a transfer function used to describe an offshore structure's responses are further expressed as a pair of response amplitude operator (RAO) function and phase function that explains the phase angle difference between the input wave and the response itself. This will be the case in this study as well. Taking into accounts the aforementioned assumption, the discretized version of Equation (2.13) then is written as Equation (2.14), with the RAO and phase function are denoted as G and φ, respectively. Equation (2.14) will later be utilized as the foundation to determine the observation matrix components.

To summarize, the Kalman filter algorithm in this study is formulated in a way where the elementary wave coefficients are the state vector components (Equation 2.15) with its dimension to be $2 \times N$ by one—with N represents $n_\omega \times n_\beta$, and the observation matrix (Equation 2.16) components are derived based on the RAO and phase functions that associate the input wave with the structure's response (the size of this matrix is m by $2 \times N$, with m indicates the number of instrument used to retrieve the response data). The time history of the responses is assumed to be measurable using sensors installed on the structure from m number of sensor are prescribed as the components of the observation vector (**y**) in the Kalman filter. Lastly, as the predicted state variables are assumed to be Gaussian, the drift model then can be utilized. Consequently, the state-transition matrix (**A**) then can be defined as an identity matrix, with its size to be $2 \times N$ by $2 \times N$.

$$\mathbf{x}(n) = \left[a_1(n)\; b_1(n)\; a_2(n)\; b_2(n) \ldots a_{n_\omega, n_\beta}(n)\; b_{n_\omega, n_\beta}(n)\right]^T \quad \cdots\cdots (2.15)$$

$$\mathbf{M} = \begin{bmatrix} G_1(\omega_1, \beta_1) \cos \gamma_{pq} & \cdots & G_m(\omega_1, \beta_1) \cos \gamma_{pq} \\ G_1(\omega_1, \beta_1) \sin \gamma_{pq} & \cdots & G_m(\omega_1, \beta_1) \sin \gamma_{pq} \\ \vdots & \ddots & \vdots \\ G_1\left(\omega_{n_\omega}, \beta_{n_\beta}\right) \cos \gamma_{pq} & \cdots & G_m\left(\omega_{n_\omega}, \beta_{n_\beta}\right) \cos \gamma_{pq} \\ G_1\left(\omega_{n_\omega}, \beta_{n_\beta}\right) \sin \gamma_{pq} & \cdots & G_m\left(\omega_{n_\omega}, \beta_{n_\beta}\right) \sin \gamma_{pq} \end{bmatrix}^T \quad \cdots\cdots (2.16)$$

where $\gamma_{pq} = \left(\omega_p t + \varphi(\omega_p, \beta_q)\right)$

2.4 NK-UTWind

The filtering to predict the waves surrounding FOWT accounts for experiment and simulation data based. For the simulation-based results discussion, a tool to generate the time domain input and reference data for the filtering is unavoidably needed. For this purpose, an aero-hydro-structural code referred as NK-UTWind is utilized. The code is developed by Suzuki, et al (Suzuki, et al., 2013), and in the coming years, their works are further improved by Oh, et al (Oh, Ishii, Iijima, & Suzuki, 2019) and Takata, et al (Takata, et al., 2021). The code has been deemed suitable as NK-UTWind is coupled with FAST, another code—developed by NREL (Jonkman & Buhl Jr., 2005), that can calculate the aerodynamic loads in the wind turbine. Hence, simulating a structural analysis of offshore wind turbine that has combined loads from wind and wave may be done using NK-UTWind.

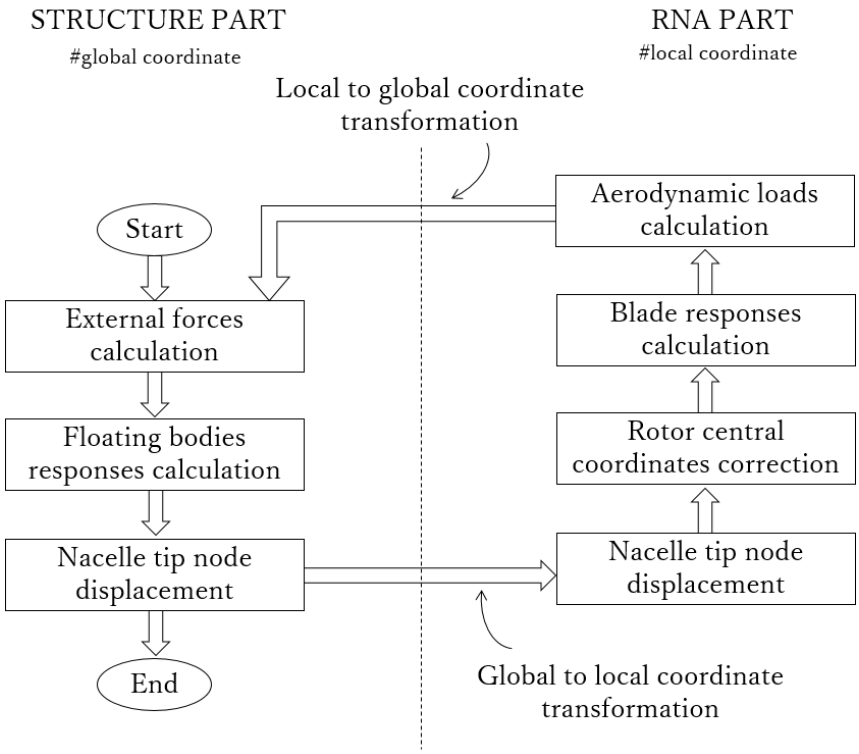

Figure 2. 3 Flowchart of coupled simulation using NK-UTWind

In the code, the whole structure is divided into two parts, they are the rotor-nacelle-assembly (RNA) and another part referred as the structure part. For further context, the structure consists out of tower, substructure, and mooring. For further reference, Figure 2.3 that shows the general process when coupled simulation is given. To get the time domain results, the structure part is subdivided into node elements and beam elements, using a finite element approach. Each node possesses three translational and three angular degrees of freedom. As a

result, the structure part consists of $6L$ degrees of freedom, where L represents the number of structural nodes.

The equation of motions to be solved by NK-UTWind is shown in the Equation (2.17). In the equation provided, $[\boldsymbol{M}]$ represents the mass matrix, which has a dimension of $6L$ for a structural model with L nodes. $[\boldsymbol{C}]$ represents the damping matrix, and $[\boldsymbol{K}]$ represents the structural stiffness matrix. The variables $\boldsymbol{x}$, $\dot{\boldsymbol{x}}$, and $\ddot{\boldsymbol{x}}$ correspond to the nodal displacement vector, velocity vector, and acceleration vector, respectively. On the right-hand side of the equation, there is a vector consisting of four force components: hydrodynamic force, forces from mooring lines, restoring force, and aerodynamic force. The simulation is performed in sequential time steps. Initially, FAST calculates the thrust force generated by the rotor and provides these results to NK-UTWind as boundary conditions. Next, NK-UTWind evaluates the structural response based on these conditions. The displacement and velocity at the top of the tower, obtained from NK-UTWind, are then returned to FAST as boundary conditions. This iterative process is repeated for each prescribed time step. The time-dependent behavior of the entire system is assessed through a loosely coupled analysis.

$$[\boldsymbol{M}]\{\ddot{\boldsymbol{x}}\} + [\boldsymbol{C}]\{\dot{\boldsymbol{x}}\} + [\boldsymbol{K}]\{\boldsymbol{x}\} = \left\{\boldsymbol{F}^{\boldsymbol{hydro}} + \boldsymbol{F}^{\boldsymbol{lines}} + \boldsymbol{F}^{\boldsymbol{buoyancy}} + \boldsymbol{F}^{\boldsymbol{aero}}\right\} \quad (2.17)$$

The hydrodynamic load in NK-UTWind is evaluated based on the Morison's formula (Morison, O'Brien, Johnson, & Schaaf, 1950). Morison's equation can be applied to elongated members where the diameter of the cylindrical element is smaller than the wavelength and the wave amplitude is not negligible compared to the diameter of the elliptical cylinder. Since the structure under the water surface can be assumed to be an elongated cylinder type column, it was judged that the application is possible. This equation is semi-empirical equation used to estimate the hydrodynamic forces acting on an object in the direction of incoming waves. It incorporates three components, i.e. the Froude-Krylov force, which is generated by the pressure field of the undisturbed waves; the added mass, which accounts for the inertia of the surrounding fluid that needs to be accelerated; and the viscous drag. Mathematically, this can be written as Equation (2.18). In the given context, ρ represents the density of the fluid, D refers to the diameter of the column element, and v represents the velocity of fluid particles. Additionally, C_m represents the coefficient for added mass, and C_d represents the coefficient for drag force. This equation requires determining the added mass coefficient and drag coefficient through empirical relations. However, the Morison equation can be easily applied and enables the calculation of wave forces in the time domain, which contributes to its widespread use in the field of hydrodynamics.

$$F^{hydro} = \rho\frac{\pi D^2}{4}\dot{v} + C_m\rho\frac{\pi D^2}{4}(\dot{v} - \ddot{x}) + C_d\frac{1}{2}\rho D(v - \dot{x})|v - \dot{x}| \quad (2.18)$$

Meanwhile, the mooring force can be determined using methods such as quasi-static catenary calculation, lumped-mass method, or linear spring method. In this study, for the sake of simplification, linear spring approach is adopted for the simulation. Using the linear spring method, the interaction between the floating body and the mooring system can be approximately analyzed by considering the mooring system as a linear spring. In this method, the tension of the linear spring is described as Equation (2.19), where $\mathrm{T_0}, \mathrm{K_m}$ and $\mathrm{L_0}$ are respectively the initial tension of the mooring rope, spring constant, and initial mooring length. Furthermore, (x_0, y_0, z_0) are the coordinates of the bottom end of the mooring rope and (x_2, y_2, z_2) are the coordinates of the top end of the mooring rope. The total length $\mathrm{L_m}$ of the mooring rope is expressed by Equation (2.20) and each directional component of the length of the mooring rope is expressed by Equation (2.21). At last, the force components at the top of the mooring then may be described as Equation (2.22).

$$\mathrm{T_m} = \mathrm{T_0} + \mathrm{K_m}(\mathrm{L} - \mathrm{L_0}) \quad \cdots\cdots (2.19)$$

$$\mathrm{L_m} = \sqrt{\mathrm{L_x^2} + \mathrm{L_y^2} + \mathrm{L_z^2}} \quad \cdots\cdots (2.20)$$

$$\begin{pmatrix} \mathrm{L_x} \\ \mathrm{L_y} \\ \mathrm{L_z} \end{pmatrix} = \begin{pmatrix} x_2 - x_0 \\ y_2 - y_0 \\ z_2 - z_0 \end{pmatrix} \quad \cdots\cdots (2.21)$$

$$\boldsymbol{F}^T = -\frac{\mathrm{T_m}}{\mathrm{L_m}} \begin{pmatrix} \mathrm{L_x} \\ \mathrm{L_y} \\ \mathrm{L_z} \end{pmatrix} \quad \cdots\cdots (2.22)$$

Meanwhile, the aerodynamic loads in the simulation is calculated based on the Blade Element Momentum theory (BEM theory), a theoretical approach used to analyze the aerodynamics of rotating blades, commonly employed in the study of wind turbines and propellers. Principally, the BEM theory is a combination out of two different theories, i.e. blade element theory and momentum theory (Leishman, 2000). BEM theory calculates the aerodynamic forces on a rotating blade by breaking down the blade into small sections, called blade elements, and analysing the forces and velocities acting on each element. Figure 2.4 provides an illustration of an airfoil with the velocities and angles that determine the forces acting on the element, as well as the induced velocities resulting from the wake influence. In this figure, V_∞, a, Ω, r and a' are respectively mean wind speed, axial induction factor, rotor rotational speed, local radius, and rotational induction factor. Moreover, ϕ_a, α_a, and β_a are inflow angle, angle of attack, and pitch angle, respectively. Figure 2.5 depicts the resulting aerodynamic forces on the element and their components, which are perpendicular and parallel to the rotor plane. These forces, namely thrust and torque, are crucial in turbine design. In Figure 2.5, the local inflow angle (ϕ_a) establishes the relationship between the lift and drag of the airfoil element and the thrust and torque forces. As shown in Figure 2.4, the inflow angle is the sum of the local pitch

angle of the blade (β_a) and the angle of attack (α_a). The local pitch angle depends on factors such as the blade's static geometry, elastic deflections, and the active or passive blade pitch control system. The angle of attack is determined by the local velocity vector, which is in turn influenced by factors like the incoming local wind speed, rotor speed, blade element velocities, and induced velocities (Moriarty & Hansen, 2005).

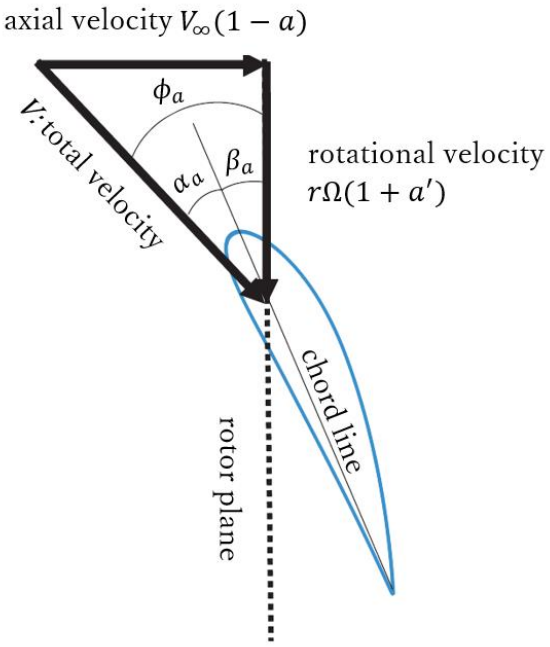

Figure 2. 4 Local element flow angles and velocities

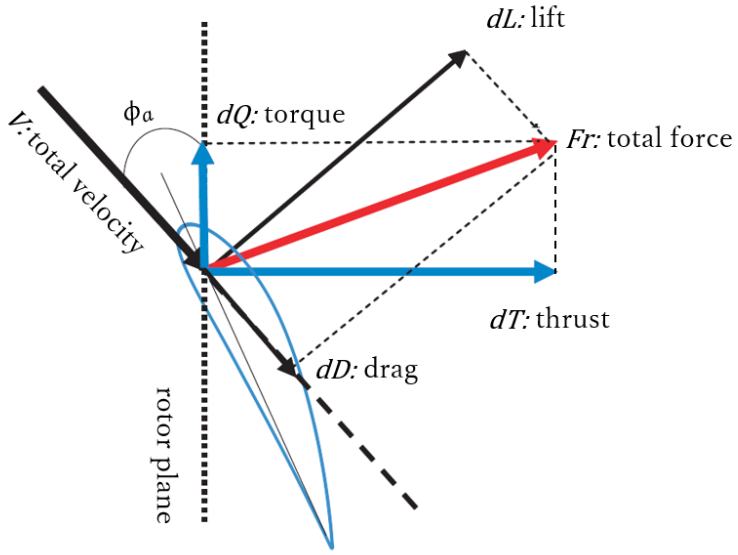

Figure 2. 5 Local elemental forces in an airfoil section

Principally, the thrust and torque of an airfoil section may be described based on the mathematical relationship between lift force, drag force, and inflow angle of the blade element (See Figure 2.5). Extensive derivation shows that respectively, thrust and torque around an annulus of width dr can be further expressed as Equation (2.23) and (2.24), where B, ρ_a, C_L, C_D, and c_r are respectively the number of blades, air density, lift coefficient, drag coefficient, and chord length. The aforementioned two equations however, are formulated without taking into accounts the wake effects that majorly influences the rotor induced velocity distribution. The impact on induced velocity within the rotor plane is most noticeable in the vicinity of the blade tips, which coincidentally holds the highest influence over the power output of the turbine. To compensate, a theory developed by Prandtl (Glauert, 1935) is incorporated. The principle of Prandtl's theory is that the velocity in the plane of the rotor is changed by the disturbed flow near the tip, which is calculated after momentum theory is taken into accounts. For this purpose, Prandtl expanded the equations by adopting a correction factor to the induced velocity field referred as F_a. This is expressed in the Equation (2.25). Considering this correction factor, the local thrust and torque of an airfoil section then can be finally obtained using Equation (2.26) and (2.27), respectively. The total thrust and torque are obtained by integrating these two equations from all the blade elements.

$$dT = B\frac{1}{2}\rho_a V^2(C_L \cos\phi_a + C_D \sin\phi_a)c_r dr \quad \cdots\cdots (2.23)$$

$$dQ = B\frac{1}{2}\rho_a V^2(C_L \sin\phi_a - C_D \cos\phi_a)c_r r dr \quad \cdots\cdots (2.24)$$

$$F_a = \frac{2}{\pi}\cos^{-1} e^{-f_a} \quad \cdots\cdots (2.25)$$

where $f_a = \frac{1}{2}B\frac{R_a - r}{r\sin\phi_a}$, and R_a is the rotor radius.

$$dT = 4\pi r\rho_a V_\infty^2(1-a)aF_a dr \quad \cdots\cdots (2.26)$$

$$dQ = 4\pi r^3\rho_a V_\infty \Omega(1-aF)a'F_a dr \quad \cdots\cdots (2.27)$$

This page is intentionally left blank

Chapter 3
Wave prediction results on FOWT

3.1 Subject structures

In this study, the focus is on a semi-submersible Floating Offshore Wind Turbine (FOWT). As mentioned previously, the semisubmersible types of FOWT design are adopted in this part of the study. Specifically, two different designs of semisubmersibles, referred to as Semisub-A (Inoue, 2021; Isnaini R. , Toichi, Iijima, & Tatsumi, 2022; Isnaini R. , Toichi, Tatsumi, & Iijima, 2022) and Semisub-B (Adilah & Iijima, 2021; Inoue, Adilah, Iijima, Oh, & Suzuki, 2020; Isnaini R. , Toichi, Tatsumi, & Iijima, 2022), are considered. For further context, the visualization of Semisub-A and Semisub-B can be found in Figure 3.1 and 3.2, respectively. While both designs share a common feature of having a substructure composed of three columns, they also possess distinct characteristics that result in different response behaviors and critical load points.

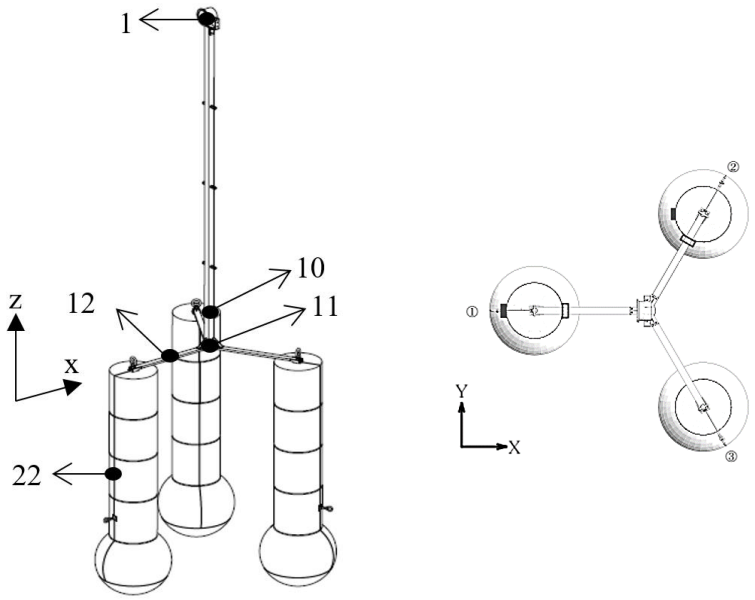

(a) (b)

Figure 3. 1 Design visualization of Semisub-A (a) Side-view, the numbers shown correspond to some of the measured locations (b) Top-view

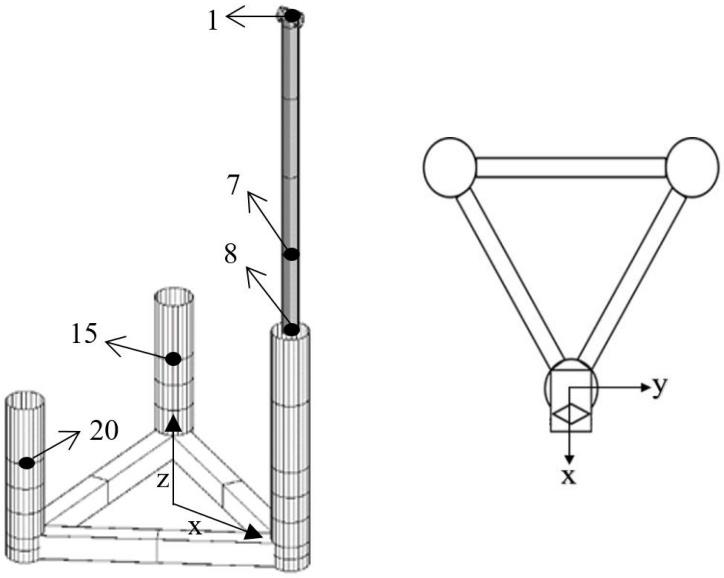

Figure 3. 2 Design visualization of Semisub-B (a) Side-view, the numbers shown correspond to some of the measured locations (b) Top-view

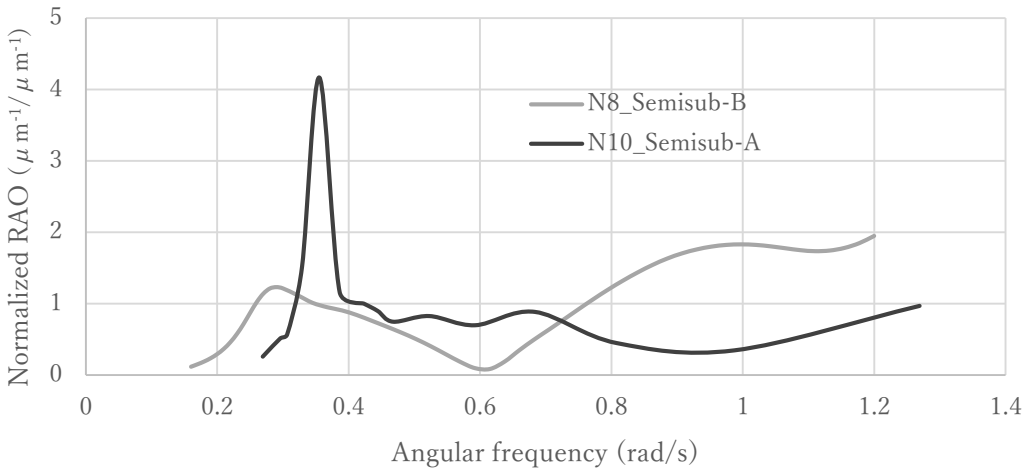

Figure 3. 3 Normalized RAO function comparison of Semisub-A (node 10) and Semisub-B (node 8)

The assigned numbers in the Figure 3.1 and 3.2 indicate the nodes and sensor locations. Further information regarding the design properties of both Semisub-A and Semisub-B can be found in Table 3.1 and 3.2, respectively. For Semisub-A, the substructure comprises three columns that provide buoyancy forces, while the superstructure, which directly interacts with

the wind, is positioned in the middle of the substructure's deck. It is evident from this design that the critical load point, which experiences the highest hydrodynamic and aerodynamic forces, is located on the deck where the tower is situated (around node 10/11). Similar to Semisub-A, Semisub-B consists of three columns along with its lower hull to provide buoyancy forces. However, there are notable differences between the two designs, with the most significant one being the placement of the superstructure. In Semisub-B, the superstructure is positioned directly on top of one of the columns (around node 8). Other than the critical load point location difference, the overall TFs, especially in the amplitude domain TFs (RAO) is found to be quite distinct between the two designs. Overall, Semisub-B has less steepness and peaky resonance compared to Semisub-A. To give more context, the strain RAO trend normalized by mean value of the corresponding function (assuming no aerodynamic load) of the two designs around their respective critical load point is shown in Figure 3.3. In this figure, black is the strain RAO (node 10) of Semisub-A, while grey is the strain RAO (node 8) of Semisub-B. Here, it can be seen that RAO belonged to Semisub-B is generally less peaky and steep compared to RAO of Semisub-A. This difference of RAO "peaky-ness" and steepness is observed to be consistent throughout different types of response between the two designs, be it the structure's elastic responses or rigid body responses.

NK-UTWind simulations (see Sec. 2.4) are conducted to calculate the transfer functions and responses for each node, which are essential components of the Kalman filter algorithm. These simulations also provide wave data that will be used as a reference for comparing with the prediction results. Additionally, this study considers two types of load conditions: wave loads only cases and combined load cases that incorporate both wave and wind forces. Further details regarding the variations in the case studies are discussed in the subsequent section.

Table 3. 1 Details on the properties of Semisub-A, real scale (except the first row)

Young's modulus of experiment model	1.93×10^{11} Pa
Young's modulus	9.65×10^{12} Pa
Displacement	1.37×10^{8} N
Draft	47.30 m
KG	15.35 m
Tower height	83.75 m
Column height	40.00 m
Total height (from keel to tower top)	140.25 m
Column diameter	10.00 m
Footing diameter	16.00 m
Deck length	20.25 m

Table 3. 2 Details on the properties of Semisub-B, real scale

Young's modulus	2.06×10^{11} Pa
Displacement	1.17×10^{8} N
Draft	25.00 m
KG	15.00 m
Tower height	113.9 m
Column height (without tower)	36.00 m
Column height (with tower)	56.00 m
Total height (from keel to tower top)	136.0 m
Column diameter	11.00 m
Lower hull length	64.18 m
Lower hull width and height	6.00 m

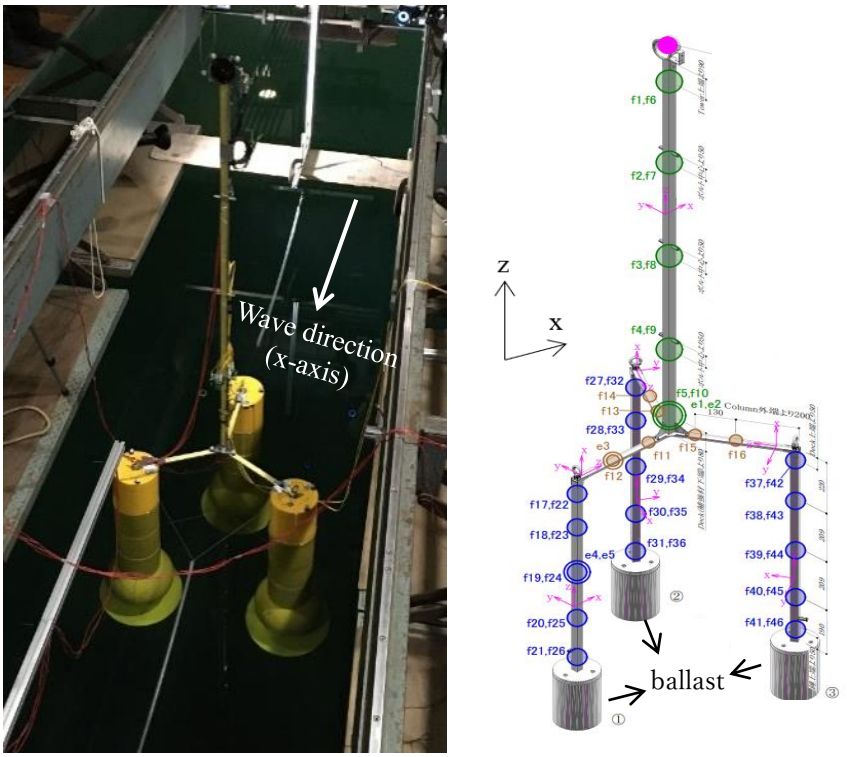

(a) (b)

Figure 3. 4 Experiment set-up (a) Semisub-A in the towing tank (b) Sensors configuration attached to the structure's "skeleton" in the experiment

The experiment was conducted at Osaka University in 2020, using a towing tank. To retrieve the experimental data, Fiber Bragg Gratings (FBG), strain gauges, and an accelerometer were employed. The experimental setup is illustrated in Figure 3.4(a), while Figure 3.4(b) displays the configuration of the sensors during the experiment. The accelerometer was placed on top of the superstructure (depicted by pink circle), while the FBG locations were indicated by green and blue circles on the superstructure and substructure, respectively. The strain gauges, represented by yellow circles, were attached to the deck part. The sensors had a sampling rate of 100 data points per second. Each FBG and strain gauge location was capable of capturing responses in both the x and y directions. It is important to note that this experiment was not specifically conducted for the present study, which implies that the available data is limited and may have an impact on the analysis of the prescribed case study. The variation in the case study are further discussed in the next section.

3.2 Case study

This section provides a more detailed explanation of the assumed case variations involved in the filtering process. In general, three types of input response and wave reference data are taken into account in this study. The first one is a fully linear assumption between wave and response. This means that while the TFs utilized to relate wave and response are computed using NK-UTWind (see the next section), the response time histories are found based on the Equation 2.13 and 2.14, while the wave time histories are calculated based on the Equation 2.11 and 2.12, indicating a fully linear relationship between the wave and response data. The goal of this part of the filtering is to find the influences of assumed discretization of the wave spectrum to the filter accuracy when it is given different complexity in the context of the TFs and the wave directionality. The TF trends are characterized by the assumed response indicated by the second column on Table 3.3. Furthermore, the existence of aerodynamic load (AD cases, where the wind is modeled as steady wind with its velocity as big as 10 m/s) is also affecting the TFs trends, hence these types of cases are also adopted to see the filter ability to estimate accurate results when different TFs are accounted for. Other than that, two types of wave directionality, i.e. unidirectional and bidirectional are taken into account to investigate the filter ability to find an accurate result when different wave complexity are taken into account.

The unidirectional wave spectrum is assumed to come towards the structure's positive x-axis direction (head sea), while the second scenario considers a bidirectional wave spectrum comprising head sea and beam sea. In the case of the unidirectional spectrum (ISSC, with a significant wave height *(Hs)* of 4.0 m and a peak period *(Tp)* of 12 s), pitch motions are utilized as the observed data. In the scenario involving a bidirectional wave spectrum, strain data are

included as part of the observed data, alongside pitch and heave, due to the increased complexity of the filtering process in this case. Strain data is known for its ability to detect responses at higher frequencies. The investigation also explores the combination of observation data locations and their impact on filter accuracy. In total, there are 11 case studies examined, as outlined in Table 3.3. The measurement locations listed in the third column of the table correspond to the numbers shown in Figure 3.1(a). Additionally, for the bidirectional case, the ISSC spectrum is used as well. Since there are two headings of origin, two wave spectra are specified. In Trial-1 to Trial-4 (both NW and AD cases), the significant wave heights *(Hs)* for head sea and beam sea are respectively 4.0 m and 2.5 m, with peak periods *(Tp)* described as 12 s and 9.5 s, respectively. In Trial-5AD, the *Hs* and *Tp* values for head sea are assumed to be 3.0 m and 12 s, while for beam sea, they are described as 4.0 m and 9.5 s. All bidirectional cases assume combination of two different measurement data for the filtering.

Table 3. 3 Case study variations description assuming total linearity for Semisub-A only

Spectrum type	Observation data	Measured location	Case name
Unidirectional spectrum	Pitch motion	22	Trial-NW* Trial-AD**
Bidirectional spectrum	Heave	1	Trial-1NW
	Strain around y-axis	12	Trial-1AD
		22	Trial-2NW
	Heave	1	Trial-2AD
	Strain around y-axis	10 and 22	Trial-3NW Trial-3AD
		10 and 12	Trial-4NW Trial-4AD
		10	Trial-5AD
	Pitch motion	22	

*NW: having only hydrodynamic load (no wind)

**AD: having both hydrodynamic and aerodynamic loads

The second type of data assumes the presence of nonlinearity as all data are based on NK-UTWind simulation. These include the response, wave, and TFs. In this part, a unidirectional wave spectrum in the form of a head sea is used for all assumed cases. The ISSC spectrum is employed in the simulations for each design, with a significant wave height *(Hs)* of 1.0 m and a mean period *(Tmean)* of 12.0 s for Semisub-A. The angular frequency range for Semisub-A is from 0.27 to 1.27 rad/s. On the other hand, Semisub-B assumes *Hs* and *Tmean* values of

0.846 m and 7.352 s, respectively, with a frequency range from 0.16 to 1.2 rad/s. These values are assigned to two load cases: one considering only hydrodynamic load and the other accounting for a combined load from waves and wind. These two variations are indexed as NW and AD, respectively. The inclusion of these two different load cases aims to examine the adaptability of the filter when considering a more complex nonlinearity problem caused by the coupling effect (Inoue, Adilah, Iijima, Oh, & Suzuki, 2020; Adilah & Iijima, 2021). The wind itself is simulated as a steady wind with a velocity of 10.0 m/s for both designs. A summary of the case variations and the details of their measurement data can be found in Table 3.4.

Table 3. 4 Case study variations fully based on NK-UTWind data

Design type	Observation data	Measured location	Case name
Semisub-A	Heave motion	1	A-1NW* A-1AD**
	Strain around y-axis	10	A-2NW A-2AD
		12	A-3NW A-3AD
	Pitch motion	22	A-4NW A-4AD
	Acceleration	1 (of heave)	A-5NW
		22 (of pitch)	A-6NW
Semisub-B	Strain around y-axis	8	B-1NW B-1AD
		20	B-2NW B-2AD
		8	B-3NW
	Pitch motion	1	

*NW: having only hydrodynamic load (no wind)

**AD: having both hydrodynamic and aerodynamic loads

Initially, in the early stages of the research, the response data included in the observation model mainly consisted of strain and nodal displacements. However, as the study progressed, it was discovered that acceleration responses would be more dependable, particularly in cases where the associated rigid body displacements were not entirely reliable across all frequency ranges due to the very high steepness of the RAO functions in the lower frequency region. This makes

the relative values of the RAO functions “appear” to be zero in the higher frequency domain. Furthermore, the possibility of combining two types of measurement data to improve prediction accuracy was explored, leading to the inclusion of case B-3NW in Table 3.4. A more comprehensive discussion regarding these matters can be found in Sec. 3.5.

Lastly, a fully experiment based data are incorporated to the filter. These include the responses for the input, wave for the reference, and TFs for the observation matrix. The experiment is carried out in a towing tank, Osaka university based on the design of Semisub-A with 1/50 scaling factor. Due to the data availability, the variation in cases based on experimental data is limited to a specific type of wave spectrum (ITTC spectrum, Hs=40 mm; T_{01} =1.56 s) representing a head sea, with the presence of aerodynamic damping introduced as a constant thrust generated by a fan. The load exerted by this fan is 5.0 N, which corresponds to the maximum thrust at the rated speed. The filtering outcomes obtained from two different observation points (point 11 and point 12, as indicated in Figure 3.1) will be compared. The transfer function specific to a certain wave height will then be tested with input waves of significant heights different from the prescribed wave height in order to assess its sensitivity. Additionally, the experimental model includes additional attachments of a cylindrical plate and a half ellipsoid at the substructure's bottom (see Figure 3.4(a)).

3.3 Wave prediction results (simulation based)

In this section, we present the results obtained from the filtering process when numerical data are introduced. The prediction using data assuming fully linear relationship between wave and response is first discussed in Sec. 3.3.1. This step is important mostly as the first check on the filter algorithm workability. In this part, the transfer functions are obtained using NK-UTWind, however, the wave and response data are generated separately based on the Equation (2.11) and (2.13). The filter ability to accurately predict different level of wave directional complexity (unidirectional and bidirectional waves) is discussed in this section. Subsequently, we delve into the estimation results using the more realistic external forces and response relationship in the context of FOWT. In this part the prediction is carried out fully based on NK-UTWind data in Sec. 3.3.2.

3.3.1 Prediction results assuming fully linear wave-response relationship

Firstly, prediction results assuming unidirectional wave is discussed. When a structure is exposed to a unidirectional wave, it means that the incoming waves are irregular but have a consistent direction of travel. In this case, the wave is assumed to move in the direction of head sea. Consequently, the number of heading directions (n_β) is one for the unidirectional wave scenario. However, the discussion in this first part focuses on the number of angular

frequencies that constitute the waves, as it holds more significance.

Other than that, in order to simplify the interpretation of results, the correlation coefficient (r_{xy}) is introduced. This is done to facilitate the analysis process, as relying solely on visual images can be misleading when numerous figures are presented. By using the correlation coefficient, a more accurate and comprehensive conclusion can be drawn. The correlation coefficient (r_{xy}) is selected because it directly quantifies the extent of linear correlation between two sets of data. In this scenario, the two sets of data are the reference wave and the predicted wave. The formula for calculating the correlation coefficient (r_{xy}) can be found in Equation (3.1) below, where X is the wave reference data and Y is the wave prediction data.

$$r_{xy} = \frac{\overline{XY} - \bar{X}.\bar{Y}}{\mathrm{sqrt}\left(\left(\overline{X^2} - \bar{X}^2\right).\left(\overline{Y^2} - \bar{Y}^2\right)\right)} \quad \text{(3.1)}$$

From a mathematical perspective, ocean wave spectra are typically modeled as continuous functions of frequencies. However, for the filtering process employed in this study, it is necessary to discretize these frequencies. This allows us to determine the number of elementary waves present in the spectrum. The challenge lies in obtaining the exact values of these frequencies, which is practically impossible. To overcome this issue, a series of trial and error operations is conducted. The objective is to identify the minimum number of frequency discretization (n_ω) that ensures both efficient and accurate algorithm execution. The chosen value for n_ω significantly impacts the size of the observation matrix ($\mathbf{M}$). A higher n_ω leads to a larger observation matrix and consequently increases computation time. Additionally, the effective minimum number of observation data (n_S) is also explored, and it is determined that 500 s of observation data with a sampling rate of 0.5 s (1000 data points) is suitable for this case.

After multiple attempts, it is observed, through visual inspection, that discretizing the unidirectional spectrum into 80 frequencies combined with 1000 observation data points yields predictions that closely align with the reference data (Figure 3.5), with its r_{xy} is found to be around 0.9. Discretizing the spectrum into 80 frequencies indicates that 160 state variables are introduced ($2n_\omega n_\beta$) for this specific prediction. However, even though the accuracy is found to be significant, it is expected that the prediction results should fit the reference almost, if not perfectly since in this part, it is assumed that the wave and response have a total linear relationship and the wave is simply the long crested type. Hence, an attempt to achieve a perfect fit is carried out by increasing the number of the elementary waves. When the number of elementary wave frequencies is slightly increased to 100, it is found that the results are closer to the expected outcome (see Figure 3.6), with its r_{xy} is found to be 0.99. Based on this, this

number of elementary waves frequency and observation data ($n_\omega = 100$ and $n_S = 1000$) are reckoned as a guidance when applying the Kalman filter in the bidirectional spectrum case.

Next, the findings based on the bidirectional wave data are discussed. A total of nine cases are examined for the prediction of bidirectional waves. Four out of the nine cases pertain to hydrodynamic loads only, while the remaining five cases represent combined load conditions. Each case involves different transfer functions based on the chosen measurement location. The accuracy of the Kalman filter in these predictions is influenced by the transfer functions used, which are known to be a sensitive factor.

Initially, the accuracy of the filter is assessed by considering the frequency discretization and the number of observation data. Based on the findings from the unidirectional wave case, a combination of $n_\omega = 100$ and $n_S = 1000$ is first explored. Similar to the previous case, 1000 observation data points correspond to a measuring period of 500 s. However, based on the direct observation, the results show inadequate agreement between the prediction and reference data considering the case are assumed to be linear in the context of its wave and response relationship. The correlation coefficient is found to be only as big as 0.70 (see Figure 3.7). Therefore, the number of observation data and frequency discretization are increased in order to find a better combination.

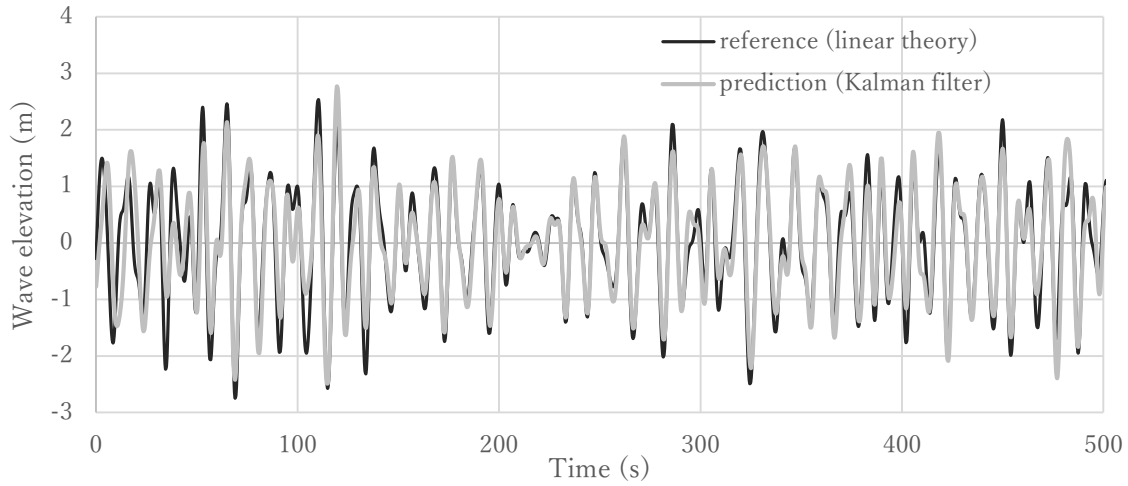

Figure 3. 5 Real-time comparison results of wave elevation from Trial-NW case for Semisub-A, unidirectional wave, assuming total linearity ($n_\omega = 80$, $n_S = 1000$)

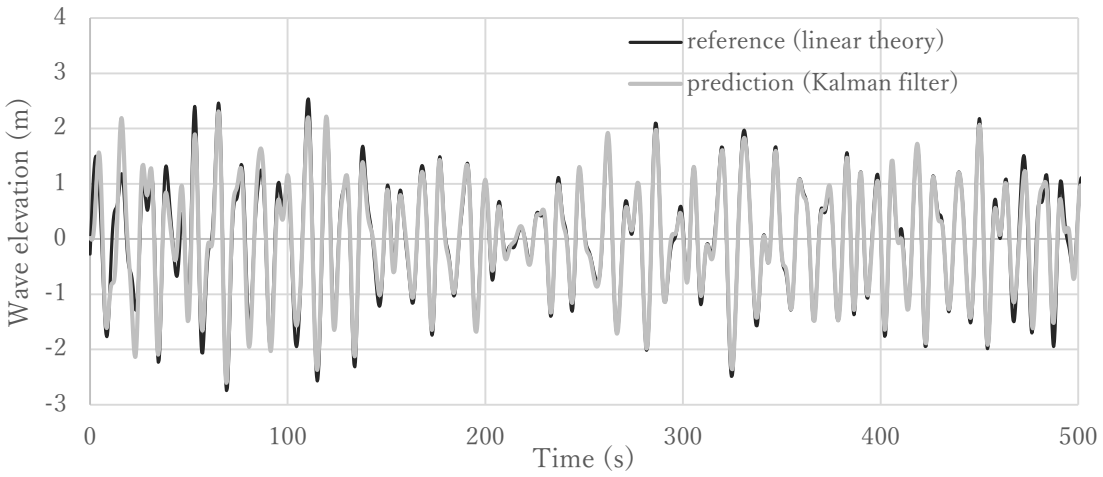

Figure 3. 6 Real-time comparison results of wave elevation from Trial-NW case for Semisub-A, unidirectional wave, assuming total linearity ($n_\omega = 100, n_S = 1000$)

In the case of bidirectional wave spectra, the state variables and observation matrix are doubled due to the inclusion of two directional waves for the heading angles. Consequently, increasing the number of discretized frequencies and measurement data leads to longer computation times. Thus, finding the combination with the minimum values of n_ω and n_S becomes crucial to reduce the computation time, especially when the system is further developed to handle more complex waves resembling real ocean surfaces with multiple heading angles.

Table 3. 5 Correlation coefficient values assuming fully linear wave-response relationship

Spectrum type	Observation data	Measured location	Case name	r_{xy}
Bidirectional spectrum	Heave	1	Trial-1NW	0.890
	Strain around y-axis	12	Trial-1AD	0.884
		22	Trial-2NW	0.891
	Heave	1	Trial-2AD	0.926
	Strain around y-axis	10 and 22	Trial-3NW	0.910
			Trial-3AD	0.873
		10 and 12	Trial-4NW	0.954
			Trial-4AD	0.962
		10	Trial-5AD	0.940
	Pitch motion	22		

*NW: having only hydrodynamic load (no wind)

**AD: having both hydrodynamic and aerodynamic loads

Figure 3.8 presents the prediction results from Trial-1NW assuming the combination of $n_\omega = 120$ and $n_S = 1200$. The correlation coefficient of this specific case is found to be 0.89. Based on this finding, the subsequent analysis for other cases will utilize 120 discretized frequencies (n_ω) and a dataset of 1200 observation data points, equivalent to a 600 s of measurement. Moreover, a correlation coefficient with the value around 0.9 is targeted for the bidirectional cases, since the wave is now more complex than the fully linear long crested (unidirectional) wave previously discussed. The prediction results (represented in the form of its corresponding r_{xy}) for all the adopted bidirectional cases are presented in Table 3.5. Based on the value in this table, it is confirmed that the filter consistently gives the desirable accuracy level for bidirectional wave case given different combination of TFs trends. In the next section, the discussion assuming the more realistic external loads and response relationship based on the NK-UTWind simulation data is given.

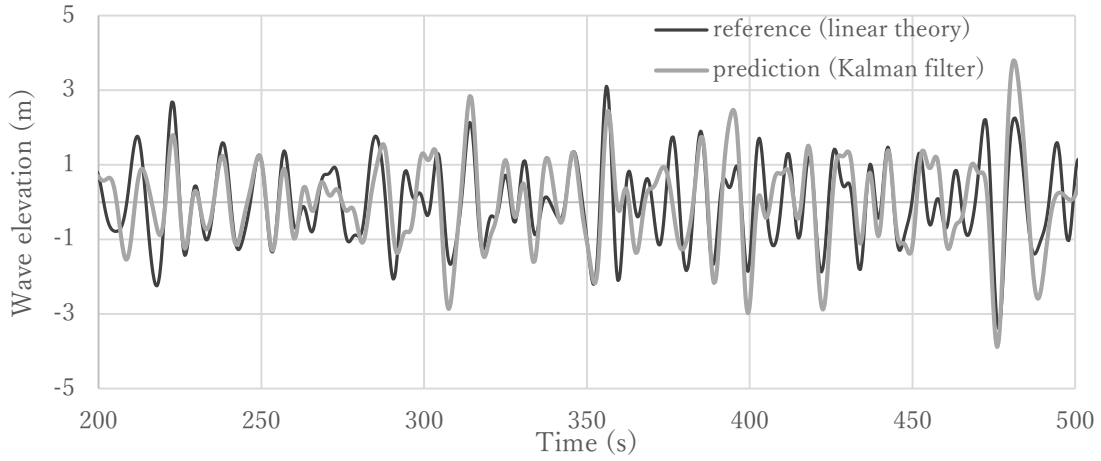

Figure 3. 7 Real-time comparison results of wave elevation from Trial-1NW case for Semisub-A, bidirectional wave, assuming total linearity ($n_\omega = 100$, $n_S = 1000$)

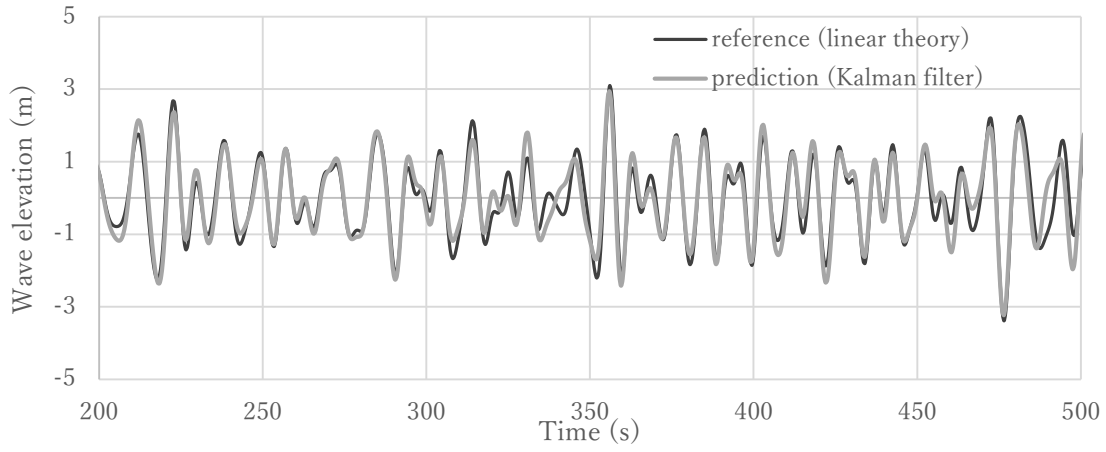

Figure 3. 8 Real-time comparison results of wave elevation from Trial-1NW case for Semisub-A, bidirectional wave, assuming total linearity ($n_\omega = 120$, $n_S = 1200$)

3.3.2 Prediction results fully based on NK-UTWind data

Real-time predictions of incoming wave values fully based on NK-UTWind data (see Sec. 2.4) have been conducted for two distinct designs of FOWT. Unlike ships, modeling an offshore wind turbine, particularly a floating type, is more complex due to its unique shape and functionality. The presence of coupling effects between wind and waves also contributes to nonlinearity when predicting waves based on the structure's responses. The outcomes of the filtering prediction are presented in this section of the report. A more detailed discussion of coupling effects will be further expounded upon in Sec. 3.6.

As explained in Sec. 3.2, the incoming wave for these cases is assumed to follow the ISSC spectrum for both the Semisub-A and Semisub-B designs. The wave approaches as a head sea along the positive-x axis. To determine the optimal number of elementary waves, a series of trial and error iterations were conducted. Through this process, it was discovered that the optimal number of elementary waves for Semisub-A is 80, while for Semisub-B, it is 55. These values are significant as they are closely linked to the discretization of the frequency spectrum. The discretization directly corresponds to the number of state variables determined by Equation (2.15), and it impacts the size of the matrix, thereby influencing computation time. Additionally, these values remain consistent throughout the entire analysis. Furthermore, the Kalman filter algorithm is applied to 1400 s of measurement data for the Semisub-A cases and 7200 s of measurement data with a sampling rate of 0.1 s for both designs.

Similar with the previous section, correlation coefficient (r_{xy}) is introduced to ease the data interpretation process, as relying solely on visual images can be misleading when numerous figures are presented. Table 3.6 presents the prediction results in terms of the correlation coefficient (r_{xy}) for each case study. The correlation coefficient value ranges from -1 to 1, where a value closer to 1 indicates higher accuracy. A value of 1 signifies a perfect match between the reference and predicted waves at every time step. To provide additional context, Figure 3.9 is included. Figure 3.9(a) illustrates the comparison results between the reference and predicted waves for case study A-1AD, which has the lowest correlation coefficient (r_{xy}). On the other hand, Figure 3.9(b) displays the comparison results for case study B-3NW, which has the highest accuracy among all the cases. Therefore, it can be observed that the time history comparison results for the other cases will fall somewhere between the patterns seen in Figure 3.9(a) and Figure 3.9(b).

In general, the wave prediction results using the Kalman filter for the Semisub-A design cases show less favorable outcomes compared to predictions for the other design. Further analysis reveals a distinct behavior where the accuracy of predictions varies when the Kalman filter is provided with different measurement data from different sensor locations. Upon closer

examination, it is concluded that the applied transfer functions, which are specific to each measurement data and location, have a more significant impact on the prediction results than the measurement data itself. In other words, the accuracy of wave predictions is highly dependent on the choice of transfer function used to relate the state variables and observation data, as seen in Equation (2.5). Therefore, specific criteria for selecting response transfer functions are necessary to achieve higher accuracy. This aspect will be further discussed in Sec. 3.5.

Table 3. 6 Correlation coefficient values for cases fully based on NK-UTWind data

Design type	Measured location	Case name	r_{xy}
Semisub-A	1 (heave)	A-1NW*	0.470
		A-1AD**	0.459
	10 (strain)	A-2NW	0.875
		A-2AD	0.607
	12 (strain)	A-3NW	0.535
		A-3AD	0.536
	22 (pitch)	A-4NW	0.663
		A-4AD	0.624
	1 (acceleration)	A-5NW	0.618
	22 (acceleration)	A-6NW	0.751
Semisub-B	8 (strain)	B-1NW	0.859
		B-1AD	0.829
	20 (strain)	B-2NW	0.854
		B-2AD	0.800
	1 (pitch) and 8 (strain)	B-3NW	0.968

*NW: having only hydrodynamic load (no wind)

**AD: having both hydrodynamic and aerodynamic loads

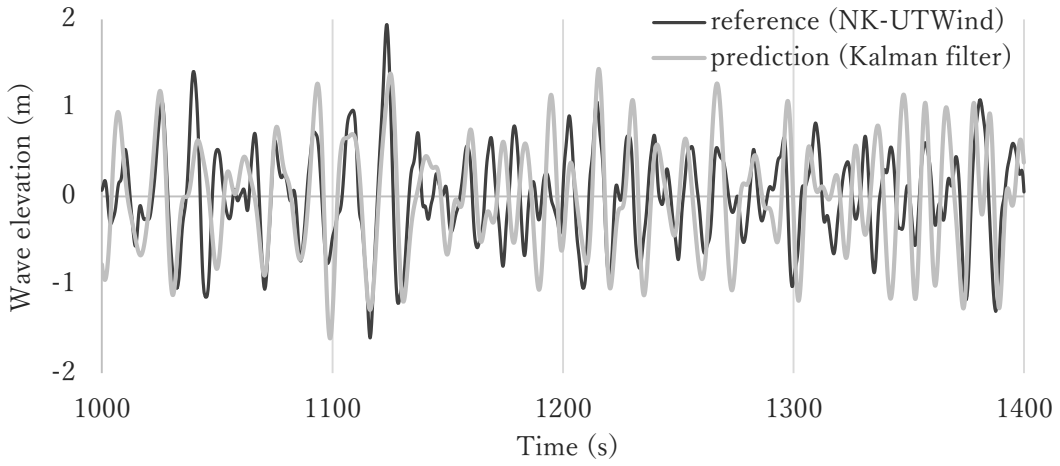

(a)

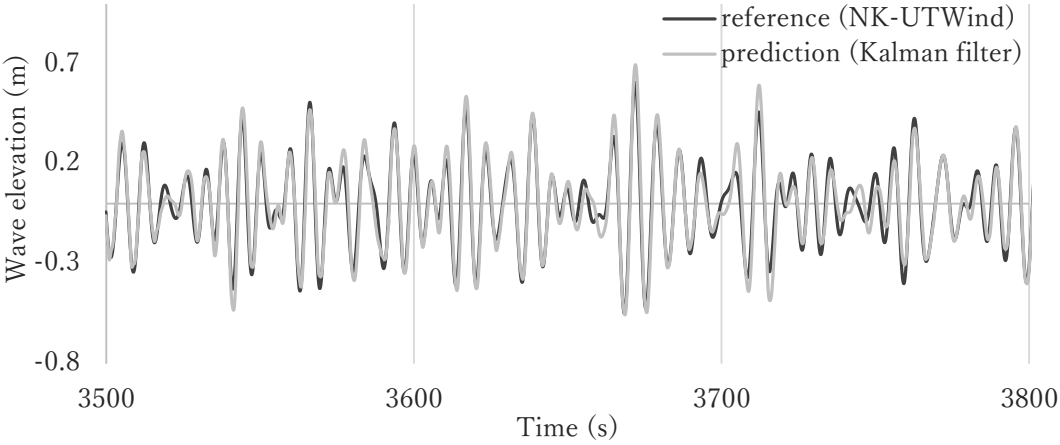

(b)

Figure 3. 9 Comparison between prediction and reference in real-time based on nonlinear simulation data (a) Case A-1AD (b) Case B-3NW

3.4 Wave prediction results (experiment based)

The experiment takes place in a towing tank, and its setup is illustrated in Figure 3.4. In order to predict the real-time wave elevation, the strain measured is utilized as the observed data. The observed wave is positioned 4.6 meters ahead of the FOWT to avoid any influence from wave diffraction and radiation effects. For this specific calculation, 120 elementary waves are assumed, and the strain data input consists of 90 s of data with a sampling rate of 100 samples per second. In this instance, two prediction cases are conducted based on the experimental data obtained. The strain data from two locations along the y-axis are used as input measurements,

and their respective transfer functions are incorporated into the filter as part of the observation matrix. These locations are identified as number 11 and number 12 in Figure 3.1(a). For simplicity, these cases are referred to as case A and case B, respectively.

Overall, the accuracy of predictions based on the experimental data is quite poor. The correlation coefficient (r_{xy}) values for case A and B are respectively found to be 0.49 and 0.44. To provide more clarity, the prediction results based on the strain data from location 11 (case A) are shown in Figure 3.10. Several factors could potentially contribute to the overall inaccuracy of the filter. Firstly, the experimental transfer functions are limited to a narrower frequency range compared to the range of wave frequencies encountered, primarily due to data availability. Secondly, these transfer functions were derived from responses under regular waves with a wave height of 36 mm, while this particular test was conducted using irregular waves with a significant wave height of 40 mm. The nonlinearity of hydrodynamic forces leads to transfer functions being specific to each wave height. Not only from combined loads, heave plates are also present in this experiment, hence causing a higher degree of nonlinearity in the system. Thirdly, it is possible that a longer period of time was required for the system to reach a steady state, since it has been found that some time is needed for the filter to reach steady state.

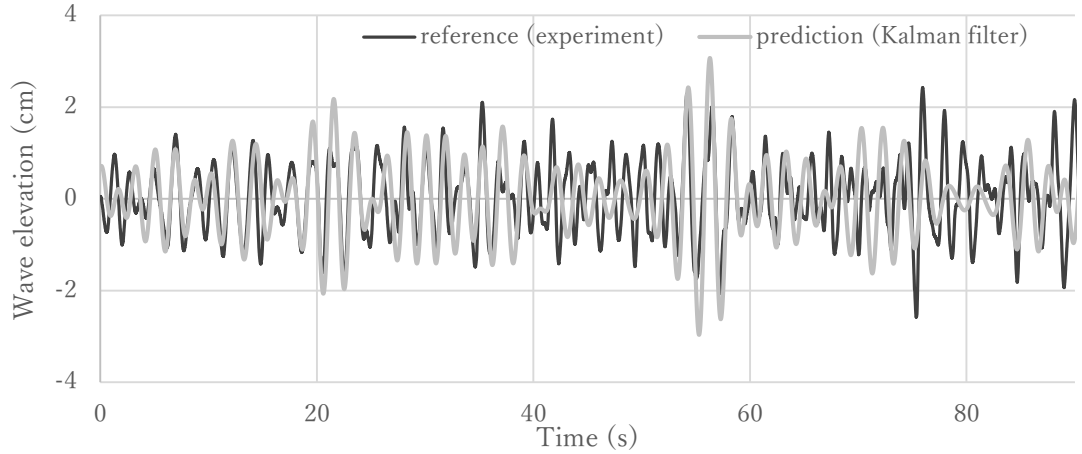

Figure 3. 10 Wave prediction results based on experiment data of Semisub-A adopting strain measurement from node 11 (case A)

As mentioned, a significant source of uncertainty comes from the nonlinearity of the response due to combined loads. Previous studies by Inoue et al. (2020) and Adilah & Iijima (2021) have examined the coupling effect of wind and wave and nonlinear loads in FOWT with respect to its response characteristics. For the semi-submersible type of FOWT, it has been observed that a combination of wind and wave loads leads to a reduction in amplitude response around resonance. In other words, the amplitude transfer function of a semi-submersible FOWT

subjected to both wind and wave loads is lower compared to when it is subjected to only wave loads. In cases where the transfer function is smaller than the "correct" transfer function, as in this situation, the predicted waves will be overestimated. It is crucial to incorporate transfer functions that consider the aerodynamic coupling effects.

3.5 Remarks on the filter dependency towards TFs

In this section, a discussion on the filter dependency towards the TFs is further elaborated. However, it is necessary to clarify that the discussion in this section will be mainly based on the simulation results fully based on the NK-UTWind data (Sec. 3.3.2). This is due to the fact that prediction results given in Sec. 3.3.1 is deemed to be not realistic enough due to the assumption of fully linearity between wave and response, while the experiment data only discussed cases containing combined loads (this will be mainly discussed in the next section).

The correlation coefficients in Table 3.6 suggest that a particular factor influences the filtering process in the Kalman filter algorithm. Upon closer examination of the algorithm, it becomes apparent that the Kalman gain found in Equation (2.8) is primarily responsible for improving the accuracy of estimation results during the correction step. This step is mathematically expressed in the Equation (2.8) to (2.10). Essentially, the Kalman gain determines how much the prediction results should be adjusted when provided with measurement inputs. Prediction steps can be found in Equation (2.6) and (2.7). Additionally, the response transfer functions play a crucial role in the algorithm. Not only do they directly link the state variables **(x)** with the measurement data **(y)**, but they are also integral to the calculation of the Kalman gain. Further analysis in this study confirms the importance of response transfer functions in achieving desirable wave prediction results using the Kalman filter. This section of the report explores the dependence and preferred types of transfer functions for wave prediction using the prescribed filtering model.

By examining the r_{xy} values in Table 3.6, it is evident that Semisub-B generally outperforms Semisub-A in wave prediction. Further comparison of the transfer functions associated with the two designs reveals that the magnitude of the transfer function in the amplitude domain (also known as the response amplitude operator or RAO) for each frequency is a factor that influences the performance of the filter algorithm. When the RAO remains significantly nonzero across all frequency ranges, the filter produces more accurate wave elevation predictions.

To provide clarification, Figure 3.11 presents a case study comparing two different transfer functions. The transfer functions in the amplitude domain for heave (node 1) and strain (node 10), used to make predictions for case A-1NW and A-2NW, respectively, are shown. The

magnitude at each point is normalized by the mean value of the function. Based on the r_{xy} values in Table 3.6, it is observed that case A-2NW achieves almost twice the prediction accuracy compared to A-1NW. This is because the RAO for case A-2NW maintains nonzero magnitudes when normalized. In contrast, the RAO for case A-1NW approaches zero when normalized within the frequency range of 0.8 rad/s to 1.2 rad/s, as depicted in Figure 3.11. To provide a visual representation of the accuracy of the filtering results, Figure 3.12 illustrates the prediction results for case A-2NW. This figure can be compared with Figure 3.9(a), which represents A-1AD, and has a similar correlation coefficient value to the prediction result from case A-1NW.

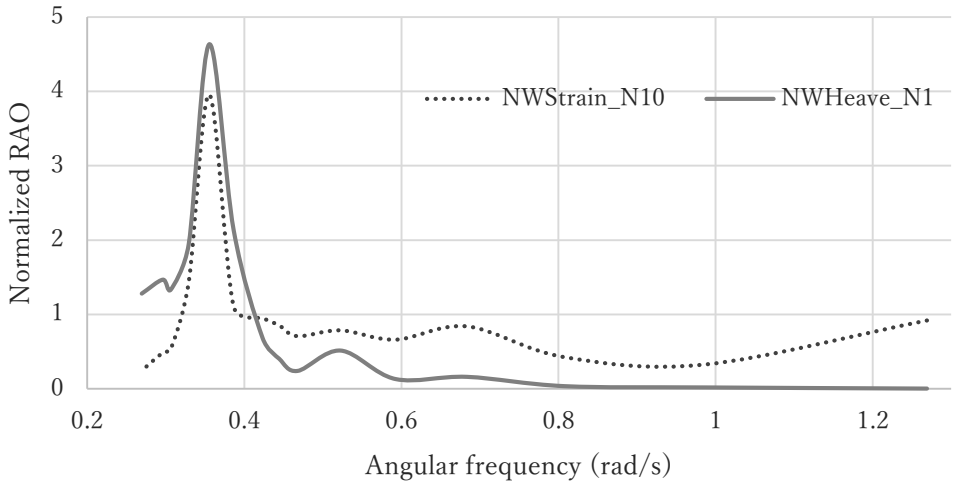

Figure 3. 11 Normalized RAO of heave at node 1 and strain at node 10 for Semisub-A

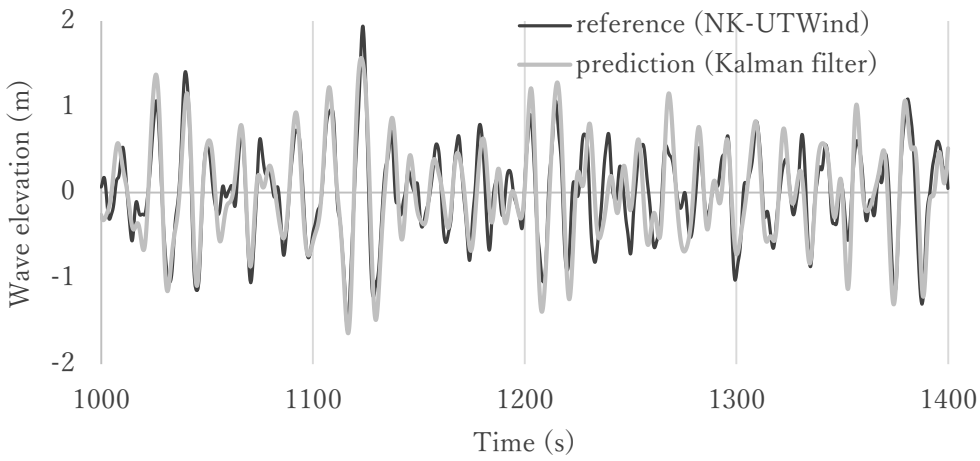

Figure 3. 12 Prediction results of Semisub-A case A-2NW based on nonlinear simulation data

The objective of any prediction endeavor is to achieve the highest possible accuracy within the limitations of the system and model employed. Consequently, it is suggested that incorporating acceleration responses may enhance the prediction results in this case, as their magnitudes are proportional to the square of the corresponding frequency. Based on this rationale, cases A-5NW and A-6NW are introduced. Analysis reveals that the r_{xy} values for these cases are indeed higher than those using nodal displacement. Therefore, it is recommended to include acceleration responses in future studies. Additionally, combining two types of measurements is also advised, as it further improves accuracy. This finding is deduced from the comparison between case B-1NW and B-3NW.

3.6 Remarks on the nonlinearity effects from combined loads

This section of the chapter discusses the interaction between wind and waves and how they affect the filtering ability to accurately predict wave elevation. Results from 3.3.2 and 3.4 will be mainly discussed. Previous studies by Adilah & Iijima (2021) and Inoue et al. (2020) have highlighted that the combined load on floating offshore wind turbines (FOWTs) does not follow a linear relationship. Therefore, it is necessary to perform prediction analysis that considers the nonlinearity of the system, especially for FOWT structures, as they are typically subjected to combined loads due to their functional nature.

The results of the filtering, assuming the presence of nonlinearity, are available in Table 3.6 as correlation coefficient values. Comparing these results with the cases without nonlinearity, it can be concluded that most of the cases with combined loads have slightly lower accuracy, except for the A-2s cases. Further examination reveals that the cause of the accuracy discrepancy lies in the amplitude response transfer function associated with each measurement. For example, the correlation coefficient values between case A-1NW and A-1AD are quite similar, indicating that the response transfer functions in the amplitude domain are comparable between the combined loads case and the wave load only case. This is illustrated in Figure 3.13. On the other hand, the coupling effect has a greater impact on the strain response at node 10 in the Semisub-A design, particularly around the resonance frequency, as depicted in Figure 3.14. Due to this coupling effect, the measured response used in the Kalman filter algorithm becomes more contaminated, resulting in less accurate prediction results. This finding is further proven based on the experiment-based prediction results given in the Sec. 3.4. When experiment data are used to estimate the waves, it is found that the prediction accuracy is generally low. Though several factors could cause this inaccuracy as discussed in Sec. 3.4, it is fair to deduce that especially in the context if case A, nonlinearity from combined loads plays a significant role to the filter ability to find accurate wave prediction.

Based on these findings, it can be concluded that understanding the nonlinearity effect on

FOWT responses is crucial for determining the appropriate location and type of response to be used when predicting incoming waves using the Kalman filter algorithm. Additionally, comprehensive experimental data is needed to further examine the nonlinearity effect in detail.

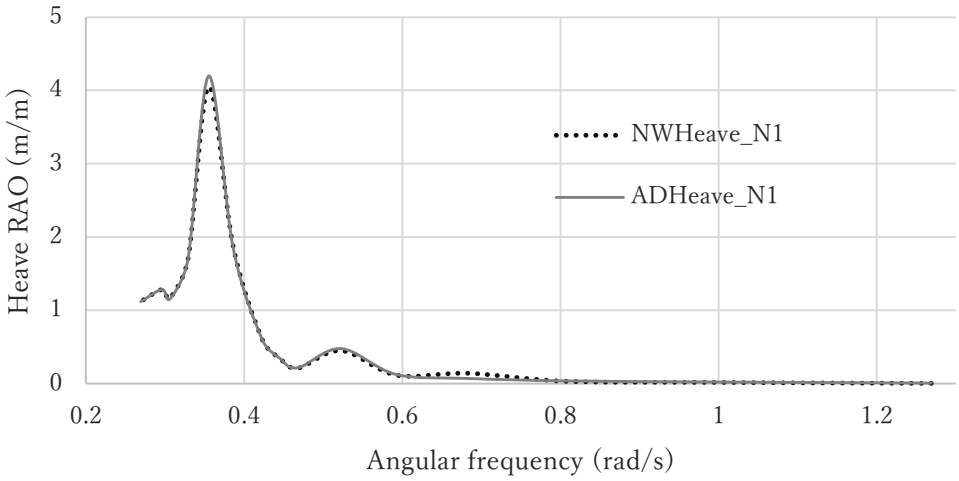

Figure 3. 13 Heave RAO comparison (node 1) between case A-1NW and A-1AD

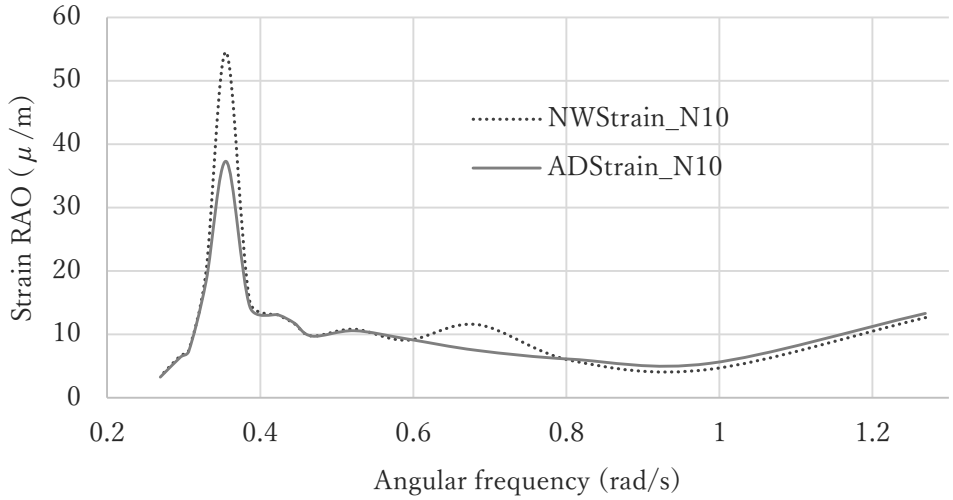

Figure 3. 14 Strain RAO comparison (node 10) between A-2NW and A-2AD

3.7 Summary

In this chapter, the real-time prediction results using Kalman filter based on two different designs of FOWTs (Semisub-A with peaky RAO and Semisub-B with less peaky RAO) are compared. In general, the prediction results for Semisub-A exhibit lower accuracy compared

to Semisub-B. This discrepancy can be attributed to the response characteristics of the respective designs. Specifically, Semisub-B displays less pronounced peaks in its response, leading to more accurate predictions. Combining measurement data from different sensors can be done to improve the prediction accuracy. Additionally, the impact of nonlinearity from coupling effects of wind and wave on the filtering results is discussed. Certain cases are found to be less affected by nonlinearity compared to others, depending on the structural response under combined loads. The findings on the nonlinearity effects towards the filtering results is further solidified after analyzing the prediction results based on experimental data of Semisub-A. However, further validation through additional experiment data points is needed, especially since the available experiment data is limited only for cases where combined loads, and heave plates (which caused further nonlinearity on the overall response) are present. Another experiment considering cases without aerodynamic load from the fan is needed to be carried out as well to provide a more accurate understanding on the Kalman filter's dependence on TFs.

In summary,

- Prediction results for Semisub-A generally have lower accuracy compared to Semisub-B due to response characteristics.
- Semisub-B has less pronounced response peaks, leading to more accurate predictions.
- Combining measurement data from different sensors can enhance prediction accuracy.
- Nonlinearity from wind-wave coupling affects filtering results, with some cases being less impacted than others depending on structural response.

This page is intentionally left blank

Chapter 4
Future predictions and causality effects

4.1 Causality effects

Throughout the decades, there have been several methods introduced to cope with the deterministic water waves prediction. Some examples of these methods are predictions based on nonlinear dynamics (Klein, et al., 2020; Huchet, Babarit, Ducrozet, Gilloteaux, & Ferrant, 2021; Hlophe, et al., 2021), predictions based on machine learning (Tanaka, Hamamichi, Wada, Takagi, & Imamura, 2018; Duan, Ma, Huang, Liu, & Duan, 2020), and predictions based on linear time-invariant (LTI) system (Naaijen, Van Oosten, Roozen, & Van 't Veer, 2018; Al-Ani, Belmont, & Christmas, 2020; Iida & Minoura, 2022). Out of these methods, LTI-based water waves prediction offers the more robust and faster computational time compared with the rest of the methods, with the Fourier coefficients estimation technique being the most successful (Iida & Minoura, 2022). This method is essentially the water waves prediction technique adopted in this study, as seen in the formulation elaborated in Sec. 2.3. The wave prediction method using the Kalman filter algorithm is extended to find the future wave and response predictions. This will be further explained in the next section. This section discusses the non-causality that arises when a water wave prediction is carried out in real-time. Firstly, another technique for LTI-based water waves prediction by calculating the convolution integral between the impulse response function and an input signal is discussed. The link between this method, future predictions based on Kalman filter, and the zero-approaching state of the non-causality phenomenon is discussed by the end of this chapter.

The convolution integral is a mathematical operation that combines two functions to produce a third function, which represents the merging or interaction of the original functions. It is a fundamental concept in calculus and is widely used in various fields, including signal processing, image processing, and physics. Mathematically, the convolution of two functions referred as $f_c(t)$ and $g_c(t)$ is denoted by $(f_c * g_c)(t)$ and is defined as:

$$(f_c * g_c)(t) = \int f_c(\tau) * g_c(t-\tau)\, d\tau \quad \cdots\cdots (4.1)$$

where $\int$ represents the integral sign, $f_c(\tau)$ and $g_c(t-\tau)$ are the functions being convolved, and $d\tau$ is the differential element used for integration.

To understand the intuition behind the convolution integral, consider $f_c(t)$ as an input signal or function and $g_c(t)$ as a response or kernel function. The convolution operation determines the output signal or resulting function at each point in time by calculating the weighted sum of the products of the input signal and the kernel function, shifted and scaled appropriately.

The convolution integral involves the following steps:

1. Reversing the kernel function: The kernel function $g_c(t)$ is reversed or flipped along the time axis, which is necessary to align the corresponding values of $f_c(t)$ and $g_c(t)$ for multiplication during integration.

2. Shifting and scaling: The reversed kernel function $g_c(-\tau)$ is shifted to the right by an amount of t, aligning it with the current point in the integration. Additionally, the function may be scaled by a factor depending on the specific convolution equation being used.

3. Multiplying and integrating: At each point in time, the values of $f_c(\tau)$ and $g_c(t-\tau)$ are multiplied together, and the products are summed up over the entire range of integration, represented by the integral sign. This multiplication and summation process is performed for every value of t.

4. Obtaining the resulting function: The outcome of the convolution integral is a new function $(f_c * g_c)(t)$, which represents the combined effect of the original functions $f_c(t)$ and $g_c(t)$. It describes how the input signal is transformed or modified by the kernel function over time.

The convolution integral possesses important properties, including commutativity $(f_c * g_c) = (g_c * f_c)$, associativity, linearity, and time-shifting. These properties make convolution a powerful tool for analyzing signals, systems, and understanding the interactions between different functions.

In the 1960s, Davis & Zarnick derived the analytical solution of the impulse response function under the deep water assumption (Davis & Zarnick, 1966). However, it was found that this impulse response function is non-causal. In mathematics, causality refers to the concept that the cause of an event or phenomenon must precede its effect in time. It is a fundamental principle that governs the relationship between cause and effect and is widely used in various branches of mathematics, such as calculus, differential equations, and signal processing. Causality can be understood through the concept of time ordering. If there is a causal relationship between two events, it means that the cause event must occur before the effect

event. In the context of mathematical models or systems, causality plays an important role in determining the behavior and validity of the model. For example, in the study of differential equations, a causal system is one in which the output at any given time depends only on the input values at earlier times, not on future inputs. This ensures that the system's response is consistent with the principle of causality, as the output is determined solely by the past inputs. Causality is also closely related to the concept of time delay. If a system exhibits causality, it means that any changes or perturbations in the input will only affect the system's output after a certain time delay. This time delay is essential for maintaining the cause-effect relationship and ensuring that the system behaves in a physically meaningful way.

In summary, causality in mathematics refers to the principle that the cause of an event must precede its effect in time. It is a fundamental concept used to establish relationships between variables, validate mathematical models, and ensure the consistency of mathematical systems with the laws of cause and effect. Causality is often associated with the notion of predictability. In a causal system, the future behavior can be predicted based on the past and present inputs. This property is particularly important in areas such as signal processing, control systems, and differential equations, where understanding causality allows for the analysis and prediction of system behavior. It is worth noting that not all mathematical functions or systems are causal. Some systems may exhibit non-causal behavior, where the output depends on future values of the input. However, causality is a fundamental assumption in many mathematical models and is often desired in practical applications to ensure logical and predictable behavior. Causality implies that a signal can be physically realized in real time (Tan, 2008), hence it is important to ensure that the impulse response function is causal as water waves prediction is time-dependent.

While it was found that the water waves non-causality is caused by the waves dispersion (Falnes J. , 1995; Falnes & Kurniawan, 2020), adopting window function and shifting the phase can be done to cope with the non-causality problem (Belmont, Horwood, Thurley, & Baker, 2006). However, the method then is only valid for deep water waves, while most offshore structures—including FOWTs, are usually installed in finite-depth water. Iida & Minoura have analytically derived the impulse response function for finite-depth water between two points and found that the distance between the two points highly influences the causality of the impulse response solution (Iida & Minoura, 2022). To give a further explanation, Figure 4.1 is given. Noted that for the discussions from here onwards (to the end of this sub-chapter), every variable corresponds to length is non-dimensionalized by the water-depth (d) and variables correlated to time is non-dimensionalized by the square-root of the water depth divided by the gravity acceleration ($\sqrt{d/g}$).

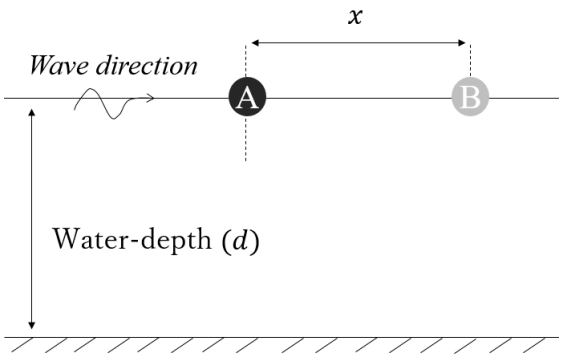

Figure 4. 1 Point locations assumed for the convolution integral

Supposed that there are two points on the water surface (points A and B) with non-dimensionalized distance of X ($\mathrm{X} = x/d$) and the waves is propagating towards x-positive direction. The time history of wave elevation at point B (η_B) then can be found based on convolution integral of the impulse response function (h) and wave elevation history at point A (η_A). This can be mathematically written as Equation (4.2). In the case of finite-water depth water, it has been analytically calculated that the impulse response function is as shown in Equation (4.3), where the extensive derivation of this function can be found in Iida & Minoura's article (Iida & Minoura, 2022).

$$\eta_B(t) = \int_{-\infty}^{+\infty} h(\tau)\eta_A(t-\tau)d\tau \quad \cdots\cdots (4.2)$$

$$h(t) = \begin{cases} \left(\frac{2}{\mathrm{X}}\right)^{\frac{1}{3}} Ai(\alpha) & \text{on } \ t \le t_0 \\ \left(\frac{2}{t}\right)^{\frac{1}{3}} Ai(\beta) & \text{on } \ t_0 \le t < t_1 \\ Re\left[\frac{1}{\pi} c_g(k_0)\sqrt{\frac{2\pi}{t|\omega''(k_0)|}} e^{i\left(\omega(k_0)t - k_0\mathrm{X} - \frac{\pi}{4}\right)}\right] & \text{on } \ t \ge t_1 \end{cases} \quad \cdots\cdots (4.3)$$

where $\alpha = (\mathrm{X}-t)(2/\mathrm{X})^{1/3}$ and $\beta = (\mathrm{X}-t)(2/t)^{1/3}$

where $Ai(-)$ is the first kind of Airy function, $t_0 = \mathrm{X}$, and t_1 is the intersection between the middle and the last function in the Equation (4.3) when the two are plotted and compared. Moreover, k_0 indicates the stationary phase points of wave number k and they are used to calculate the angular frequency (ω) and its first (also denoted as group velocity, c_g) and second derivative used in the last function in Equation (4.3). They are further expressed as Equation (4.4), (4.5), and (4.6), respectively.

$$\omega(k) = \sqrt{k \tanh k} \quad \cdots\cdots (4.4)$$

$$\omega'(k) = \frac{d\omega}{dk} = \frac{1}{2}\sqrt{\frac{\tanh k}{k}}\left(1 + \frac{2k}{\sinh 2k}\right) \quad \cdots\cdots (4.5)$$

$$\omega''(k) = \frac{d^2\omega}{dk^2} = \frac{1}{4k}\sqrt{\frac{\tanh k}{k}}\left(\frac{4k^2}{\sinh^2 2k} - 1\right) + \frac{1}{2}\sqrt{\frac{\tanh k}{k}}\left(\frac{2}{\sinh 2k} - \frac{4k}{\sinh 2k \tanh 2k}\right) \quad \cdots\cdots (4.6)$$

As it has been discussed, causality criteria are necessary to be fulfilled for the time domain water waves prediction, and it is found that for the case of finite-depth water, the non-causality phenomenon for the impulse response function solution changes for different X value. To give further understanding, Figure 4.2 is presented. Here, two different plots of the impulse response functions for different X values are shown. Based on this figure, it can be visually understood that the bigger the value of X, the "beginning" of the impulse response function is more "shifted" to the right, hence indicating causality. This is plausible since mathematically speaking, a non-causal system is indicated by $f(t) \neq 0$ when $t \leq 0$, which in this case will be bound to happen if the value of X is smaller than three, roughly. In other words, it can be concluded that the non-causality effects ought to be practically negligible if two different points are introduced, and only if the distance between the two points is far enough. This distance should be at least equal to three when non-dimensionalized with the water-depth ($x/d \geq 3$), as mentioned prior.

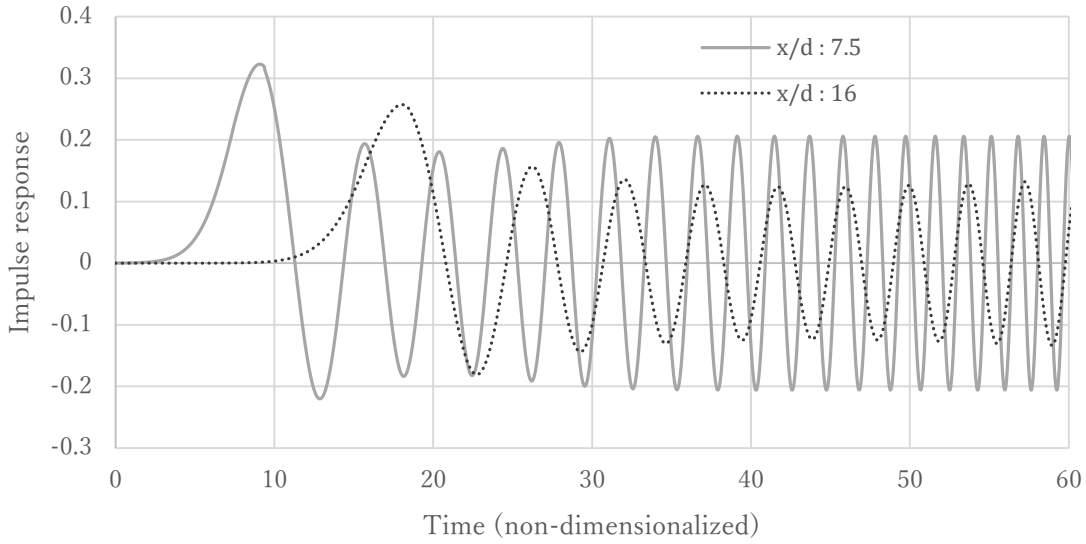

Figure 4. 2 Impulse response function plots of different X, all values are non-dimensionalized

4.2 Future wave and response prediction based on the Kalman filter

In this part, the method utilized to obtain the future predictions is described. Identical with the convolution integral-based prediction, the future predictions are carried out after introducing spatial distance relative to the reference point where the waves are first identified using the Kalman filter algorithm (see Figure 1.3). The causality criteria discussed previously is implemented. The causality criteria are applicable here as well due to the fact that the water wave prediction based on the convolution integral is principally the same as the Fourier coefficients prediction based (which are the state variables of the Kalman filter algorithm). Given the same problem definition, the two methods are principally the comparable as either method provides the time domain solution to Equation (2.11). The main difference is that convolution integral provides an analytical solution while the Kalman filter approaches the problem numerically.

To further elaborate, Equation (4.7) is presented. This equation is the basis of the future prediction calculation after spatial distance is introduced. In other words, after Fourier coefficients (a and b) are found via the Kalman filtering, the wave profile at x-meter away from a point of reference (in this case, where the first model is located) can be found using Equation (4.7), where k is the wave number and x is the relative distance to the point of reference. Further, given $n_\beta = 1$ and $y = 0$, Equation (4.7) is then just another form of Equation (4.2) which proves the point that causality criteria applicable for wave prediction via convolution integral should also be applicable for the Kalman filter based prediction. As explained in the previous sub-chapter, when spatial distance is introduced, causality should be practically achieved when the ratio between two points distance and the water-depth equals to at least three ($x/d \geq 3$). Hence, this ratio limitation is incorporated to this study and dictates the tank and model set-up in general to ensure the non-causality phenomenon is avoided. Further technical details on these matters are described in the next chapter. Another thing worthy to mention is that the convolution integral could only be utilized if the input wave is defined as long-crested. Theoretically, the ocean waves may be described as an addition of multiple long-crested waves. Due to this reason, wave prediction via the Kalman filter algorithm is more realistic as it accounts for wave directionality decomposition.

$$\eta_{xy}(x,y,t) = \sum_{q=1}^{n_\beta}\sum_{p=1}^{n_\omega} a_{p,q}\ \cos(\omega_p t + \phi) + \sum_{q=1}^{n_\beta}\sum_{p=1}^{n_\omega} b_{p,q}\ \sin(\omega_p t + \phi) \quad \cdots\cdots (4.7)$$

where $\phi = -k_p x \cos\beta_q - k_p y \sin\beta_q$

Since the future wave prediction is carried out in x-meter away from a point of reference where structure responses are not part of the input data. Hence, those responses then may be prescribed as another unknown variable that can be determined based on the predicted future waves due to the existed theoretical dependency between input wave, response, and transfer functions. Mathematically, this can be further expressed as shown in the Equation (4.8).

$$Y_{xy}(x,y,t) = \sum_{p=1}^{n_\beta}\sum_{q=1}^{n_\omega} a_{p,q}\, G(\omega_p,\beta_q)\cos\theta_{pq} + \sum_{q=1}^{n_\beta}\sum_{p=1}^{n_\omega} b_{p,q}\, G(\omega_p,\beta_q)\sin\theta_{pq} \quad \cdots\cdots\cdots\cdots (4.8)$$

where $\theta = (\omega_p t + \varphi(\omega_p,\beta_q) - k_p x\cos\beta_q - k_p y\sin\beta_q)$

4.3 Possible offshore wind farm arrangement

This section explores a possible offshore wind farm arrangement considering wake effects, a phenomenon that will significantly reduce the wind velocity and increase the turbulence intensity of downstream wind turbines. The explanation on the realistic application of the proposed future predictions based on the Kalman filter in the wind farm is also discussed.

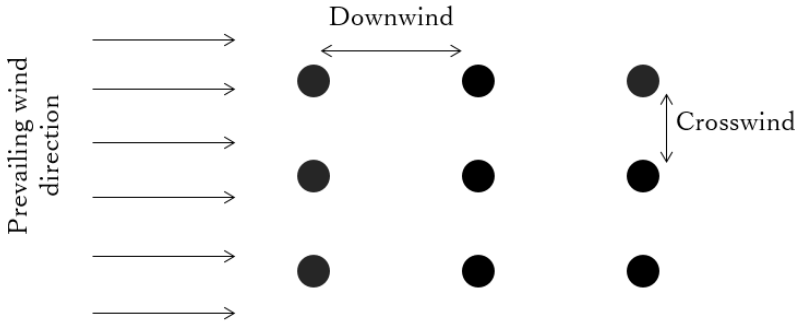

Figure 4. 3 Wind direction, downwind, and crosswind

When studies on the performance of an individual wind turbine are carried out, the calculations typically yield results based on the highest-rated power, leading to significant errors in the calculation of the levelized cost of energy (LCOE). Additionally, relying solely on the performance of a single wind turbine can result in inaccurate estimations of downwind and crosswind distances (see Figure 4.3), leading to incorrect calculations of the number of turbines required for a specific production (Hassania, Helgadóttir, & Riedel, 2023). Ragnarsson et al. (Ragnarsson, Oddsson, Unnthorsson, & Hrafnkelsson, 2015) provided LCOE calculations for the Búrfell site, an onshore wind site in Iceland, based on assumptions of seven rotor diameters (7D) downwind and four rotor diameters (4D) crosswind. However, they did

not account for the wake loss effect, which significantly impacts both the LCOE and the financial aspects of the project. Hence, it is important to consider the wake loss effect when designing a wind farm, not only for the onshore farm but also the offshore ones.

In wind farm layout analysis, six well-known wake loss models are commonly used. These models are Jenson-Katic, Larsen, Frandsen, Gaussian-Bastankah, Porté-Agel (BPA), and Gaussian—in which further divided into Xia and Archer (XA), and Geometric (Cristina, et al., 2018). The literature extensively discusses the Jensen-Katic and XA models as recommended options among the various wake loss models due to their consistent performance across different directions and wind farms. The Jensen-Katic model is particularly suitable for layout optimization involving annual energy production, as it exhibits satisfactory performance in terms of the correlation coefficient. On the other hand, the XA model is well-suited for aligning the wake loss model with the desired direction.

According to previous literature (Manwell, McGowan, & Rogers, 2004), wind farms that adopt a configuration with 8-10 rotor diameters (D) in the downwind direction and 5 rotor diameters in the crosswind direction experience array losses below 10%. Recent study conducted by Hassania et al. (Hassania, Helgadóttir, & Riedel, 2023) revealed that opting for a downwind distance of 10 times the rotor diameter (10D) will yield significantly improved power output. These findings are used as guidelines to describe the possible FOWTs arrangement in the wind farm proposed in this section.

As explained, when designing a wind farm, wake loss effect should be considered as it influences the total windfarm power generation. A variable that effects the recommended distance between wind turbines would be the rotor diameter (D). Until this report is being written, offshore wind turbines commonly had capacities ranging from 6 to 12 megawatts (MW). These larger turbines have rotor diameters typically exceeding 150 meters and are designed to capture more energy from the wind, thereby improving the overall cost-effectiveness of offshore wind farms. It's worth noting that the offshore wind industry is rapidly evolving, and larger capacity turbines are being developed and deployed. Newer turbine models with capacities of 14 MW or even higher have been introduced. Typically, as the capacity of a wind turbine increases, so does the rotor diameter. In the range of 12 to 14 MW, which was the highest commonly available capacity at that time, the rotor diameters ranged from approximately 200 to 230 meters. If it is assumed that the FOWT in the wind farm has 200 m rotor diameters, then the downwind distance should be 10 times larger than D, that is 2 km apart from one another, while the crosswind spacing would be as long as 5D, or 1 km. To give more concrete example, a fully commissioned offshore wind farm from The Hornsea Project is discussed.

The Hornsea Project (Ørsted, 2023), located off the coast of Yorkshire, England, is one of the largest offshore wind farms in the world in which primarily utilizes fixed-bottom wind turbines since the site is considered shallow water. The project consists of multiple phases. These phases are referred as Hornsea Project 1, Hornsea Project 2, Horsea Project 3, and Hornsea Project 4, with Hornsea Project 1 being fully commissioned in December 2019 in which the total capacity is 1.2 GW, while Hornsea Project 2 is fully commissioned in August 2022 with total capacity of 1.4 GW. With its completion, Hornsea Project 2 surpassed Hornsea Project 1 as the largest offshore wind farm globally currently. Figure 4.4 presents the layout of the wind turbines indicated by blue dots in Hornsea Project 1 and 2 (4C Offshore, 2023). For Hornsea Project 1, the average distance between wind turbines is approximately 1.2 kilometers, using 7 MW turbines with 154 m rotor diameters.

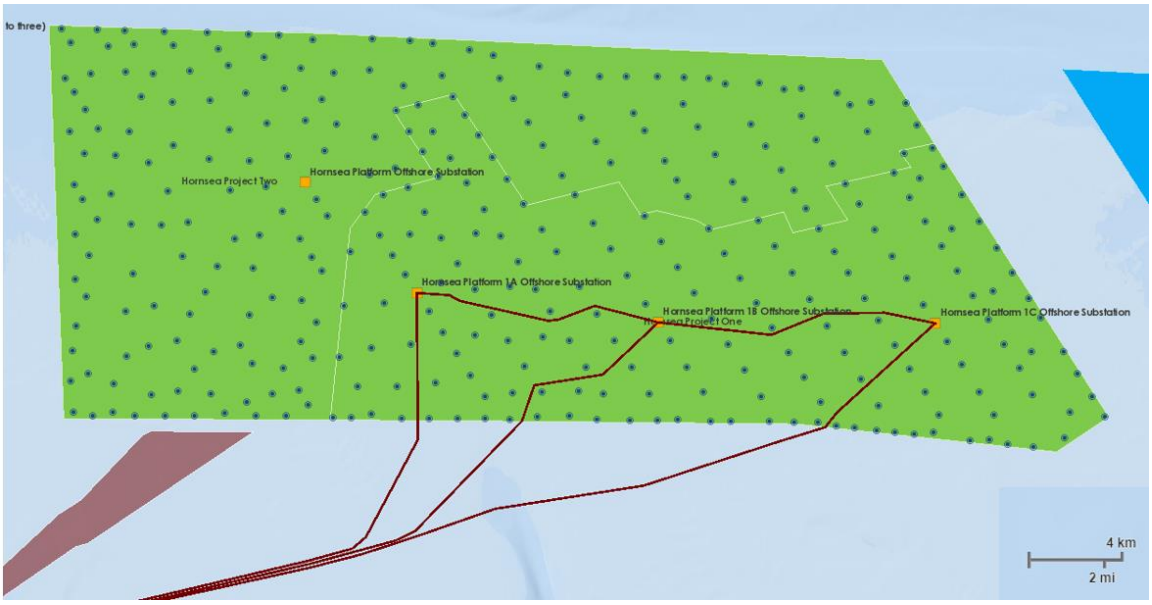

Figure 4. 4 Wind turbine layout in Hornsea Project 1 and 2

Floating offshore wind turbines—which are the targeted structure, on the other hand, are designed for deeper waters where fixed-bottom foundations are not feasible or economically viable. As discussed in Sec. 4.1, in order to ensure the causality for future predictions, the ratio of spacing and water depth should be at least equal to three ($x/d \geq 3$). Since the turbines is targeted to be floating, deeper water assumption should be adopted to find the ratio. As a rule of thumb, sites with at least 200 m of water depth can be considered appropriate for FOWTs installation. Reiterating the prediction arrangement presented based on Figure 1.3(a), it can be agreed upon that the "main" filtering is carried out in the black dots, where the Fourier coefficients are first being estimated. After incorporating the spatial distance as explained in Sec. 4.2, the future predictions at gray dots can be determined. Based on this, it becomes apparent that the spatial distance is varied depending on the location of the gray dots relative

to the black dots. However, the smallest x/d is found to be 5 if it is assumed that the spacing between each turbines is around 1 km. This means that in any case the causality limitation is fulfilled for the case of deeper water wind farm. Moreover, it is expected that the spatial distance between turbines will become bigger and bigger due to the larger turbine expected to take over the market as explained previously. Therefore, it is expected that the findings of the study can be feasibly applied to both current and upcoming floating wind farm projects.

Chapter 5
Future predictions results on multiple floating bodies

5.1 Subject structure and tank set-up

The experiment takes place at Osaka University in a two-dimensional tank. Based on the TFs of the model, the tank test can be separated into two phase. Phase 1 accounts for the experiment considering resonance free models, while phase 2 is the test that utilizes models with resonance. Figure 5.1(a) and (b) present resonance free model, while Figure 5.1(c) and (d) show the model with resonance. The drafts of the model are 12 and 59 mm for the resonance free model and model with resonance, respectively. The primary component of both floating models is a rectangular box made of 3 mm thick acrylic plate.

For the resonance free models, the dimensions of the box are as follows: length (L) of 500 mm, width (W) of 280 mm, and height (h) of 40 mm. The model's draft is set at 12 mm using lead (Pb) as ballast. A vertical tower, made of cylindrical acrylic with an outer diameter of 30 mm and an inner diameter of 26 mm, is positioned at the center of the model. Atop the tower, a 50 mm rectangle made of 3 mm acrylic plate is attached. The tower and rectangle plate are important for ensuring the accuracy of optical tracking measurements, which will be discussed further in the subsequent section. The overall height of the model from keel to top measures 311.3 mm.

For the models with resonance, the main box is in general shorter in x direction and taller in z direction. To be exact, the length (L), width (W), and height (h) of the main floater for this model are respectively 200 mm, 280 mm, and 80 mm. Similar to the resonance free model, a vertical tower, made of cylindrical acrylic with an outer diameter of 30 mm and an inner diameter of 26 mm, is positioned at the center of the model. A 50 mm × 50 mm plate with thickness of 3 mm is also placed on top of the cylindrical tower. The total height from keel to tower top for this model is 317 mm. Steel is used as ballast to reach draft of 59 mm.

A total of three models, all having the same design, are taken into consideration for each phase of the experiment. These models are placed approximately 3 m apart from each other within the two-dimensional tank. For experiment considering resonance free models (or phase 1), first model is positioned at a distance of 2 m from the wave-maker. To distinguish them based

on their proximity to the wave generator, they are named Model 1, Model 2, and Model 3 respectively, starting from the nearest one. The water depth (d) is set at 0.4 m. In relation to Model 1 (which serves as the reference point), the x/d ratios for Model 2 and Model 3 are roughly 7.5 and 16 respectively, meeting the criteria for causality (see Chapter 4). The tank has a breadth of 0.3 m and a length of 14 m.

The next experiment considering the models with resonance (phase 2) is carried out in the same 2D tank assuming the same water depth (0.4 m). For this phase, the distance between Model 1 and Model 2 is around 3.5 m, while the space between Model 2 and Model 3 is approximately 3.8 m in the tank. Model 1 is located around 2 m from the wave maker. The x/d ratios for Model 2 and Model 3 from Model 1 are about 8.7 and 18 respectively.

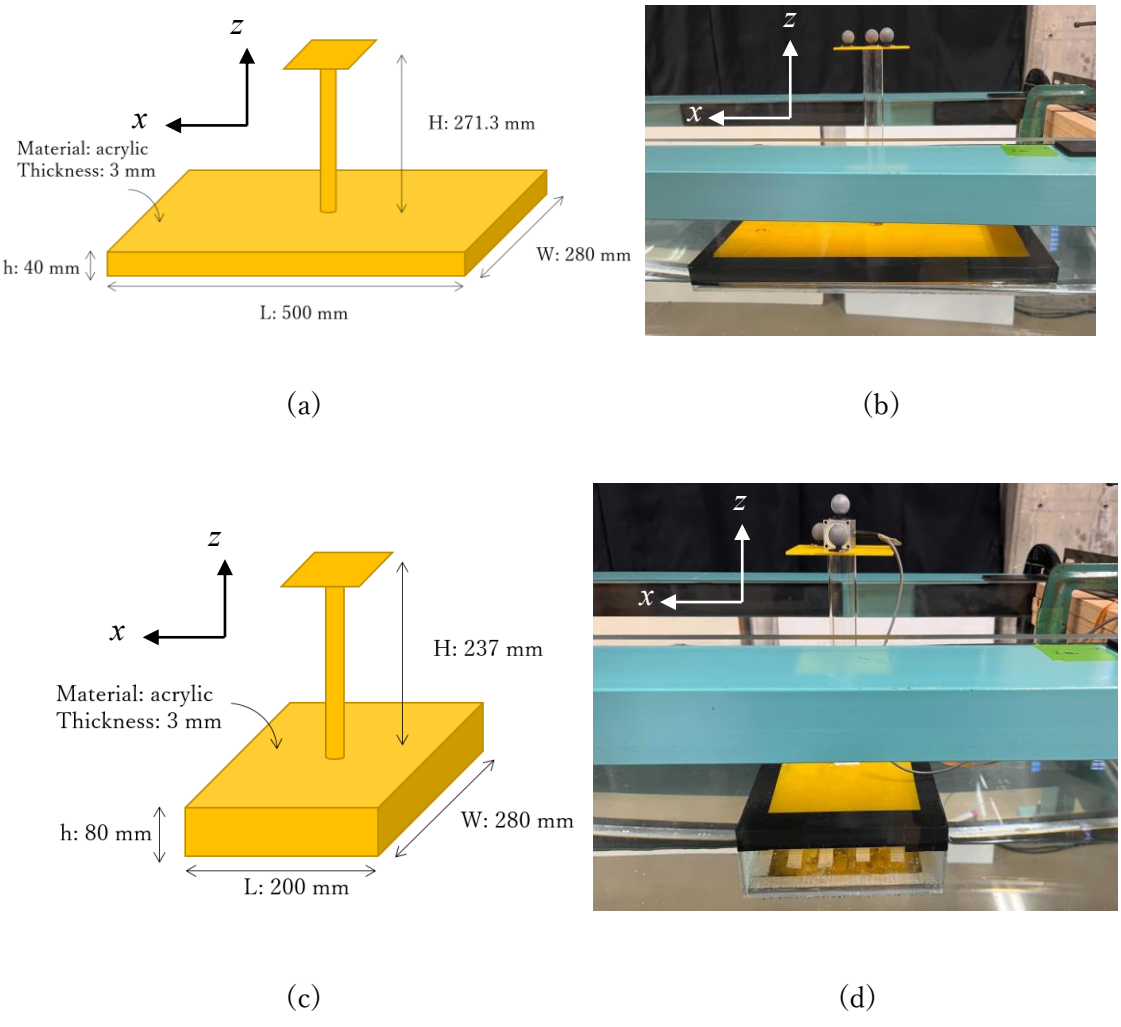

Figure 5. 1 Model visualizations (a) Design visualization of the resonance free model (b) A resonance free model on the 2D tank (c) Design visualization of the model with resonance (d) A model with resonance on the 2D tank

A schematic diagram of the tank setup is provided in Figure 5.2, which also depicts the measurement system. This set-up applies for both phase 1 and 2 of the experiment, especially in the context of wave gages placement. The specifics of the measurement system will be explained in the subsequent section. The experiment involves gathering data for both regular waves and irregular waves. The regular wave data is utilized to be compared with the numerically calculated transfer functions (TFs). The method used to calculate the simulation TFs can be found in Sec. 5.4. Meanwhile, the irregular wave data is used for the Kalman filter and future wave prediction.

For the case of phase 1, fifteen different periods of regular waves are considered, ranging from 0.6 to 1.3 s (corresponding to 4.83 to 10.47 rad/s), with an increment of 0.05 s between each wave period. Meanwhile, even though phase 2 considers the same wave period range (0.6 to 1.3 s) for its regular wave test, a total of 77 regular wave tests are conducted to help finding the definite peak of the resonance. Moreover, various cases of irregular waves assuming the JONSWAP spectrum are also examined. For more detailed information regarding the wave conditions, refer to Sec. 5.3.

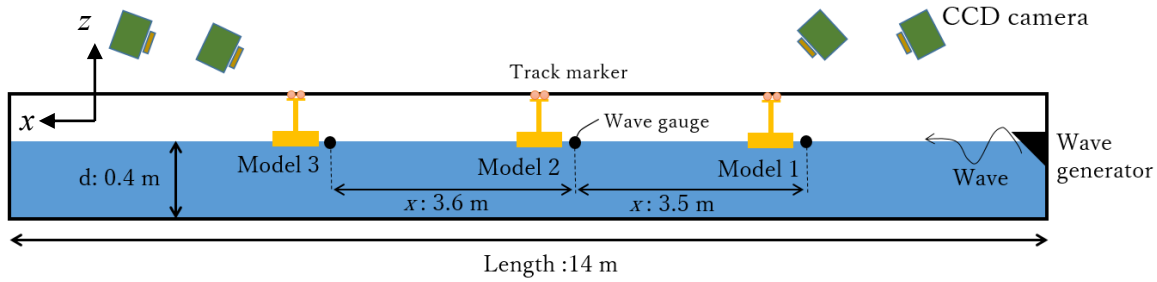

(a)

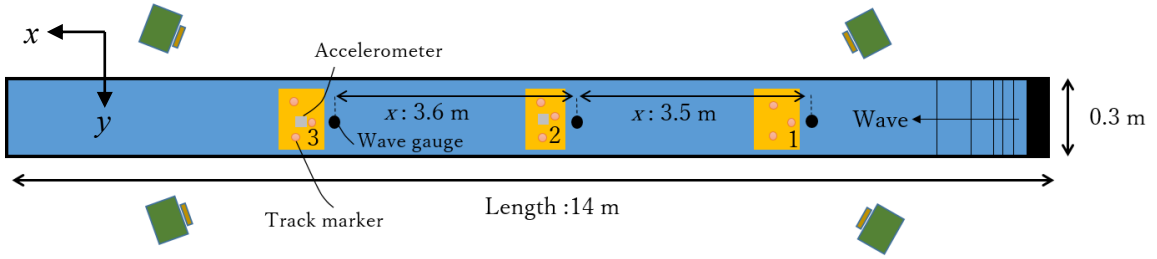

(b)

Figure 5. 2 Experiment set-up (a) Side-view (b) Top-view

5.2 Measurement system

This section describes the measurement system and sensors arrangement used during the test in the 2D tank. Firstly, it is needed to declare that the measurement system described in this section is applied in the same manner during phase 1 and 2 of the experiment unless mentioned otherwise. The purpose of the tank test is to retrieve the TFs and compare them with the simulated transfer functions (TFs), validate the Kalman filter algorithm, and prove the feasibility of future predictions using the spatial distance between two objects. In order to achieve these, it is crucial to accurately capture the responses of the structures and the time histories of the waves. The wave time histories are measured using wave gauges, with a total of three wave gauges being utilized. These wave gauges are positioned in front of each model, indicated by black circles in Figure 5.2. For the case of phase 1, the wave gauges corresponding to Model 1, Model 2, and Model 3 are respectively placed at distances of 0.15 m, 0.13 m, and 0.1 m in front of the model. For phase 2, the wave gauges are located 0.3 m, 0.27 m, and 0.47 m in front of Model 1, Model 2, and Model 3, respectively. Throughout the experiment, efforts are made to maintain these distances constant.

Regarding the mooring system, only Model 1 is moored using a soft rubber band, while Model 2 and Model 3 are left unmoored due to minimal drifting. The rubber band is selected for its low stiffness, minimizing interference with the rigid body movement. One end of the rubber band is attached to the base of the tower, while the other end is connected to a lever holding the wave gauge situated in the negative-x direction of the model.

The measured responses of the structure include the displacement and accelerations of the rigid body. An optical motion tracking system called OptiTrack is used as the primary measurement system to capture the rigid body displacement, particularly focusing on heave and pitch. Four high-speed cameras are employed to assist the OptiTrack system. These cameras track the movement of track markers placed on the top of the tower to ensure visibility. Each model is equipped with three markers. Initially, the goal is to capture the displacement of all models. For this purpose, the four cameras are set up as depicted in Figure 5.2 (represented by green boxes). A real depiction of this high-speed camera can be found in Figure 5.3. However, after analyzing the data obtained in a preliminary test, it was discovered that the high-speed cameras were not reliably detecting the rigid body movement due to the narrow space compared to its length. Therefore, the camera setup is modified to the configuration shown in Figure 5.4 to ensure data quality for the remainder of the experiment. The revised setup focuses on capturing the rigid body motion of Model 1 and Model 2.

In addition to the optical tracking for motion measurement, Model 2 and Model 3 are each equipped with a single-axis accelerometer to capture their vertical acceleration. The

accelerometer data serves as a backup since it is known to be quite noisy, whereas the optical tracking measurement signal is more reliable in this aspect. The signals from both sensors are synchronized in the time domain, and a sampling rate of 100 Hz is used for all the sensors involved. To eliminate high-frequency noise from the measurement data, a Butterworth filter is applied. The filter order is set to five, and its cut-off frequency is determined to be 5 Hz. This filtering process helps to refine the data by removing unwanted noise.

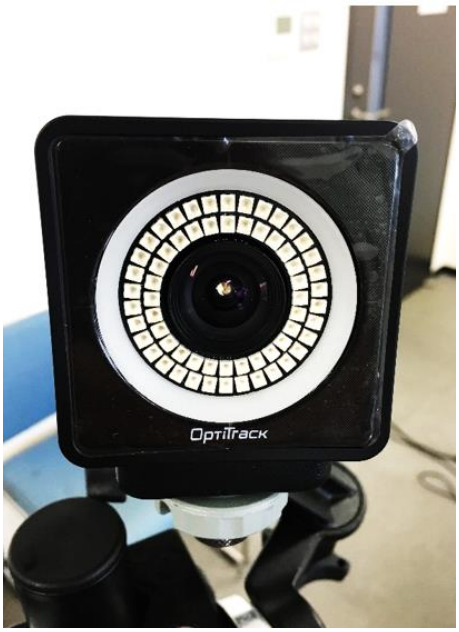

Figure 5. 3 A high-speed camera in the optical tracking system

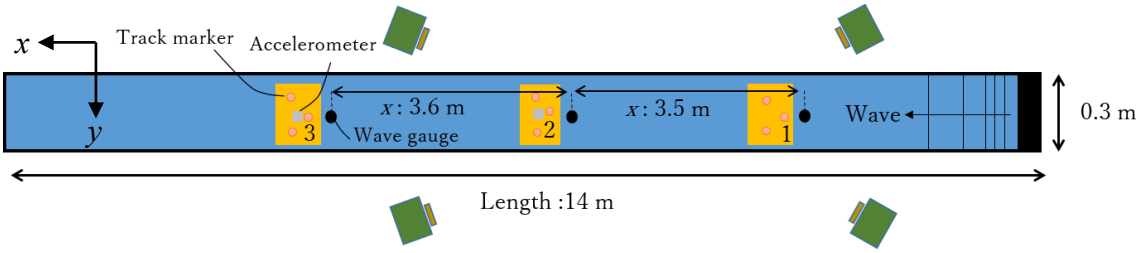

Figure 5. 4 Altered cameras set-up illustrated (top-view)

5.3 Test matrix

The wave test is conducted to examine both regular and irregular waves. Data from the regular wave test is utilized to validate the transfer functions (TFs) obtained from simulations. These TFs are particularly important for wave prediction at Model 1, where the wave is predicted using the Kalman filter algorithm. The wave time series generated by the Kalman filter

algorithm are then used to predict future waves on Model 2 and Model 3, taking into account their spatial distances relative to Model 1. More details regarding the regular wave cases for resonance free model can be found in Table 5.1. Meanwhile, regular wave cases for model with resonance is given in Appendix due to the longer list and to avoid redundancy as the frequency range is the same as phase 1 anyway.

Table 5. 1 Regular wave cases of resonance free model

Case no.	Wave circular frequency (rad/s)	Wave period (s)	Measured wave amplitude at Model 1 (mm)
1	4.83	1.30	4.79
2	5.03	1.25	4.45
3	5.24	1.20	4.93
4	5.46	1.15	5.09
5	5.71	1.10	5.57
6	5.98	1.05	5.18
7	6.28	1.00	4.61
8	6.61	0.95	5.26
9	6.98	0.90	4.22
10	7.39	0.85	4.00
11	7.85	0.80	3.09
12	8.38	0.75	4.98
13	8.98	0.70	5.57
14	9.67	0.65	6.23
15	10.47	0.60	8.02

In addition to regular waves, data retrieval for irregular waves is also performed to serve as input and reference for the wave predictions. Table 5.2 provides specific information about the environmental conditions and the cases considered. Here, the same index number in "case name" column indicates the same wave conditions. Six JONSWAP spectra (long-crested waves) with varying significant heights *(Hs)* and periods *(Ts)* are adopted. The spectrum ranges from 3.77 to 17.58 rad/s. In this table, the index number corresponds to a specific combination of *Hs* and *Ts* for the wave, while the model condition indicates whether the experiment and subsequent prediction involve the presence of a model or not. Two types of model conditions are utilized: no model (NM) and with model condition, in which it is further divided into RF (resonance free) and WR (with resonance) cases. For RF cases, the data being

analyzed and discussed are coming from the experiment that uses resonance free models. Meanwhile, WR cases discuss prediction based on data obtained on the 2D experiment that utilizes models with resonance.

The no model condition is considered to represent the purest form of linearity between input (wave) and output (typically responses) for the Kalman filter algorithm. According to Equation (2.14), the relationship between input and output signals can be described using the response amplitude operator (RAO, G) and phase (φ) functions. Under ideal conditions, where the input and output signals are identical, the RAO and phase functions are typically represented as 1 and 0, respectively, across all elementary wave components. The NM conditions are justified based on this premise.

Table 5. 2 Irregular wave cases, its index description, and cases name

Wave spectrum	Significant height (mm)	Significant period (s)	Index number	Model condition	Case name
JONSWAP	30	0.95	1	NM*	NM_1
				RF*	RF_1
		0.87	2	NM	NM_2
				RF	RF_2
	15	0.95	3	NM	NM_3
				RF	RF_3
				WR*	WR_3
		0.87	4	NM	NM_4
				RF	RF_4
				WR	WR_4
	20	0.95	5	WR	WR_5
		0.87	6		WR_6

*NM: no model, RF: resonance free, WR: with resonance

5.4 Boundary Element Method (BEM) solver

Before discussing the main results from experiment, a simulation intended to validate and compare with the data obtained from experiment is needed to be carried out. For this purpose, simulation code developed based on the boundary integral equations is adopted. Boundary integral equations are a traditional approach used to analyze boundary value problems associated with partial differential equations. The term "boundary element method", or BEM

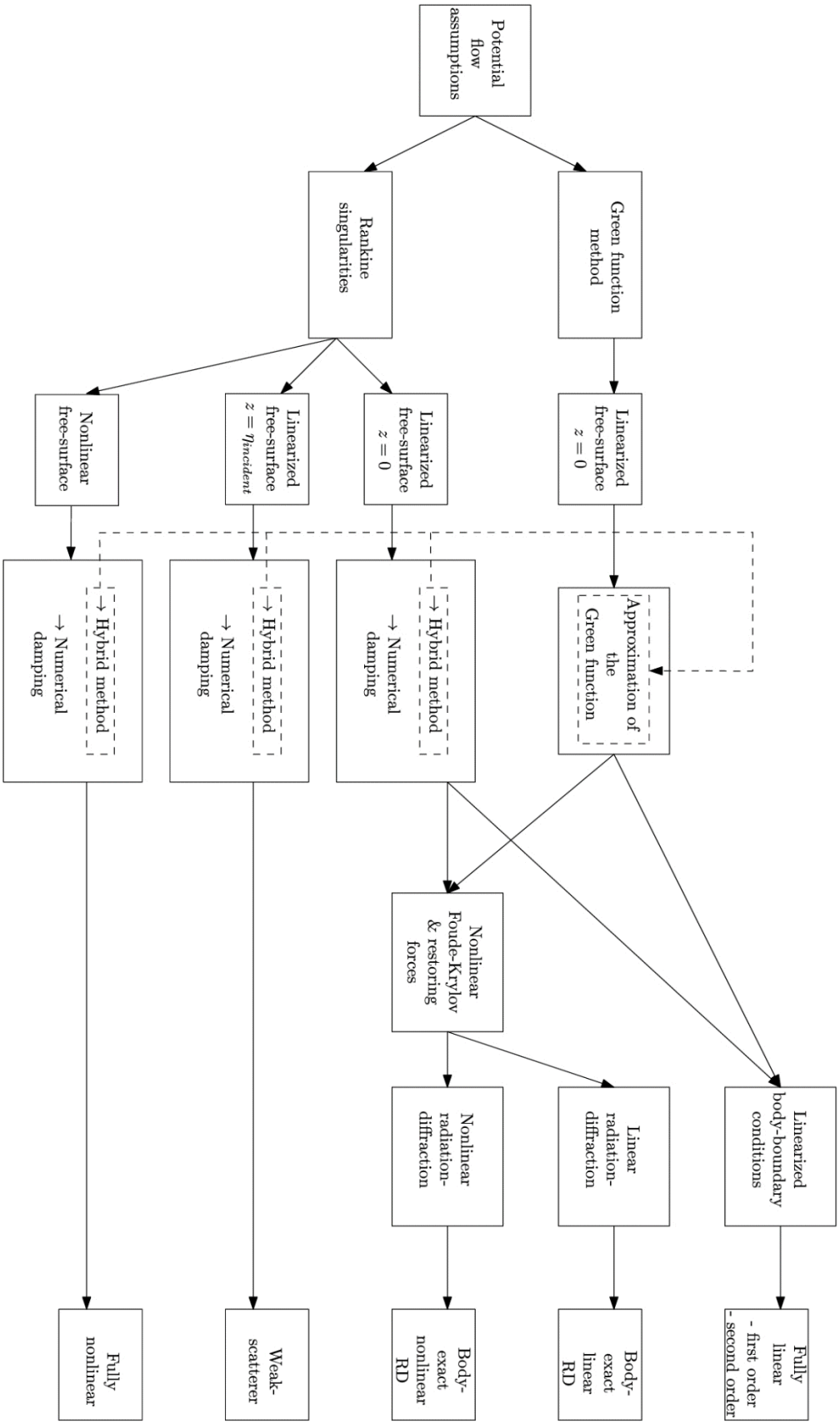

Figure 5. 5 Potential models in boundary element method (Papillon, Castello, & Ringwood, 2020)

encompasses any technique used to numerically approximate the solutions to these boundary integral equations. The distinctive characteristic of the BEM's approximate solution to the boundary value problem is that it precisely satisfies the differential equation within the domain and is represented by a finite set of parameters located on the boundary.

In the field of potential flow theory for water wave–body interaction problems, different numerical models have emerged over the last 50 years or so, thanks to advances in numerical computation (Papillon, Castello, & Ringwood, 2020). The biggest issues in solving potential flow problems lie in the computation of the nonlinear free-surface boundary condition equations, and in the treatment of the body boundary condition (in the case of freely moving bodies) which takes into account the relative motion between the moving body and the unsteady free-surface elevation. Different levels of assumption are made in the treatment of those conditions, which lead to more or less complex models. Figure 5.5 summarizes the "mathematical assumption routes" that may be taken when boundary element method is adopted to solve the partial differential equations in potential flow theory. Technically speaking, both the free-surface Green function and Rankine singularity serve as Green functions. However, for the sake of convenience, the "free-surface Green function" will be simply referred as the "Green function" in this study.

When tackling potential flow problems involving a body, two separate tasks must be addressed: solving the equation governing the motion of the body and solving the equation governing the fluid (potential flow problem). These two aspects are interconnected through the hydrodynamic forces exerted on the body. The approach taken to solve the problem can vary depending on whether a Green function method or Rankine sources are employed. Under the assumption of small wave steepness and small body, the hydrodynamic forces acting on a body can be found using the Green function formulation, which will be adopted in this study. This formulation enables the analysis performed in either the time-domain or frequency domain analysis. For the purpose of validating the TFs retrieved from the experiment, the frequency domain analysis is considered. The coordinate system and notations related to this section is shown in the Figure 5.6.

Let ψ and ψ be the total potential and total complex velocity potential for wave with angular frequency of ω. Based on the Green function theorem, the total potential is given in Equation (5.1), where the total velocity potential can be expressed as Equation (5.2). Here, ψ_0, ψ_D and ψ_R are the complex incident, diffraction, and radiation velocity potential, respectively. Further, the complex incident velocity potential can be described as Equation (5.3), where a_w is the wave amplitude, g is gravitational constant, d is water depth, and is the k wave number. Meanwhile, the complex generalized hydrodynamic forces can be found by integrating the

pressure acting on the wetted surface (S_w). This may be expressed as Equation (5.4), where n is the generalized unit normal vector.

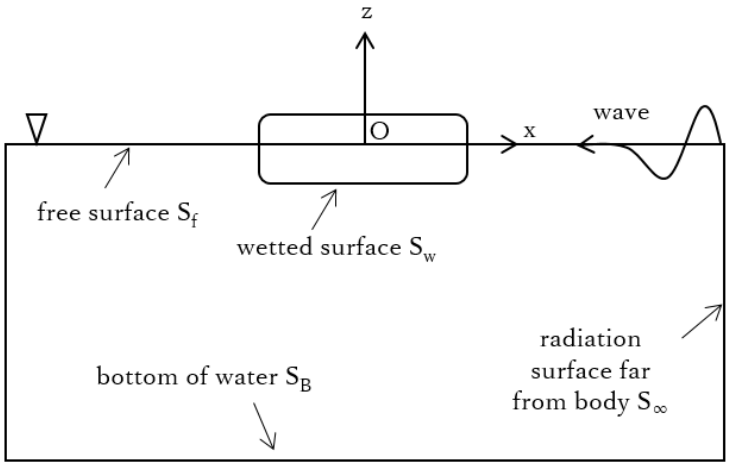

Figure 5. 6 Coordinate system and notations

$$\psi = \mathrm{Re}\,(\psi e^{-i\omega t}) \quad (5.1)$$

$$\psi = \psi_0 + \psi_D + \psi_R \quad (5.2)$$

$$\psi_0 = -\frac{a_w g}{\omega}\frac{\cosh k_0(z+d)}{\cosh k_0 d} e^{ik_0 x} \quad (5.3)$$

$$Fh_i = \iint_{S_w} \mathrm{Re}\left(i\rho\omega\psi_i e^{-i\omega t}\right) n_{0_i}\, ds = \mathrm{Re}\left(\boldsymbol{Fh}_i e^{-i\omega t}\right) \quad (5.4)$$

where,

$$\boldsymbol{Fh}_i = i\rho\omega \iint_{S_w} (\psi_0 + \psi_D) n_i\, ds + \sum_{j=1}^{3} i\rho\omega V_j \iint_{S_w} \psi_{R_j} n_i\, ds \quad (5.5)$$

The first and second terms on left-hand side of Equation (5.5) may respectively be further referred as excitation forces ($\boldsymbol{F}_i^{ex}$) and radiation forces ($\boldsymbol{F}_i^{R}$) as seen in the Equation (5.6). The difference between $\boldsymbol{F}_i^{ex}$ and $\boldsymbol{F}_i^{R}$ lies in the situation of the body itself, with $\boldsymbol{F}_i^{ex}$ are the forces exerted on the stationary body, while $\boldsymbol{F}_i^{R}$ are the present forces when the body is in motion, without the existence of the incident wave.

$$\boldsymbol{Fh}_i = \boldsymbol{F}_i^{ex} + \boldsymbol{F}_i^{R} \quad (5.6)$$

For the case of $\boldsymbol{F}_i^{ex}$, it can be further decomposed into forces caused by the pressure of the incident wave (further referred as Froude-Krylov forces, or $\boldsymbol{F}_i^{FK}$) and diffraction forces ($\boldsymbol{F}_i^{D}$). This can be expressed mathematically as Equation (5.7). Another mathematical definition of the excitation forces can also be found in Equation (5.8).

$$\boldsymbol{F}_i^{ex} = \boldsymbol{F}_i^{FK} + \boldsymbol{F}_i^{D} = i\rho\omega \iint_{S_w} \psi_0 n_i \, ds + i\rho\omega \iint_{S_w} \psi_D n_i \, ds \quad (5.7)$$

$$F_{ex_i}(t) = \mathrm{Im}\left(\left(\boldsymbol{F}_i^{FK} + \boldsymbol{F}_i^{D}\right)e^{-i\omega t}\right) \quad (5.8)$$

Meanwhile, the radiation forces can be described as shown in the Equation (5.9). Here, $\boldsymbol{f}_{ij}$ represents the force applied in the i direction as a result of a unit velocity motion in the jth degree of freedom and V is the velocity of the moving body. Then the total radiation load can be described as shown in the Equation (5.10) and (5.11).

$$\boldsymbol{F}_i^{R} = \sum_{j=1}^{3} i\rho\omega \mathrm{V}_j \iint_{S_w} \psi_{R_j} n_i \, ds = \sum_{j=1}^{3} \boldsymbol{f}_{ij} \mathrm{V}_j \quad (5.9)$$

$$F_{R_i}(t) = \mathrm{Re}\left(\boldsymbol{f}_{ij}\mathrm{V}_j e^{-i\omega t}\right) = \mathrm{Re}\left[\left(\mathrm{Re}\,\boldsymbol{f}_{ij} + \mathrm{Im}\,\boldsymbol{f}_{ij}\right)\mathrm{V}_j e^{-i\omega t}\right] \quad (5.10)$$

or,

$$F_{R_i}(t) = -\left(\rho \iint_{S_w} \mathrm{Re}\left(\psi_{R_j}\right) n_i \, ds\right)\ddot{X}_j - \left(\rho \iint_{S_w} \mathrm{Im}\left(\psi_{R_j}\right) n_i \, ds\right)\dot{X}_j \quad (5.11)$$

where $\dot{X}_J = \mathrm{V}$ and $\ddot{X}_j = -i\omega\mathrm{V}$

As seen in the Equation (5.11), the radiation forces consist of two components: one that is proportional to the acceleration of the body and another that is proportional to the velocity of the body. Based on this understanding, the added mass and damping term arisen from radiation forces can be defined and shown respectively in the Equation (5.12) and (5.13). These terms are adopted to the equation of motion, and after incorporating the excitation forces, the equation of motion to be solved is shown in the Equation (5.14) and (5.15).

$$A_{R_{ij}} = \rho \iint_{S_w} \mathrm{Re}\left(\psi_{R_j}\right) n_i \, ds = \frac{1}{\omega}\mathrm{Im}\left(\boldsymbol{f}_{ij}\right) \quad (5.12)$$

$$B_{R_{ij}} = \rho \iint_{S_w} \mathrm{Im}\left(\psi_{R_j}\right) n_i \, ds = -\,\mathrm{Re}\left(\boldsymbol{f}_{ij}\right) \quad (5.13)$$

$$\left(\boldsymbol{M}_{ji} + A_{R_{ji}}\right)\ddot{X}_i(t) + B_{R_{ji}}\dot{X}_i(t) + K_{H_{ji}}X_i(t) = \boldsymbol{F}_j^{ex}e^{-i\omega t} \quad (5.14)$$

substituting $X(t) = Re(\boldsymbol{X}e^{-i\omega t})$,

$$\left[-\omega^2\left(\boldsymbol{M}_{ji} + A_{R_{ji}}\right) - i\omega B_{R_{ji}} + K_{H_{ji}}\right]\boldsymbol{X}_i = \boldsymbol{F}_j^{ex} \quad (5.15)$$

5.5 Transfer functions comparison

The simulated transfer functions (TFs) obtained based on the description mentioned above are compared with the experimental TFs, focusing on heave and pitch responses in terms of both amplitude (RAO) and phase. The experimental RAO and phase functions are obtained

from the regular wave experiments by applying Fast Fourier Transform (FFT) to the data. The phase TFs play a crucial role in the Kalman filtering process, as this study focuses on time domain data. The phase TFs can be effectively obtained by calculating the phase difference between the wave and the response. The RAOs are always normalized by dividing the response amplitude by the wave amplitude measured at Model 1. Ideally, the undisturbed wave data should be used to capture the hydrodynamic effects between the models. However, due to data limitations, the wave measured at Model 1 is utilized instead. This is applicable for data involving resonance free model and model with resonance. Figure 5.7 displays the TFs for the pitch and heave response belong to resonance free model, while Figure 5.9 shows the TFs for pitch and heave of model with resonance.

Firstly, TFs from resonance free model is discussed. The BEM simulations are carried out two-dimensionally using in-house code assuming three degrees of freedom (surge, heave, and pitch). In Figure 5.7, the dark grey lines represent the simulation results, the black dots represent the experimental results for Model 1, and the grey dots represent the experimental results for Model 2. When directly examining the retrieved time domain data, it can be observed that the wave amplitude for long waves at Model 1 remains consistent with a sinusoidal shape, whereas shorter waves exhibit the opposite trend. This indicates that nonlinearity effects are less prominent in longer waves compared to shorter waves, resulting in more noticeable differences in RAO between Model 1 and Model 2 in the higher frequency domain.

The comparison between the retrieved TFs from the experiment and simulation also reveals differences in terms of their curve regularity as seen in Figure 5.7(a) and (c). The plot generated from simulation appears smoother, while the experimental-based plot exhibits more waviness, particularly in the lower frequency range. This irregularity in the experimental data can be attributed to hydrodynamic interactions among the three floats and reflections from the end wall, which may have affected the consistency of the data. When extracting the TFs from the experimental data, it was ensured that the sinusoidal data used for calculations were among the first ten perfectly developed sinusoidal waves, aiming to minimize the influence of reflection waves. However, for lower frequency waves, which correspond to longer periods, the wave reaches the end of the tank more quickly, resulting in faster arrival of reflection waves. Furthermore, wave interactions between floating bodies are expected to be more significant in the lower frequency range due to the relatively closer distance between the models when the wavelength is longer. Despite these encountered problems, the simulation and experimental TFs generally exhibit acceptable values in comparison to each other. To enable filtering for RF cases, the retrieved TFs from the experiment are combined with the simulated TFs to achieve a wider spectrum range. The spectrum assumed for the irregular wave test covers a range from 3 to 16 rad/s.

Next, discussion on the TFs of model with resonance is given. Unlike the resonance free model, the simulations for model with resonance are carried out three-dimensionally using a BEM solver tool called Nemoh. The mesh of this model can be found in Figure 5.8. The results of simulated TFs and experiment TFs are given in Figure 5.9. Similarly, pitch and heave TFs are compared in this figure. Results from simulation are indicated with grey lines, while results based on experiment are indicated by black dots. Looking at the presented results, it is pretty clear that the experiment vs simulation results are not as congruent as TFs results comparison of resonance free model.

Firstly, the RAO results are discussed. For pitch, the results can be seen in Figure 5.9(a). Initial simulation results (grey lines) indicate a poor match with the experiment data (black dots). A better fit is found after center of gravity to metacenter distance (GM) and damping coefficient in the simulation is tuned. The result from simulation after tuning is indicated by grey dots in Figure 5.9(a). However, these tunings need to be proven practically, especially when it comes to GM since the value of GM is initially found mathematically at 6.7 cm and recheck has been done to ensure the value is correct. To further ensure the value of GM, a subsequent experiment was conducted. In this experiment, heeling angles were measured using optitrack by adding a small weight of m gr at a distance of x centimeters from the center of the structure. The experiment allowed for the calculation of GM using Equation (5.16), where M_0 represents the mass of the structure and ϵ denotes the heeling angle. Four different weights (100, 200, 250, and 300 gr) were employed, while x remained constant at 8.8 cm. Interestingly, the experimentally obtained GM was found to be 7 mm shorter than the analytical values. Figure 5.9(a) illustrates the pitch RAO functions assuming the experimentally obtained GM, represented by disconnected grey lines. From these findings, it can be concluded that the simulated pitch resonance peak approaches closer to the experimental results, but does not precisely match. The observed difference could be attributed to the oversight of the limitations on the heeling angle values during the follow-up experiment conducted to determine GM. Theoretically, Equation (5.16) is applicable only for small angles, and the heeling angle of the scaled model during the experiment should have been limited to a maximum of 2 degrees (池田, 梅田, 慎, & 内藤, 2013). However, the heeling angle from the experiment ranges from 2.4 to 7.4 degrees. It is also advised that instead of keeping the x distance constant, the same weight should be used while the x distance is shifted. Therefore, it is recommended to conduct another experiment to determine the corrected value of GM based on the aforementioned recommendations.

$$GM = \frac{mx}{(M_0+m)\tan\epsilon} \quad (5.16)$$

For the case of heave RAO, it can be concluded that simulation and experiment data generally give a much better match when compared as seen in Figure 5.9(c). The most noticeable

discrepancy is found to be the trend of RAO data within the frequency range of around 6 to 8.5 rad/s. Upon further investigation, it is discovered that coupled motions with roll are substantial in this frequency range, hence affecting the RAO of heave.

Lastly, the phase functions of the model with resonance are examined. Figure 5.9(b) and (d) illustrate the pitch phase functions and heave phase functions, respectively. The heave phase functions demonstrate a stronger agreement between the simulation and experiment compared to the pitch phase functions, similar to the RAO functions. As seen in Figure 5.9(d), the heave experimental phase functions cluster around the same values as the simulated phase functions.

To analyze the pitch phase functions, simulation data based on tuning is utilized due to the closely matched trends observed between the simulation and experiment in the amplitude domain TFs. In Figure 5.9(b), the simulated pitch phase functions based on tuning are represented by grey dots. Comparing them with the experimental phase functions, it is noted that the results align closely in the lower frequency range, up to approximately 8 rad/s. However, this correspondence is expected, as the discrepancy in the RAO between the simulation considering tuning and the experiment increases beyond the frequency of approximately 8 rad/s. Hence, a similar phenomenon is anticipated in the phase functions. To address the discrepancy in the phase functions, it is necessary to achieve better agreement in the amplitude domain functions as well. As mentioned earlier, conducting another careful experiment to determine a corrected value of GM might be the most logical initial step in identifying the cause of the issue. Meanwhile, for the time being, predictions related to the model with resonance (WR cases) are performed solely using data unrelated to pitch. Unlike the free resonance model filtering (RF cases), the simulated TFs will be considered assuming a frequency range from 3 to 16 rad/s.

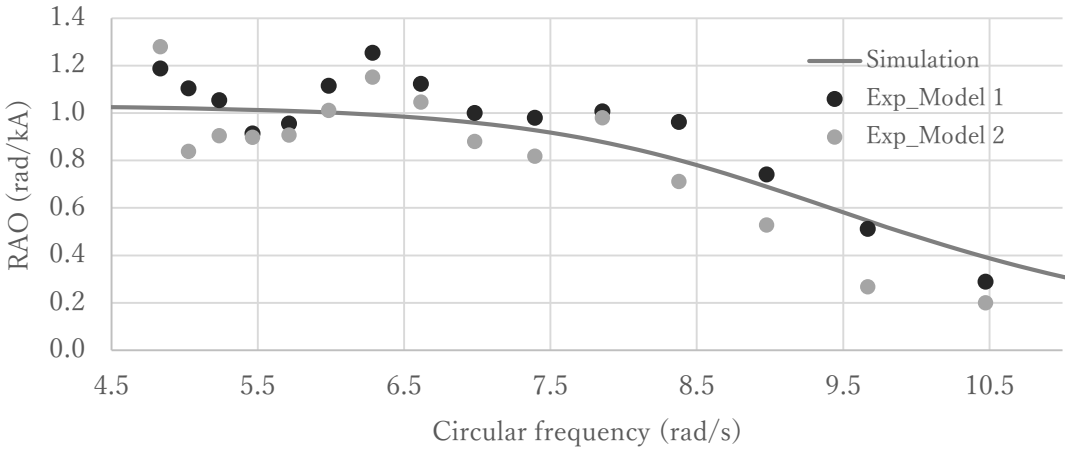

(a)

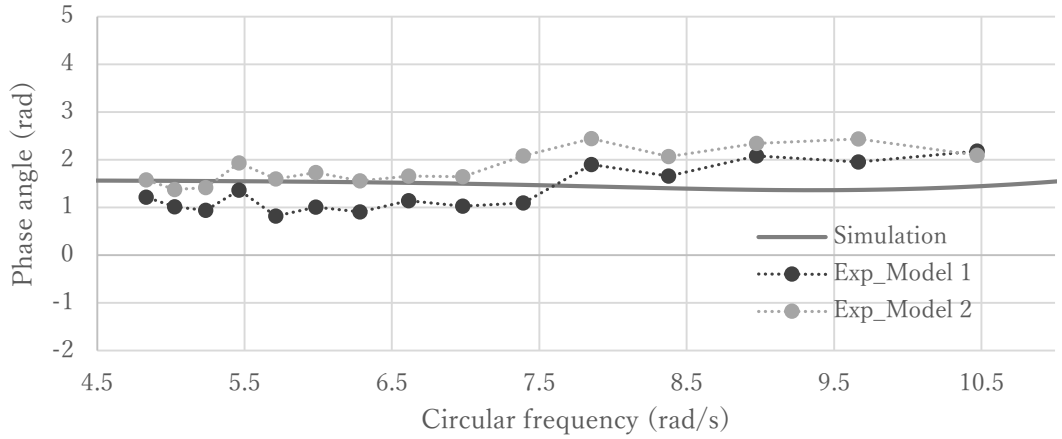

(b)

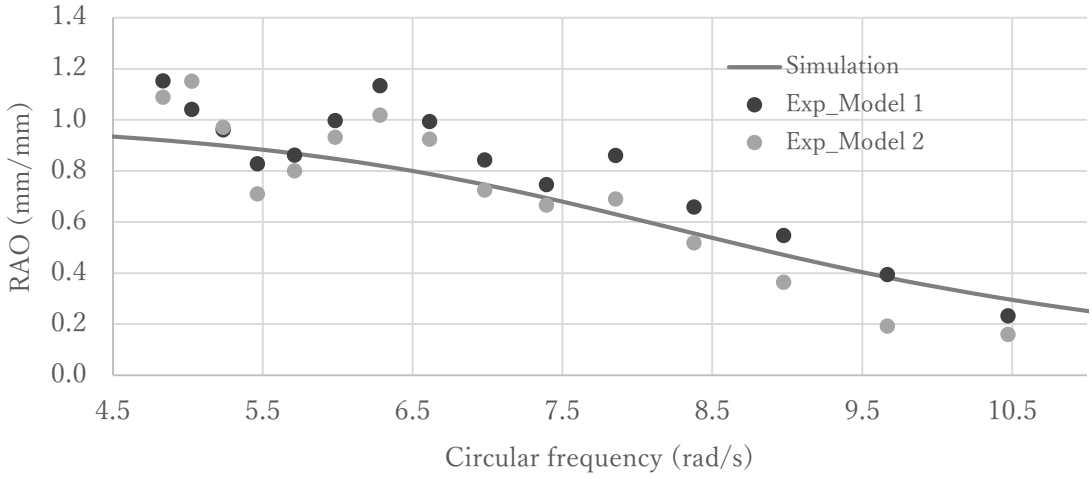

(c)

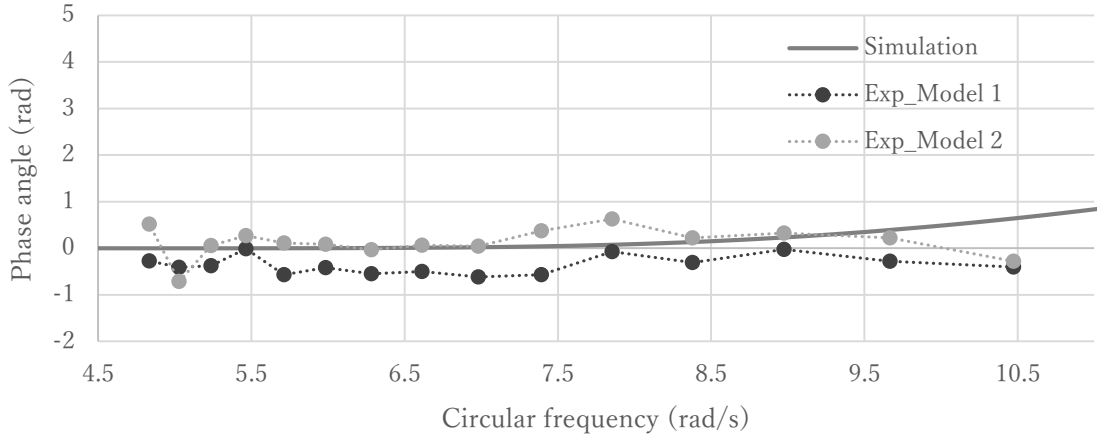

(d)

Figure 5. 7 TFs comparison between experiment and simulation of resonance free model (a) RAO pitch (b) Phase function pitch (c) RAO heave (d) Phase function heave

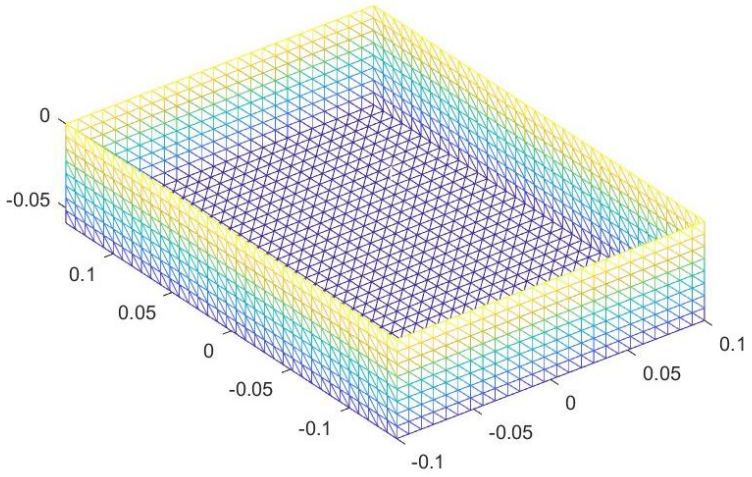

Figure 5. 8 Mesh discretization of model with resonance in Nemoh

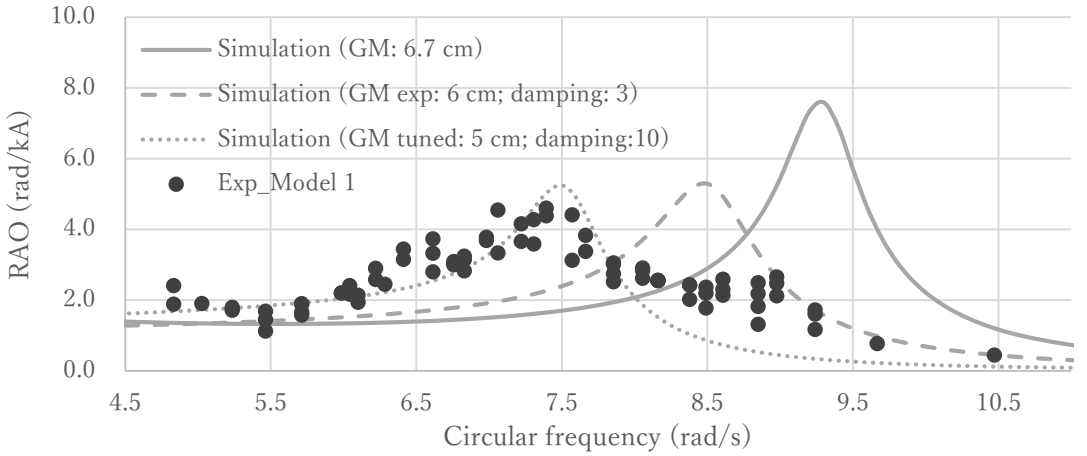

(a)

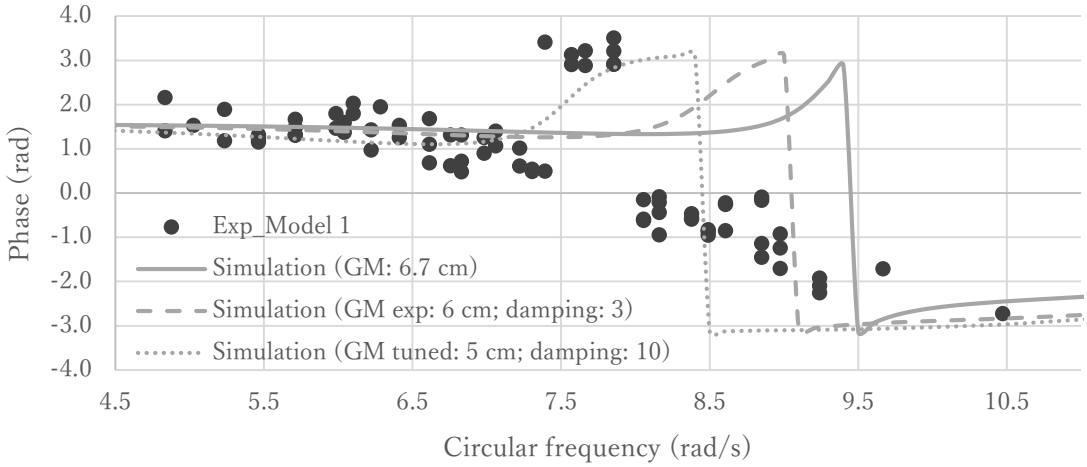

(b)

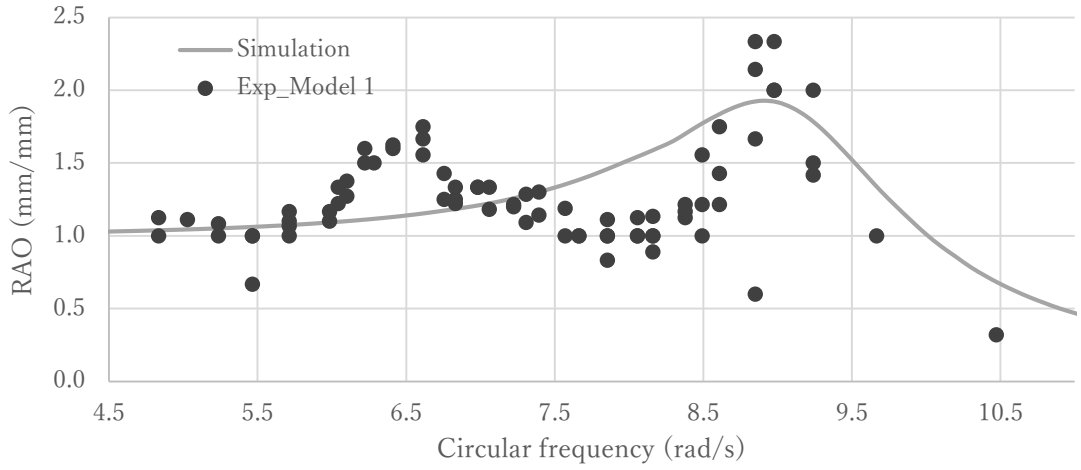

(c)

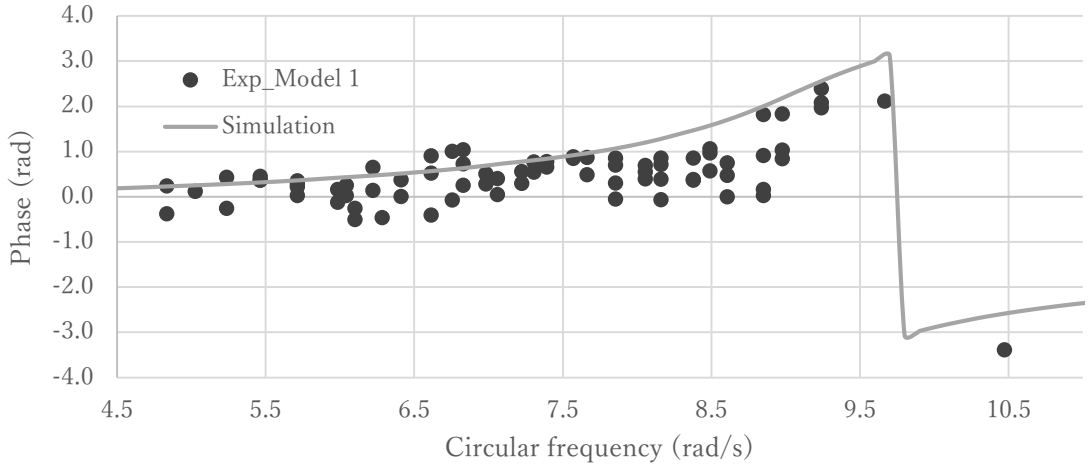

(d)

Figure 5. 9 TFs comparison between experiment and simulation of model with resonance (a) RAO pitch (b) Phase function pitch (c) RAO heave (d) Phase function heave

5.6 Wave profile identification

This section focuses on the outcomes of identifying the wave profile using the Kalman filter in Model 1. In this case, the wave profile is determined by incorporating the response data (heave in this case) obtained from an experiment as input in the Kalman filter algorithm. The predicted wave profile is then compared to the wave gauge data. Just like results in Chapter 3, in order to simplify the analysis, the accuracy is measured using the correlation coefficient (r_{xy}) from this point forward. The correlation coefficient values range from -1 to 1, with a value of 1 indicating a perfect match between the predicted and measured signals. Equation (3.1) can be used to calculate the correlation coefficient (r_{xy}), with X representing the wave reference data and Y representing the wave prediction data.

The assumed elementary waves for all Kalman filter (KF) predictions are 80. Based on explanation in Sec. 2.3, the state variables then can be determined as 160, with n_ω being 80 and n_β being 1. Table 5.3 provides the correlation coefficients (r_{xy}) for all the assumed cases. The numbers listed alongside the r_{xy} values represent the assumed KF filtering time (referred to as T), which is varied at 25, 40, and 55 s. Generally, a minimum r_{xy}value of approximately 0.8 is considered indicative of "good results". Figure 5.10 provides additional visual context by comparing the predicted and reference waves for three specific cases: NM_3 with $r_{xy\_25} \approx 1.0$, RF_3 with $r_{xy\_25} \approx 0.8$ and WR_3 with $r_{xy\_25} \approx 0.78$. Here, the subscript value of 25 corresponds to the assumed KF filtering time T done in the unit of seconds.

Table 5. 3 Correlation coefficient of KF results at Model 1

Case name	r_{xy_25}	r_{xy_40}	r_{xy_55}
NM_1	0.979	0.950	0.937
NM_2	0.966	0.954	0.962
NM_3	0.975	0.940	0.926
NM_4	0.970	0.955	0.952
RF_1	0.799	0.507	0.432
RF_2	0.801	0.633	0.501
RF_3	0.813	0.718	0.649
RF_4	0.836	0.706	0.636
WR_3	0.782	0.703	0.662
WR_4	0.793	0.660	0.612
WR_5	0.815	0.670	0.633
WR_6	0.804	0.717	0.697

According to the defined "good results standard," it can be observed from Table 5.3 that the NM cases exhibits different tendencies compared to RF and WR cases. NM cases consistently yield high-accuracy results for all assumed filtering times, while the accuracy of RF and WR cases decreases as the filtering time increases. This disparity is natural due to the presence of hydrodynamic effects and reflection waves (especially for RF cases), which impact the high-frequency wave region. The simulation, as discussed in the previous section, only considers linear waves, resulting in greater difficulty for the filter to accurately predict waves in the higher frequency range that occur later.

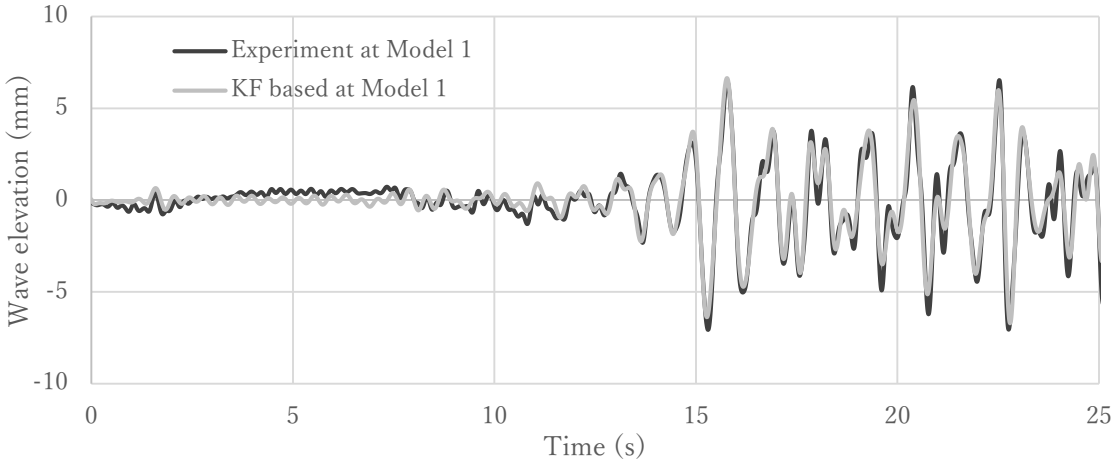

(a)

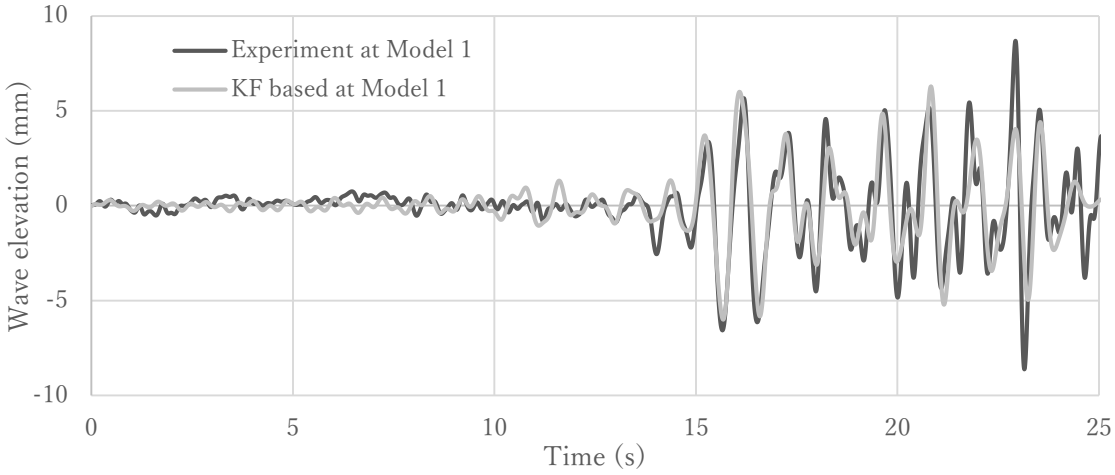

(b)

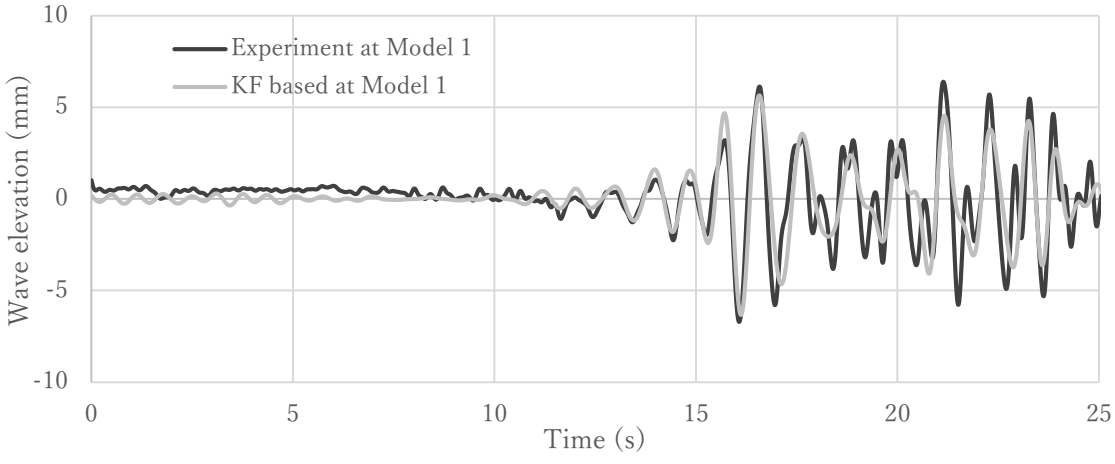

(c)

Figure 5. 10 Experimental vs KF wave time histories at Model 1; KF T: 25 s (a) Case NM_3 (b) Case RF_3 (c) Case WR_3

5.7 Future wave prediction results

This section focuses on discussing future wave predictions carried out in Model 2 and Model 3. With the knowledge of elementary wave coefficients from the Kalman filter in Model 1, the wave profile in Model 2 and Model 3 can be determined using Equation (4.8). The spatial distances (x) for RF cases between Model 2 and Model 1, and between Model 3 and Model 1, are 2.98 m and 6.55 m, respectively. Meanwhile, for WR cases, the spatial distance of Model 2 and Model 1 is 3.47 m, and the distance between Model 3 and Model 1 is 7.27 m. Since the water depth (d) is 0.4 m, it satisfies the condition $x/d \geq 3$ for all cases, fulfilling the causality criteria explained in Chapter 4 and justifying the future wave analysis.

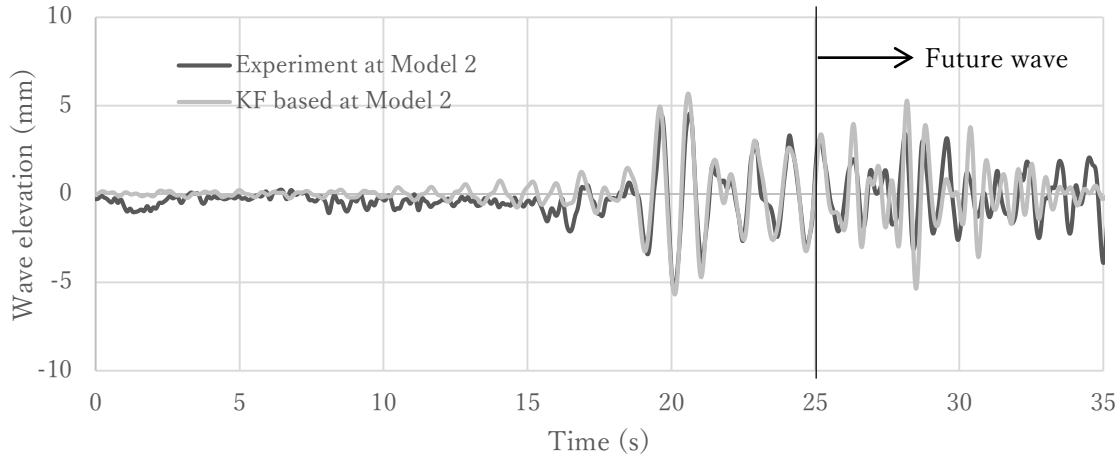

(a)

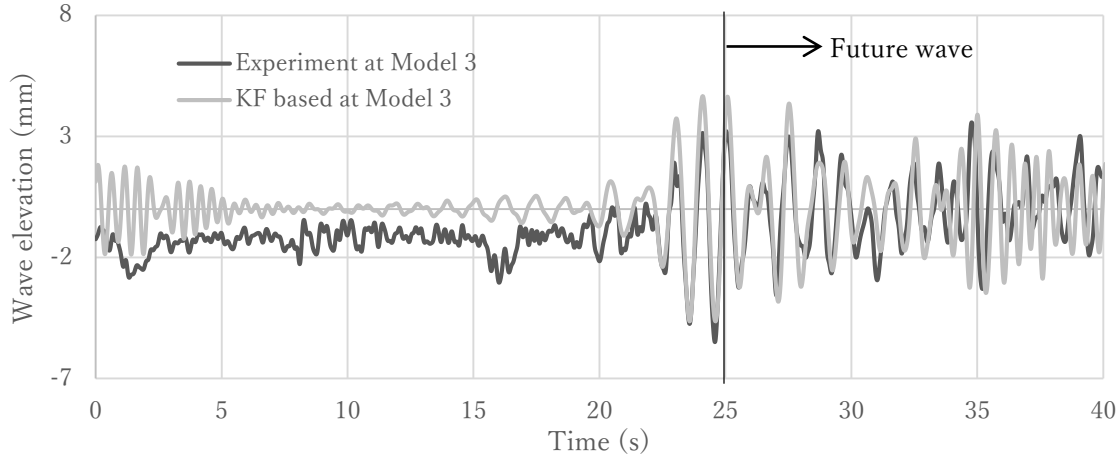

(b)

Figure 5. 11 Experimental vs KF-based wave histories (a) Wave at Model 2; case RF_3; KF T:25 s (b) Wave at Model 3; case RF_3; KF T: 25 s

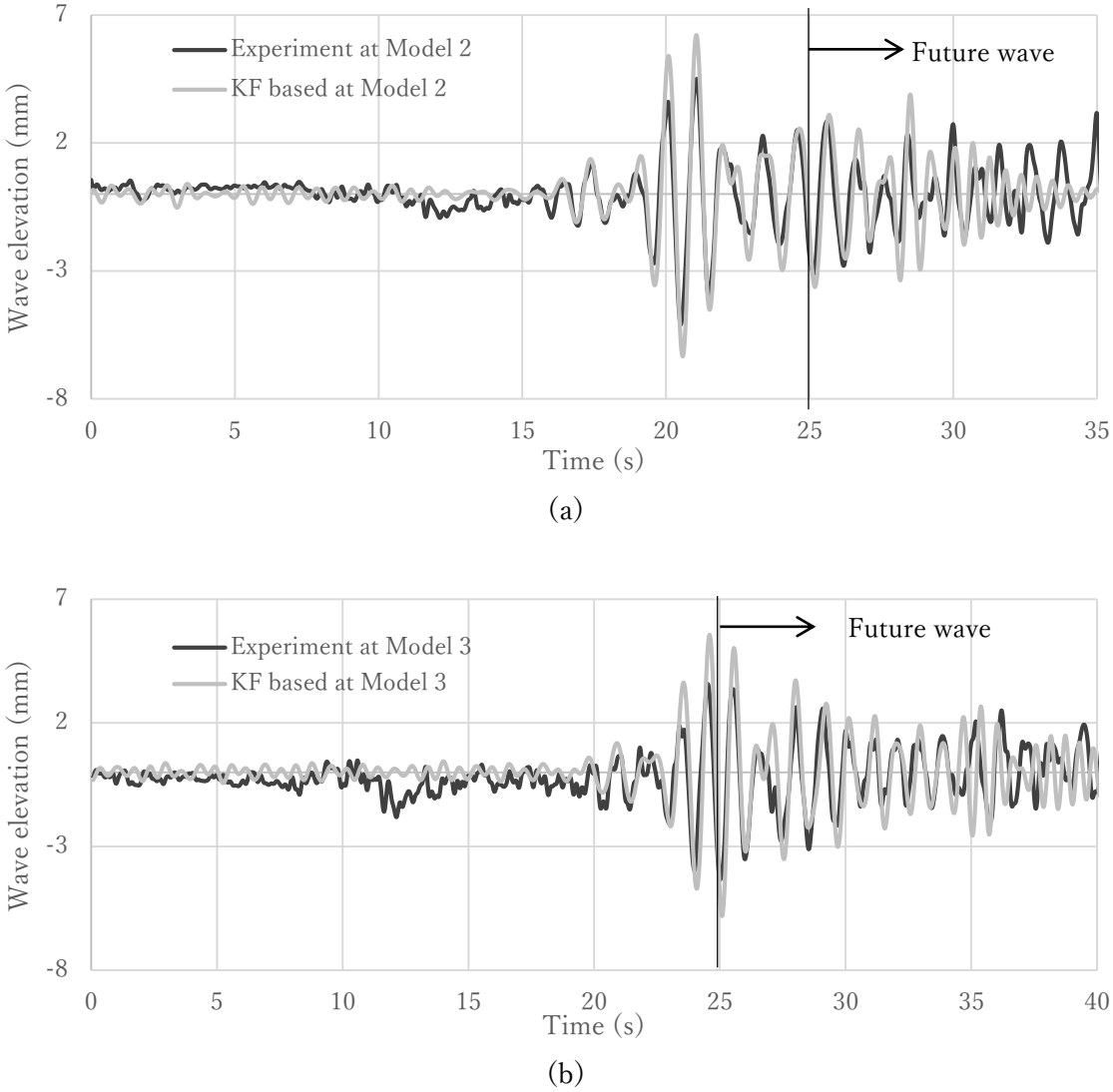

Figure 5. 12 Experimental vs KF-based wave histories (a) Wave at Model 2; case WR_3; KF T:25 s (b) Wave at Model 3; case WR_3; KF T: 25 s

Given that the input wave at the reference point has been decomposed using the Kalman filter algorithm in the previous step, the wave time series at a distance x away from the reference point can be plotted for $0 < t < T + \Delta t$ using Equation (4.7), where Δt represents the future time. Consequently, the wave profiles in Model 2 and Model 3 can be calculated using the elementary wave coefficients for $T = 25$ s in Model 1.

Figure 5.11(a) and (b) illustrate the wave time histories at Model 2 and Model 3, respectively, obtained using the aforementioned method for the RF_3 case with KF $T = 25$ s. The same results for case WR_3 is given in Figure 5.12(a) and (b). From these particular examples, it can be observed that Model 3, which has a greater distance (x) from Model 1, exhibits a longer predictable future time. The correlation coefficients (r_{xy}) consistently hover around 0.8,

especially for RF cases, when the assumed future predictable times at Model 2 and Model 3 are 3 and 8 s, respectively. For WR cases, the future predictable time are found to be longer, that is as long as 5 and 10 s at Model 2 and Model 3, respectively. This is found to be reasonable as it has been stated in the beginning of this section, the distance between Model 2 and Model 1, and Model 3 and Model 1 of WR cases are slightly longer compared to the RF cases. Hence, the aforementioned finding of "a longer spatial distance will result in a longer predictable future time as well, assuming the water depth remains the same" is further proven. Table 5.4 provides complete data on r_{xy} during the future predictable time for Model 2, while Table 5.5 presents the same data for Model 3 for both RF and WR cases.

In the following comparison, future wave predictions at Model 2 are examined using two different methods. Initially, when utilizing the previously mentioned method, the future predictable time at Model 2 is consistently determined to be only 3 s ahead for RF cases. Therefore, a direct comparison is made by assuming Kalman filter (KF) prediction directly at Model 2. In this scenario, the ϕ term in Equation (4.7) can be disregarded, and the output vector of the system in Equation (2.5) represents the response of Model 2, specifically the heave motion. Consistently, it is observed that adopting the spatial distance method is more favorable due to the existence of the spatial distance, resulting in a longer predictable future time. Moreover, this method yields higher accuracy. To provide further context, Figure 5.13 is presented, illustrating three types of data. The dark grey line represents the reference wave obtained from measurements, the grey line represents wave predictions obtained by adopting the spatial distance and calculated using Equation (4.7), and the discontinued black lines represent wave predictions assuming KF is directly applied at Model 2, utilizing Equations (2.4) to (2.10) with the heave response of Model 2 instead of Model 1 for **y** in Equation (2.5). It can be observed that the accuracy deteriorates more rapidly in the future time for the discontinued black lines scenario.

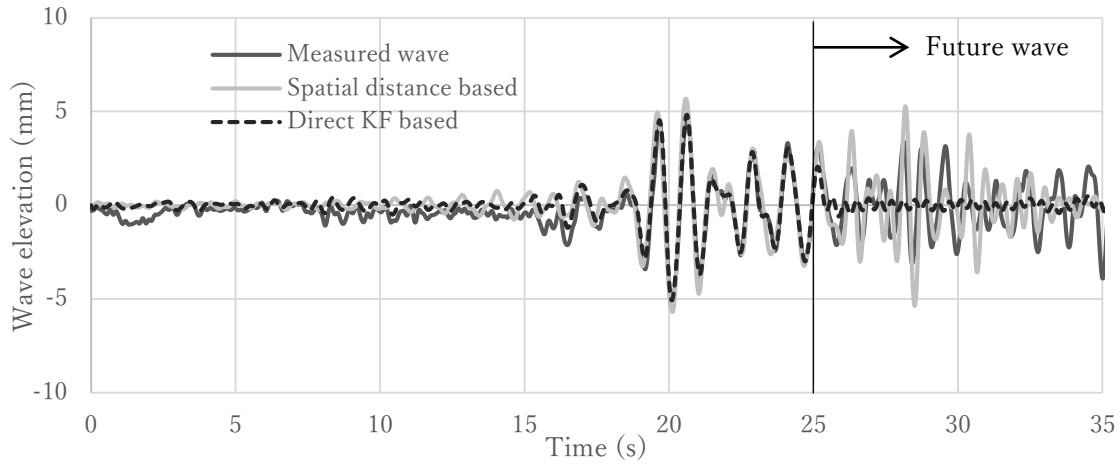

Figure 5. 13 Experimental vs spatial distance based wave prediction vs direct KF wave prediction at Model 2; case RF_3; KF T: 25 s

Table 5. 4 Correlation coefficient of future wave at Model 2 (based on KF T: 25 s)

Case name	r_{xy_25}		
	3 s ahead	8 s ahead	15 s ahead
NM_1	0.932	0.886	0.554
NM_2	0.945	0.820	0.493
NM_3	0.945	0.842	0.477
NM_4	0.893	0.796	0.541
RF_1	0.858	0.584	0.400
RF_2	0.810	0.584	0.408
RF_3	0.762	0.605	0.417
RF_4	0.764	0.585	0.426
Case name	r_{xy_25}		
	5 s ahead	10 s ahead	15 s ahead
WR_3	0.780	0.622	0.442
WR_4	0.751	0.509	0.413
WR_5	0.864	0.571	0.463
WR_6	0.759	0.535	0.441

Table 5. 5 Correlation coefficient of future wave at Model 3 (based on KF T: 25 s)

Case name	r_{xy_25}		
	3 s ahead	8 s ahead	15 s ahead
NM_1	1.000	1.000	0.899
NM_2	0.905	0.966	0.617
NM_3	1.000	0.911	0.772
NM_4	1.000	1.000	0.888
RF_1	0.900	0.858	0.567
RF_2	0.772	0.755	0.626
RF_3	0.936	0.861	0.504
RF_4	0.822	0.815	0.461
Case name	r_{xy_25}		
	5 s ahead	10 s ahead	15 s ahead
WR_3	0.897	0.830	0.676
WR_4	0.823	0.778	0.554
WR_5	0.902	0.797	0.665
WR_6	0.911	0.828	0.626

The future predictable time window can be explained by examining the correlation functions of the signals involved. When considering the future predictable time based on direct Kalman filter (KF) results, the auto-correlation function of the wave at Model 2 is considered. On the other hand, the cross-correlation function between the wave at Model 1 and the wave at Model 2 or Model 3 is used to explain the future predictable time in predictions based on the spatial distance. Equation (5.17) is utilized to calculate the cross-correlation of the signal $f_c(t)$ and the signal $g_c(t)$ over a time lag of τ s. In this case, $f_c(t)$ represents the time series of wave elevation at Model 2 or Model 3, and $g_c(t)$ represents the time series of wave at Model 1 for $t = T$, which is 25 s in this case. The bar symbol indicates the complex conjugates for complex-valued signals.

$$(f_c \star g_c)(\tau) = \int_{-\infty}^{+\infty} \overline{f_c(t)}\, g_c(t+\tau)\, dt \quad \cdots\cdots (5.17)$$

Cross-correlation measures the similarity between two signals as a function of their displacement relative to each other. A value close to zero at a time lag indicates that the two signals are uncorrelated or perfectly random at that particular time lag, suggesting non-predictability between the signals. A value close to one indicates strong correlation between the signals. The same interpretation can be applied to the auto-correlation function, which can be calculated using Equation (5.17) assuming $f_c(t) = g_c(t)$, where $f_c(t)$represents the wave time histories at Model 2 for $t = T$ (25 s in this case).

Figure 5.14 provides further illustration of this explanation. Figures 5.14 (a), (b), and (c) depict the auto-correlation function of the wave at Model 2, the cross-correlation function between the wave at Model 1 and Model 2 (referred to as Ω_2), and the cross-correlation function between the wave at Model 1 and Model 3 (referred to as Ω_3) for RF cases considering KF $T = 25$ s. In the case of auto-correlation, the signals exhibit strong correlation when the time difference is zero, indicating an extremely short future predictable time if the spatial distance is not taken into account. For Ω_2, the densest correlation is found at around 4 s. This means that the signal at Model 1 at $t = 0$ s has the most influence on the signal at Model 2 at $t = 4$ s. Similarly, the signal at Model 1 at $t = -4$ s has the most influence on the signal at Model 2 at $t = 0$ s. Thus, all the information at Model 1 before $t = 25$ s propagates (convoluted) to Model 2 up to $t = 25 + 4$ s or slightly beyond. The same applies to the wave at Model 3, but in this case, the highest correlation is found at $t \approx 25$ s seconds instead of 4 s.

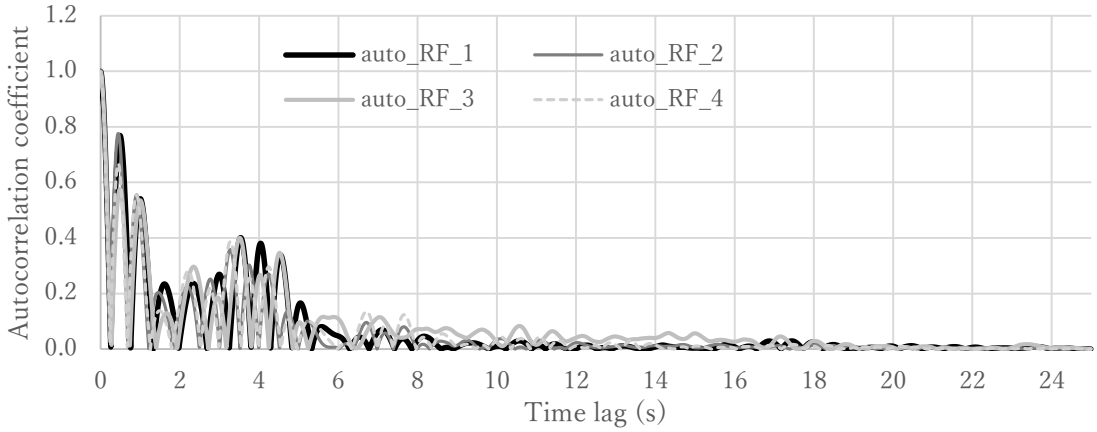

(a)

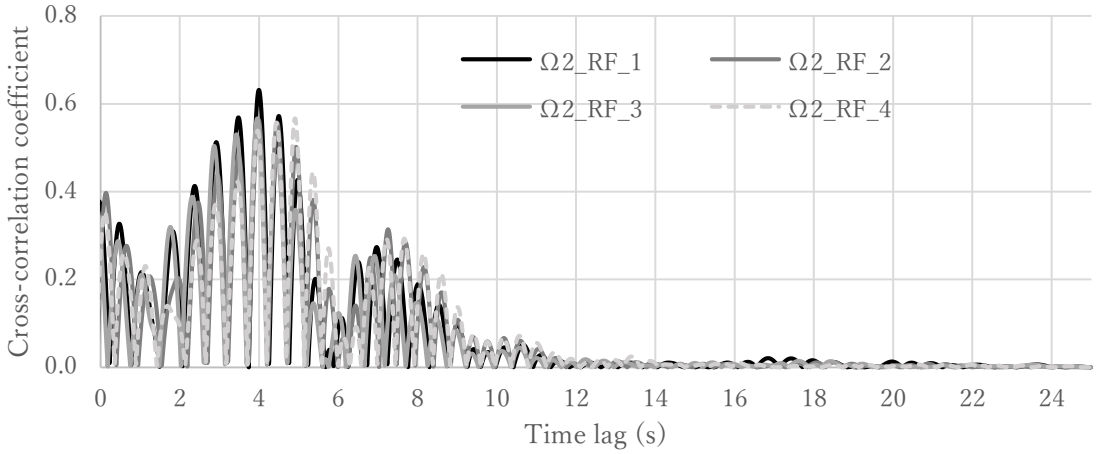

(b)

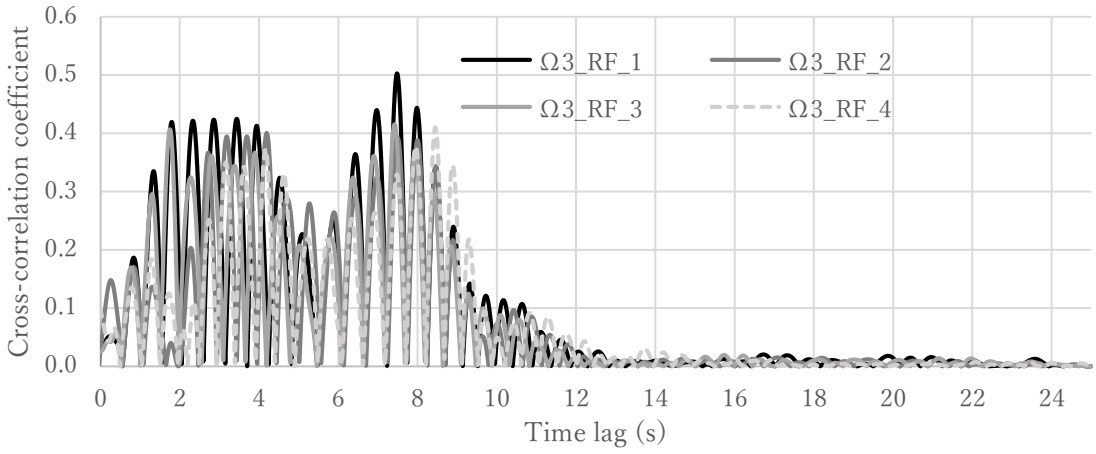

(c)

Figure 5. 14 Correlation functions for RF cases (a) Autocorrelation functions of wave at Model 2 (b) Cross-correlation functions between wave at Model 1 and Model 2 (c) Cross-correlation functions between wave at Model 1 and Model 3

5.8 Future response prediction results

In theory, the responses of structures can be calculated if the input wave and transfer functions (TFs) of the structures are known, as described in Equation (2.13) and Equation (2.14). The wave data obtained and discussed in the previous section are utilized as the input to predict the response of Model 2 and Model 3. Similar to the prediction of wave time series in Sec. 5.7, the predictions of time response histories can be obtained using Equation (4.8). Since satisfactory results are only achieved when $T = 25$ s for RF and WR cases, the response predictions are focused on these cases. The obtained results are then compared to the response data obtained from experiments. Given the availability of reference data, the pitch and heave predictions are performed for Model 2, while the response predicted for Model 3 is its vertical acceleration.

Table 5.6 presents the values r_{xy_25} during the future predictable time for Model 2, and Table 5.7 displays the corresponding values for Model 3. From these tables, it can be observed that the prediction of responses has been successfully carried out, except for the pitch response prediction on Model 2 of WR cases. Figure 5.15 provides a set of examples illustrating the future responses of heave at Model 2 and vertical acceleration at Model 3 for case RF_1; KF T: 25 s, while the same responses for case WR_3 can be found in Figure 5.16(a) and (b). Note that the amplitude of heave acceleration at Model 3 for WR_3 case is generally over predicted. This is caused by the decision of assuming that the heave acceleration RAO at Model 3 equals to the heave acceleration RAO at Model 1, without taking into accounts the hydrodynamic interactions among the three floats. Nonetheless, the trend of the predicted heave acceleration response is found to reasonably fit the experiment data.

Table 5. 6 Correlation coefficient of future responses (based on KF T: 25 s) at Model 2

Case name	Pitch (r_{xy_25})			Heave (r_{xy_25})		
	3 s ahead	8 s ahead	15 s ahead	3 s ahead	8 s ahead	15 s ahead
RF_1	0.958	0.788	0.619	0.975	0.820	0.580
RF_2	0.952	0.821	0.579	0.956	0.792	0.492
RF_3	0.918	0.723	0.558	0.945	0.811	0.587
RF_4	0.951	0.808	0.592	0.964	0.821	0.542
WR_3	Unavailable (see the explanation provided in Sec.5.5)			0.976	0.760	0.602
WR_4				0.985	0.733	0.501
WR_5				0.960	0.751	0.557
WR_6				0.972	0.753	0.561

Table 5. 7 Correlation coefficient of future responses (based on KF T: 25 s) at Model 3

Case name	Vertical acceleration (r_{xy_25})			
	3 s ahead	8 s ahead	12 s ahead	15 s ahead
RF_1	0.988	0.938	0.825	0.764
RF_2	0.867	0.849	0.751	0.613
RF_3	0.917	0.883	0.788	0.681
RF_4	0.978	0.949	0.871	0.824
WR_3	0.951	0.880	0.768	0.667
WR_4	0.881	0.798	0.766	0.635
WR_5	0.934	0.829	0.751	0.647
WR_6	0947	0.858	0.783	0.675

Generally, it can be observed that the future predictable time for responses is found to be longer than the future predictable time for the associated wave. Specifically, the responses at Model 2 and Model 3 can be predicted up to 8 s and 12 s ahead, respectively, for both RF and WR cases. In the previous section, it has been established that the predictable future time at Model 2 for RF and WR are respectively 3 and 5 s. With the same predictable future time of response at Model 2 that is as long as 8 s, the excess duration of predictable future time for the response of RF and WR cases is respectively 5 s and 3 s. Hence, it can be observed that the excess duration for the predictable future time of WR cases is shorter than RF cases. Based on this, it can be concluded the properties of the TFs might be the factor that determine the predictable future time duration of the response, as they are the only additional factor in Equation (5.6) to obtain the response. A longer future response prediction time (compared to the future predictable time of the associated wave) can be achieved if the response amplitude operators (RAO) functions are more significant in the longer wave region. However, if the response characteristics of the models include resonance in the shorter wave region, it is expected that the future predictable time for the response would not increase as much. Nevertheless, this hypothesis needs further verification especially conclusions derived based on the WR cases as for the time being, simulation TFs are incorporated in the Kalman filter algorithm for this model rather than its experiment TFs.

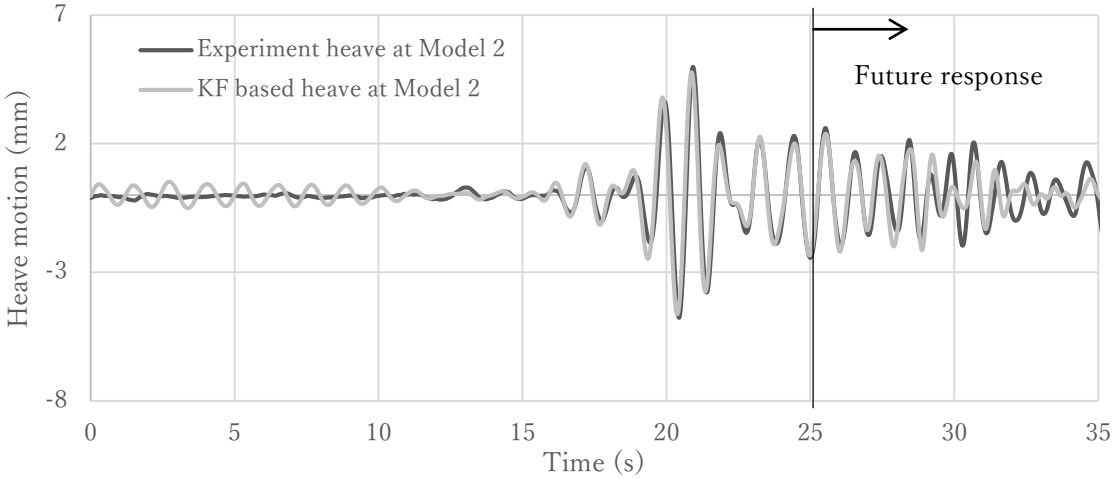

(a)

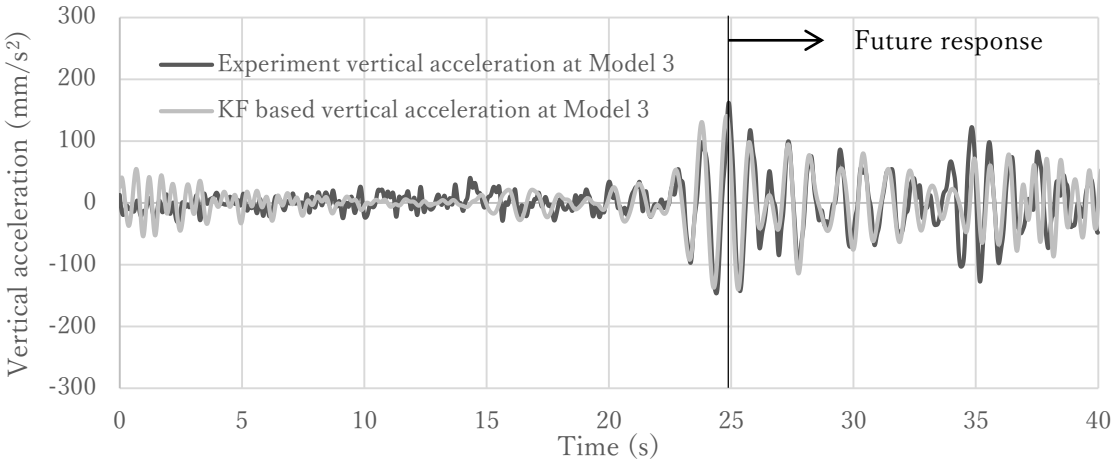

(b)

Figure 5. 15 Experimental vs KF-based response time series for case RF_3; KF T: 25 s (a) Heave at Model 2 (b) Vertical acceleration at Model 3

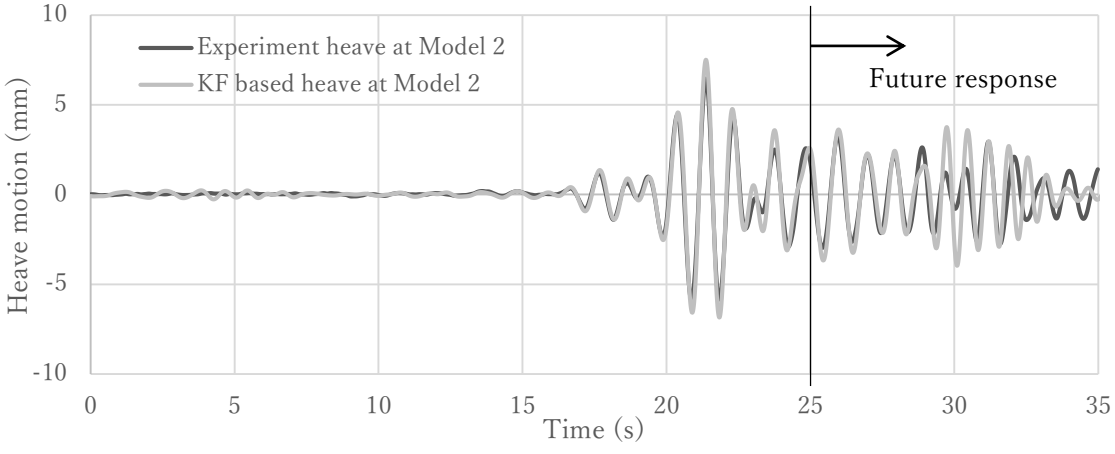

(a)

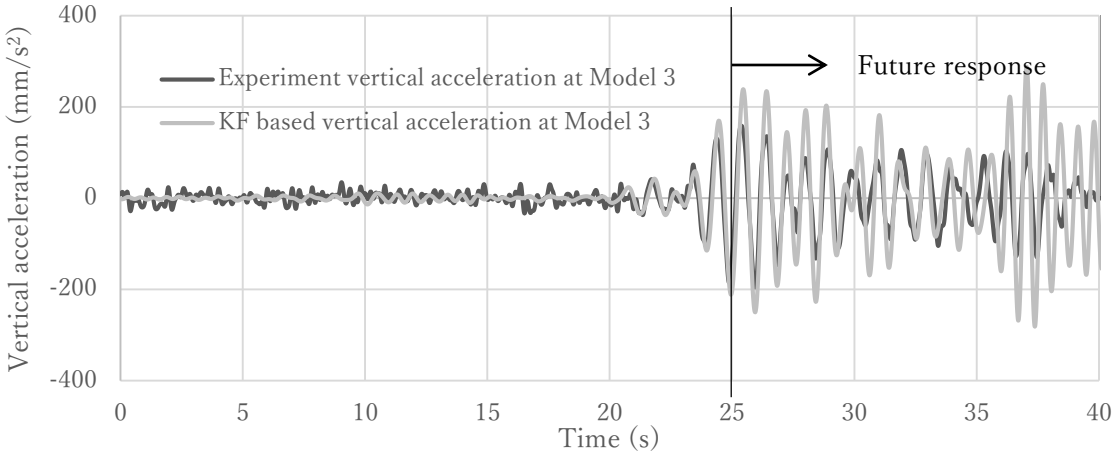

(b)

Figure 5. 16 Experimental vs KF-based response time series for case WR_3; KF T: 25 s (a) Heave at Model 2 (b) Vertical acceleration at Model 3

5.9 Summary

This chapter discusses the results of future wave and response predictions of models located away from a reference point, based on the results of the Kalman filter applied at the reference point. A series of experiments using scaled models in a 2D tank was conducted to validate this method. The experiment is carried out under two different phase, namely phase 1 and phase 2. In phase 1, three identical models with no resonance in their TFs are adopted, while in phase 2, three models with resonance are used. The proposed Kalman filter algorithm accurately identifies the wave profile around a model by analyzing the measured time series of the model's response, both for resonance free model and model with resonance cases. However, accuracy decreases when significant hydrodynamic interactions and reflection waves are present. Moreover, the study confirms that accurate future wave predictions at a specific point can be achieved by extending the identified wave from the reference point when considering spatial distances. It is observed that longer spatial distances result in longer predictable future time. This can be explained by examining the cross-correlation function between waves at the reference point and waves away from it. The slope of maximum values of the impulse response functions may also be used to explain the future predictable time. Future response predictions are also performed based on the previously mentioned future wave predictions. The study reveals that the predictable time for responses exceeds the predictable time for the associated wave input, with its excess duration depends on the response characteristics of the models. However, additional confirmation is required for the findings drawn from phase 2 results. This is due to the decision of utilizing simulation TFs in the Kalman filter algorithm instead of experimental TFs, for the time being.

In summary,

- The proposed Kalman filter accurately identifies the wave profile around the model for both resonance-free and resonance-included cases based on 2D tank experiment data.
- Extending the identified wave from the reference point allows for accurate future wave predictions at specific points, considering spatial distances.
- Longer spatial distances result in longer predictable future time due to the cross-correlation function between waves at the reference point and distant waves.
- Future response predictions are performed based on the future wave predictions, and the predictable time for responses exceeds that of the associated wave input, where the excess duration depends on the response characteristics of the models.

Chapter 6
Conclusions and future works

6.1 Conclusions

This study investigates the feasibility of using the Kalman filter algorithm to predict the future waves and responses using measurement data on multiple floating bodies targeted to be implemented in digital twin system of a wind farm. The prediction is based on the coefficients of elementary waves that constitute the overall wave spectrum. Firstly, the real-time prediction results using Kalman filter based on two different designs of FOWTs are compared, where the main difference lies on the corresponding TFs. Shortly, the first structure has steeper and peakier RAO compared to the second one. The next part of the study proposes a method for predicting future waves and responses of models located away from a reference point, based on the results of the Kalman filter applied at the reference point. Experiment on 2D tank using simplified floating models is conducted to prove the proposed method feasibility. The 2D tank experiments can be further broken down into two phase. In phase 1, resonance free models are adopted, while in phase 2, models with resonance are utilized.

- For the case of wave prediction carried out using FOWT designs, it is consistently found that structure with steeper and pronounced peak in the RAO function gives less accurate wave estimation results. The finding is further solidified when results from 2D tank experiment are considered. Overall, resonance free model exhibit higher accuracy compared to the model with resonance due to the absence of nonlinearity effects in resonance free model.

- Prediction accuracy can be improved by combining different measurement data. However, this should be done with caution as combining different responses to the filter affects observation matrix size that influences the computational time.

- Filtering results based on the simulation and experiment using two FOWT designs point out that nonlinearity from combined loads plays a big role on the prediction results. If the nonlinearity caused by the combined loads is high, the prediction accuracy will be highly affected as well. This finding is valid the other way around. Still, it is foreseen that wave prediction based on Kalman filter should be effective for FOWT. One of the design

introduced in this study is indeed characterized by its peaky resonance and high degree of nonlinearity from combined load. Nevertheless, this is rather an odd design specially crafted for research purpose. The other design, which consistently demonstrates satisfactory accuracy across all case studies, aligns more closely with the commonly preferred response characteristics when designing FOWT.

- The experiments conducted at the 2D tank confirm that accurate future wave predictions at a specific point can be achieved by extending the identified wave from the reference point when considering spatial distances.

- It is observed that longer spatial distances result in longer predictable future time. This can be explained by examining the cross-correlation function between waves at the reference point and waves away from it.

- Lastly, it is found that the predictable time for responses exceeds the predictable time for the associated wave input. This applies to both resonance free models and model with resonance. However, it is observed that the excess duration of the predictable future time of responses on the model with resonance is shorter than the free resonance model.

6.2 Future scopes

The study demonstrates the effectiveness of real-time wave identification around a model using the Kalman filter algorithm. It also successfully predicts future waves and responses for different models located away from the reference model. The findings suggest that implementing this system in a wind farm could optimize the operation and maintenance processes, potentially reducing maintenance costs. Further research is recommended to revalidate the future predictability of responses by considering models with resonance in higher frequency regions. Additionally, improvements in the algorithm, particularly regarding floating body interactions and reflection waves, are necessary to validate the effectiveness of the proposed method. Conducting experiments in a longer tank, such as a towing tank, using less simplified models is suggested to thoroughly examine the interaction between floating bodies, reflection waves, and their impact on prediction results. When it all has been done, then a real scale test at sea is needed, especially to check the assumption that dispersion relations remain constant at all point would still hold true.

Moreover, for practical applications on FOWTs, a thorough analysis is required to determine the appropriate measurement data and location. It is essential to carefully consider these factors when applying the Kalman filter algorithm in real-world scenarios. Short-crested wave cases

should also be investigated since the present investigations basically covers only long-crested wave cases. To achieve this, NK-UTWind needs to be improved. It is noted that Komoriyama (2023) has validated and extended the currently used Kalman filter algorithm to predict short-crested wave using a ship model as the subject structure. However, there is still a need for a dedicated study to assess the feasibility and effectiveness of the Kalman filter algorithm in predicting short-crested waves specifically for FOWT.

Last but not least, it has been proven that Kalman filter is heavily relied on the assumed TFs. Hence, extending the algorithm in a way that it is able to automatically update the TFs based on the input response is proposed. For cases with high nonlinearity, it is suggested to combine Kalman filter—that is light in algorithm, with Neural Network (NN). NN is known to have the ability to handle nonlinear prediction. However, the effectivity is highly dependent on the training data provided.

This page is intentionally left blank

References

4C Offshore. (2023, June 17). Retrieved from https://map.4coffshore.com/

Adilah, A., & Iijima, K. (2021). A Spectral Approach for Efficient Fatigue Damage Evaluation of Floating Support Structure for Offshore Wind Turbine Taking Account of Aerodynamic Coupling Effects. *Journal of Marine Science and Technology*, https://doi.org/10.1007/s00773-021-00841-x.

Al-Ani, M., Belmont, M., & Christmas, J. (2020). Sea Trial on Deterministic Sea Waves Prediction using Wave-Profiling Rasar. *Ocean Engineering, 207*.

Auger, F., Hilairet, M., Guerrero, J. M., Monmasson, E., Orlowska-Kowalska, T., & Katsura, S. (2013). Industrial Applications of the Kalman Filter: A Review. *IEEE Transactions on Industrial Electronics, 60*, 5458-5471.

Belmont, M. R., Horwood, J. M., Thurley, R. W., & Baker, J. (2006). Filters for Linear Sea-Wave Prediction. *Ocean Engineering, 33*, 2332-2351.

Butterfield, S., Musial, W., Jonkman, J., & Sclavounos, P. (2005). Engineering Challenges for Floating Offshore Wind Turbines. *Copenhagen Offshore Wind Conference.* Copenhagen.

Castellà, X. T. (2020). *Operation and Maintenance Costs for Offshore Wind Farm: Analysis and Strategies to Reduce O&M Costs.* Industrial Engineering, BarcelonaTech and NTUST Taiwan: Master Thesis.

Ciuriuc, A., Rapha, J. I., Guanche, R., & Domínguez-García, J. L. (2022). Digital Tools for Floating Offshore Wind Turbines (FOWT): A State of the Art. *Energy Reports, 8*, 1207-1228.

Cristina, A. L., Ahmadreza, V. B., Chi, Y., Sicheng, W., Pan, Y., Brodie, J. F., & Maguire, A. E. (2018). Review and evaluation of wake loss models for wind energy applications. *Appl. Energy*, 1187-1207.

Darlington, S. (1958). Linear Least-Squares Smoothing and Prediction, with Applications. *Bell System Tech. Journal, 37*, 1221-1294.

Davis, M. C., & Zarnick, E. E. (1966). *Testing Ship Models in Transient Waves.* Washington, D.C.: David Taylor Model Basin, Department of the Navy.

Dogariu, L.-M., Benesty, J., Paleologu, C., & Ciochină, S. (2021). An Insightful Overview of the Wiener Filter for System Identification. *Applied Sciences, 11*.

Duan, W., Ma, X., Huang, L., Liu, Y., & Duan, S. (2020). Phase-Resolved Wave Prediction Model for Long-Crest Waves based on Machine Learning. *Computer Methods in Applied Mechanics and Engineering, 372*.

Ellabban, O., Abu-Rub, H., & Blaabjerg, F. (2014). Renewable energy resources: current status, future prospects and their enabling technology. *Renewable and Sustainable Energy Reviews, 39*, 748-764.

Emmanouil, G., Galanis, G., & Kallos, G. (2012). Combination of Statistical Kalman Filters and Data Assimilation for Improving Ocean Waves Analysis and Forecasting. *Ocean Modelling, 59-60*, 11-23.

Esteban, M. D., Diez, J. J., López, J. S., & Negro, V. (2011). Why offshore wind energy? *Renewable Energy, 36*, 444-450.

Esteban, M. D., López-Gutiérrez, J.-S., & Negro, V. (2020). Offshore wind farms. *Journal of Marine Science and Engineering, 8*, 1-2.

Falnes, J. (1995). On Non-Causal Impulse Response Functions Related to Propagating Water Waves. *Applied Ocean Research, 17*(6), 379-389.

Falnes, J., & Kurniawan, A. (2020). *Ocean Waves and Oscillating Systems: Linear Interactions Including Wave-Energy Extraction.* Cambridge University Press.

Glauert, H. (1935). Airplane Propellers. In W. F. Durand, *Aerodynamic Theory* (pp. 169-360). Berlin, Heidelberg: Springer.

Hanaki, T., Takaoka, M., & Minoura, M. (2022). Recursive Analysis of Added Mass, Damping COefficient, and Wave-Exciting Force Using Time-Series Data of Two Dimensional Floating Body's Motion Only. *Applied Ocean Research, 123*.

Hassania, R., Helgadóttir, Á., & Riedel, M. (2023). Iceland wind farm assessment case study and development: An empirical data from wind and wind turbine. *Cleaner Energy Systems*.

Hlophe, T., Wolgamot, H., Kurniawan, A., Taylor, P. H., Orszaghova, J., & Draper, S. (2021). Fast Wave-by-Wave Prediction of Weakly Nonlinear Unidirectional Wave Fields. *Applied Ocean Research, 112*.

Huchet, M., Babarit, A., Ducrozet, G., Gilloteaux, J.-C., & Ferrant, P. (2021). Nonlinear Deterministic Sea Wave Prediction Using Instantaneous Velocity Profiles. *Ocean Engineering, 220*.

Iida, T., & Minoura, M. (2022). Analytical Solution of Impulse Response Function of Finite-Depth Water Waves. *Ocean Engineering, 249*.

Inoue, T. (2021). *風波混合荷重下における FOWT の構造応答予測のための空力評価モデルの開発に関する研究 (Master thesis).* Osaka: Osaka University.

Inoue, T., Adilah, A., Iijima, K., Oh, S., & Suzuki, H. (2020). Discussion on Coupling Effect in Structural Load of FOWT for Condensing Wind and Wave Bins for Spectral Fatigue Analysis. *Journal of Marine Science and Engineering, 8*(11), https://doi.org/10.3390/jmse8110937.

IRENA. (2019). *Future of wind: deployment, investment, technology, grid integration and socio-economic aspects (A Global Energy Transformation Paper).* Abu Dhabi: International Renewable Energy Agency.

Isnaini, R., Toichi, K., Iijima, K., & Tatsumi, A. (2022). Real-Time Prediction of Incoming Wave Profile Surrounding Floating Offshore Wind Turbine using Kalman Filter. *OMAE.* Hamburg.

Isnaini, R., Toichi, K., Tatsumi, A., & Iijima, K. (2022). Real-Time Wave Prediction for Floating Offshore Wind Turbine based on the Kalman Filter. *RENEW2022.* Lisbon.

Jonkman, J. M., & Buhl Jr., M. L. (2005). *FAST User's Guide (Technical Report NREL/TP-500-38230).* Golden, Colorado: National Renewable Energy Laboratory (NREL).

Kalman, R. E. (1960). A New Approach to Linear Filtering and Predictions Problems. *Journal of Basic Engineering, 82*, 35-45.

Kashiwagi, M. (2018). Wave-Body Interaction Theory (Theory of Ship Waves). Osaka: Dept. of NAOE, Osaka University.

Klein, M., Dudek, M., Clauss, G. F., Ehlers, S., Behrendt, J., Hoffman, N., & Onorato, M. (2020). On the Deterministic Prediction of Water Waves. *Fluids, 5*.

Komoriyama, Y. (2023). *Safety monitoring system for ship structures using real-time measurement and*

numerical model (PhD thesis). Osaka: Osaka University.

Lanning, J. H., & Battin, R. H. (1956). *Random Processes in Automatic Control.* New York: McGraw-Hill Book Company, Inc.

Leishman, J. G. (2000). *Principles of Helicopter Aerodynamics.* Cambridge: The Press Syndicate of The University of Cambridge.

Manwell, J. F., McGowan, J. G., & Rogers, A. L. (2004). *Wind Energy Explained: Theory, Design and Application.* Hoboken, New Jersey: Wiley.

Moriarty, P. J., & Hansen, A. C. (2005). *AeroDyn Theory Manual.* Golden: National Renewable Energy Laboratory (NREL).

Morison, J. P., O'Brien, M. P., Johnson, J. W., & Schaaf, S. A. (1950). The Force Exerted by Surface Waves on Piles. *Journal of Petroleum Technology*, 149-154.

Naaijen, P., Van Oosten, K., Roozen, K., & Van 't Veer, R. (2018). Validation of a Deterministic Wave and Ship Motion Prediction System. *International Conference on Offshore Mechanics and Arctic Engineering.* Madrid.

Oh, S., Ishii, K., Iijima, K., & Suzuki, H. (2019). Implementation of Potential Flow Hydrodynamics to Time-Domain Analysis of Flexible Platforms of Floating Offshore Wind Turbines. *Journal of Physics: Conference Series.* Trondheim.

Ørsted. (2023, June 17). *Home page: Hornsea Project*. Retrieved from Hornsea Project Web site: https://hornseaprojects.co.uk/

Papillon, L., Castello, R., & Ringwood, J. V. (2020). Boundary Element and Integral Methods in Potential Flow Theory: A Review with A Focus on Wave Energy Applications. *Journal of Ocean Engineering and Marine Energy*.

Pascoal, R., & Soares, C. G. (2009). Kalman Filtering of Vessel Motions for Ocean Wave directional Spectrum Estimation. *Ocean Engineering, 36*, 477-488.

Pascoal, R., Perera, P., & Soares, C. G. (2017). Estimation of Directional Sea Spectra from Ship Motions in Sea Trials. *Ocean Engineering, 132*, 126-137.

Pinto, J. P., Bernardino, M. C., & Pires Silva, A. (2005). A Kalman Filter Application to A Spectral Wave Model. *Nonlinear Processes in Geophysics, 12*, 775-782.

Ragnarsson, B. F., Oddsson, G. V., Unnthorsson, R., & Hrafnkelsson, B. (2015). Levelized Cost of Energy Analysis of a Wind Power Generation System at Búrfell in Iceland. *Energies*, 9464-9485.

Sánchez, S., López-Gutiérrez, J.-S., Negro, V., & Esteban, M. D. (2019). Foundations in offshore wind farms: evolution, characteristics and range of use. Analysis of main dimensional in monopile foundation. *Journal of Marine Science and Engineering, 7*(441).

Simon, D. (2006). *Optimal State Estimation: Kalman, H-Infinity, and Nonlinear Approaches.* Hoboken, New Jersey: John Wiley & Sons, Inc.

Suzuki, H., Shibata, H., Fujioka, H., Hirabayashi, S., Ishii, K., & Kikuchi, K. (2013). Development and Verification of Analysis Code "UT-Wind" for Rotor-Floater-Mooring Coupled Response of a Floating Offshore Wind Turbine. *Journal of Japanese Society of Naval Architects and Ocean Engineers, 13*, 81-90.

Takata, T., Takaoka, M., Goncalves, R., Houtani, H., Yoshimura, Y., Hara, K., . . . Suzuki, H. (2021). Dynamic Behaviour of A Flexible Multi-COlumn FOWT in Regular Waves. *Journal of Marine Science and Engineering, 9*(2), DOI:10.3390/jmse9020124.

Tan, L. (2008). Digital Signals and Systems. In *Digital Signal Processing: Fundamentals and*

Applications (pp. 57-86). London: Elsevier.

Tanaka, S., Hamamichi, S., Wada, R., Takagi, K., & Imamura, J. (2018). Wave Motion Alert System by Multiple Drones. *OCEANS 2018 MTS/ IEEE.* Charleston.

Tillenburg, D. (2021). *Technical challenges of floating offshore wind turbines—An overview.* FH Münster - University of Applied Sciences.

Wang, M., Wang, C., Hnydiuk-Stefan, A., Feng, S., Atilla, I., & Li, Z. (2021). Recent Progress on Reliability Analysis of Offshore Wind Turbine Support Structures Considering Digital Twin Solutions. *Ocean Engineering, 232*, 109168.

Wiener, N. (1949). *The Extrapolation, Interpolation, and Smoothing of Stationary Time Series.* New York: John Wiley & Sons, Inc.

Wu, X., Hub, Y., Li, Y., Yang, J., Duan, L., Wang, T., . . . Liao, S. (2019). Foundation of offshore wind turbines: A review. *Renewable and Sustainable Energy Reviews, 104*, 379-393.

Zadeh, L. A., & Ragazzini, J. R. (1950). An Extension of Wiener's Theory of Prediction. *Journal of Applied Physics, 21*, 645-655.

池田, 良., 梅田, 直., 慎, 燦., & 内藤, 林. (2013). *船舶海洋工学シリーズ 5　船体運動　耐航性能　初級編 (Sec. 8.2.4).* 東京都: 株式会社　成山堂書店.

Acknowledgements

I wish to express my sincere appreciation and deepest gratitude to my supervisor, Iijima Kazuhiro-Sensei, who has inspired me with his ingenuity, work ethic, and kindness. Without his persistent help, the goal of this research would not have been realized. I'd also like to deliver my appreciation for all the members of Structural Integrity Subarea laboratory, Osaka University, for all their help during my Doctoral degree completion, especially K. Tsukamoto, B.Y. Xie, K. Toichi, A. Yoshioka, and Y. Watanabe for tagging along during my experiment and put up with my leadership style that I would only be able to describe as ～SUPER-DUPER-EXTRA-CHAOTIC～. Lastly, I wish to acknowledge the support and great love of my friends, and the one and only, Fabian, that has stuck with me since forever and has chosen to stick around despite all the hurdles (y'know, Your Majesty Corona and panic attacks and stuff). They kept me going on and this work would not have been possible without their inputs.

Osaka, June 2023
Rodhiatul Isnaini

"Oh no. This again?" –*me, in the middle of writing this dissertation*

This page is intentionally left blank

Appendix 1

Table of regular wave cases for model with resonance

Case no.	Wave circular frequency (rad/s)	Wave period (s)	Measured wave height at Model 1 (mm)
1	4.83	1.30	3.14
2	4.83	1.30	7.47
3	5.03	1.25	6.41
4	5.24	1.20	10.28
5	5.24	1.20	12.16
6	5.46	1.15	8.33
7	5.46	1.15	10.34
8	5.46	1.15	12.11
9	5.71	1.10	8.73
10	5.71	1.10	8.89
11	5.71	1.10	11.25
12	5.71	1.10	13.38
13	5.98	1.05	8.83
14	5.98	1.05	10.88
15	6.04	1.04	8.04
16	6.04	1.04	9.98
17	6.10	1.03	6.31
18	6.10	1.03	8.10
19	6.22	1.01	6.74
20	6.22	1.01	8.33
21	6.28	1.00	9.47
22	6.41	0.98	8.97
23	6.41	0.98	11.24
24	6.61	0.95	8.52
25	6.61	0.95	8.41
26	6.61	0.95	10.37
27	6.76	0.93	7.16
28	6.76	0.93	9.05

29	6.83	0.92	6.92
30	6.83	0.92	9.57
31	6.83	0.92	12.02
32	6.98	0.90	9.03
33	6.98	0.90	12.60
34	7.06	0.89	9.74
35	7.06	0.89	13.41
36	7.22	0.87	8.26
37	7.22	0.87	11.55
38	7.31	0.86	6.94
39	7.31	0.86	9.24
40	7.39	0.85	6.98
41	7.39	0.85	9.95
42	7.57	0.83	9.88
43	7.57	0.83	14.67
44	7.66	0.82	11.95
45	7.66	0.82	16.17
46	7.85	0.80	6.03
47	7.85	0.80	7.58
48	7.85	0.80	11.51
49	7.85	0.80	14.77
50	8.06	0.78	8.58
51	8.06	0.78	11.04
52	8.06	0.78	13.02
53	8.16	0.77	8.19
54	8.16	0.77	9.96
55	8.16	0.77	11.41
56	8.16	0.77	14.04
57	8.38	0.75	6.54
58	8.38	0.75	8.22
59	8.38	0.75	9.65
60	8.49	0.74	6.83
61	8.49	0.74	7.57
62	8.49	0.74	10.16
63	8.61	0.73	5.96
64	8.61	0.73	7.00
65	8.61	0.73	12.35
66	8.85	0.71	5.21

67	8.85	0.71	6.42
68	8.85	0.71	6.76
69	8.85	0.71	11.39
70	8.98	0.70	5.33
71	8.98	0.70	6.38
72	8.98	0.70	7.77
73	9.24	0.68	3.64
74	9.24	0.68	14.03
75	9.24	0.68	19.27
76	9.67	0.65	5.56
77	10.47	0.60	16.92

This page is intentionally left blank

Appendix 2

Transfer functions

Semisub-A

All TFs are calculated based on 1 m wave amplitude, and 10 m/s steady wind for AD cases

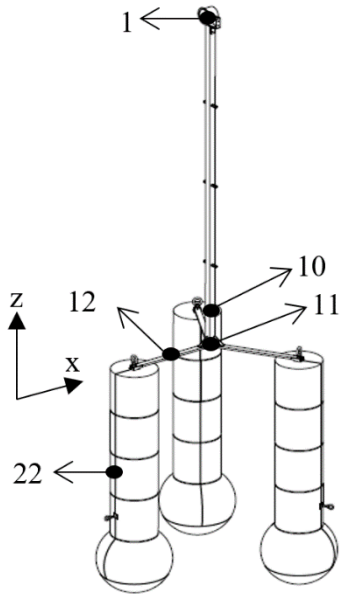

Table 1. Heave node 1

No wind condition (A-1NW)			Combined load condition (A-1AD)		
Frequency (rad/s)	RAO (m/m)	Phase (rad)	Frequency (rad/s)	RAO (m/m)	Phase (rad)
1.26933	0.002988	0.8219	1.26933	0.006245	0.3054
0.987301	0.016522	0.4076	0.987301	0.021111	-3.0299
0.807815	0.031488	0.1998	0.807815	0.036076	-1.83498
0.683549	0.14089	-2.18246	0.683549	0.069212	-1.2074
0.592362	0.11531	0.2673	0.592362	0.12377	-0.7666
0.522684	0.44965	-3.9465	0.522684	0.47677	-4.9795
0.467673	0.21069	3.1895	0.467673	0.21436	2.20648
0.444293	0.35373	-3.0761	0.444293	0.35288	-3.9484

0.423139	0.59795	3.22778	0.423139	0.59639	2.47655
0.386348	1.8637	3.4431	0.386348	1.8429	2.8972
0.355424	4.0506	-1.06781	0.355424	4.1965	-1.26533
0.3291	1.7013	-0.1204	0.3291	1.6986	-0.60101
0.306407	1.1674	-0.0438	0.306407	1.1546	-0.42
0.296195	1.283	-0.035	0.296195	1.2828	-0.38826
0.26926	1.1195	-0.0223	0.26926	1.1169	-0.3072

Table 2. Strain node 10

No wind condition (A-2NW)			Combined load condition (A-2AD)		
Frequency (rad/s)	RAO (μ/m)	Phase (rad)	Frequency (rad/s)	RAO (μ/m)	Phase (rad)
1.2693	12.674	-0.60963	1.2693	13.321	-0.22861
0.9873	4.519	0.6924	0.9873	5.4503	0.22579
0.80782	5.8621	-4.7279	0.80782	6.0941	2.267
0.68355	11.572	-4.3989	0.68355	7.4901	0.051246
0.59236	9.1226	-5.0559	0.59236	9.2908	-0.09139
0.52268	10.812	-4.7451	0.52268	10.594	0.48533
0.46767	9.7704	1.6086	0.46767	9.7427	-2.3237
0.44429	11.745	-4.6722	0.44429	11.813	0.94181
0.42314	13.093	1.6475	0.42314	13.109	-2.0404
0.38635	15.204	1.6901	0.38635	14.355	1.8085
0.35542	54.566	-3.7056	0.35542	37.285	-1.8212
0.3291	19.85	-1.8768	0.3291	18.384	0.19377
0.30641	7.44	4.6308	0.30641	7.3551	-2.4843
0.2962	6.7404	-1.5989	0.2962	6.5043	-2.3615
0.26926	3.3666	-1.5589	0.26926	3.2842	0.95545

Table 3. Strain node 12

No wind condition (A-3NW)			Combined load condition (A-3AD)		
Frequency (rad/s)	RAO (μ/m)	Phase (rad)	Frequency (rad/s)	RAO (μ/m)	Phase (rad)
1.2693	10.865	-2.2429	1.2693	10.533	-1.88
0.9873	52.831	-2.6127	0.9873	52.831	0.159
0.80782	84.397	0.34783	0.80782	85.061	1.21
0.68355	220.63	0.32799	0.68355	223.95	1.86
0.59236	230.93	-0.31619	0.59236	242.23	1.57

0.52268	551.57	-0.7209	0.52268	548.25	1.45
0.46767	109.98	0.16217	0.46767	111.31	-0.629
0.44429	87.055	0.25209	0.44429	86.39	2.68
0.42314	67.451	0.35419	0.42314	65.79	-0.273
0.38635	39.208	0.721	0.38635	24.854	0.368
0.35542	73.764	-0.57988	0.35542	62.467	-2.09
0.3291	32.928	1.7121	0.3291	27.778	0.602
0.30641	15.451	-0.92578	0.30641	15.451	-0.656
0.2962	15.484	-0.83424	0.2962	14.022	-1.54
0.26926	9.4697	2.4695	0.26926	9.2039	1.88

Table 4. Pitch node 22

No wind condition (A-3NW)			Combined load condition (A-3AD)		
Frequency (rad/s)	RAO (deg/m)	Phase (rad)	Frequency (rad/s)	RAO (deg/m)	Phase (rad)
1.26933	0.209351	-0.33884	1.26933	0.224314	0.064821
0.987301	0.379869	-2.56664	0.987301	0.416914	0.187386
0.807815	0.538244	0.776101	0.807815	0.572535	1.602956
0.683549	2.141435	1.896905	0.683549	1.21612	2.198914
0.592362	1.222211	-0.93349	0.592362	1.263884	0.95918
0.522684	3.605939	2.199538	0.522684	3.554351	1.226273
0.467673	1.169565	-1.01543	0.467673	1.20246	-1.75012
0.444293	1.414313	1.945494	0.444293	1.469441	1.331117
0.423139	1.688346	-1.27239	0.423139	1.741781	-1.75282
0.386348	2.287782	1.793195	0.386348	2.27304	1.975879
0.355424	9.716926	-0.49503	0.355424	6.453521	-1.70238
0.3291	4.021192	1.28165	0.3291	3.701391	0.290011
0.306407	1.721911	-1.66308	0.306407	1.694273	-2.40487
0.296195	1.657377	-1.61619	0.296195	1.599113	-2.28408
0.26926	0.981864	1.555734	0.26926	0.958489	1.017632

Table 5. Heave acceleration node 1

No wind condition (A-5NW)		
Frequency (rad/s)	RAO (m.rad2/s2.m)	Phase (rad)
1.2693	0.004843	-2.319
0.9873	0.016093	-2.7338

0.80782	0.020547	0.19989
0.68355	0.029314	0.13604
0.59236	0.040455	0.2674
0.52268	0.12284	-0.80496
0.46767	0.046084	0.04824
0.44429	0.069826	0.065193
0.42314	0.10709	0.086249
0.38635	0.27818	0.30162
0.35542	0.51173	-1.0678
0.3291	0.18424	-0.12077
0.30641	0.10961	-0.04428
0.2962	0.11253	-0.03504
0.26926	0.08117	-0.02276

Table 6. Pitch acceleration node 22

No wind condition (A-6NW)		
Frequency (rad/s)	RAO (deg.rad2/s2.m)	Phase (rad)
1.2693	0.3288	-0.31182
0.9873	0.37036	-2.5665
0.80782	0.35124	0.77576
0.68355	0.54728	0.68595
0.59236	0.42879	-0.93343
0.52268	0.98529	2.1996
0.46767	0.25574	-1.015
0.44429	0.27934	1.9457
0.42314	0.30246	-1.2722
0.38635	0.34174	1.7928
0.35542	1.2279	-0.49527
0.3291	0.43609	1.2795
0.30641	0.16208	-1.6651
0.2962	0.14548	-1.6161
0.26926	0.071103	1.5562

Semisub-B

All TFs are calculated based on 1 m wave amplitude, and 10 m/s steady wind for AD cases

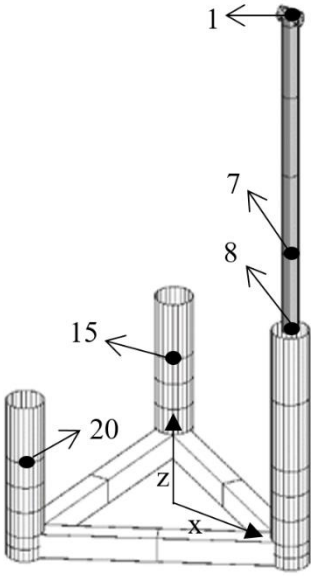

Table 7. Strain node 8

No wind condition (B-1NW)			Combined load condition (B-1AD)		
Frequency (rad/s)	RAO (μ /m)	Phase (rad)	Frequency (rad/s)	RAO (μ /m)	Phase (rad)
0.16	3.328580553	-0.60455	0.16	9.772101	-0.65932
0.17	4.308732603	-0.52595	0.17	10.93868	-0.44039
0.18	5.405438063	-0.44736	0.18	12.51782	-0.22146
0.19	6.724209653	-0.39763	0.19	14.36825	-0.03724
0.2	8.370560096	-0.34791	0.2	16.34869	0.146983
0.21	10.45285492	-0.2768	0.21	18.35868	0.281644
0.22	13.09087091	-0.20569	0.22	20.46091	0.416306
0.23	16.38006307	-0.10737	0.23	22.69569	0.542329
0.24	20.30718809	-0.00905	0.24	24.85048	0.668353
0.25	24.71005857	0.156204	0.25	26.76462	0.802251
0.26	28.93940905	0.321454	0.26	28.73779	0.93615
0.27	32.29265703	0.489879	0.27	30.99501	1.021756
0.28	34.34103018	0.658304	0.28	33.00233	1.107362
0.29	34.88476654	0.79073	0.29	34.19514	1.180891
0.3	34.36633584	0.923155	0.3	34.64519	1.25442
0.3225	31.63930125	1.031642	0.3225	34.03442	1.320304
0.345	28.65366427	1.140129	0.345	32.8417	1.386188

0.3675	26.9087242	1.169527	0.3675	32.38411	1.515702
0.39	25.63781288	1.198925	0.39	31.20813	1.645217
0.4125	23.80480153	1.134421	0.4125	27.79629	1.621665
0.435	21.56168618	1.069917	0.435	23.14587	1.598114
0.4575	19.26212879	1.051813	0.4575	18.55095	1.675285
0.48	16.87833001	1.033709	0.48	13.97787	1.752455
0.5025	14.29701475	0.977801	0.5025	9.284421	1.795824
0.525	11.44446608	0.921893	0.525	5.221754	1.839192
0.5475	8.326916064	0.684444	0.5475	2.758481	-0.04679
0.57	5.23083454	0.446996	0.57	2.839632	-1.93277
0.5925	2.750917213	-0.67666	0.5925	5.868939	-1.72521
0.615	2.434525493	-1.80032	0.615	10.10854	-1.51765
0.6375	5.376060242	-2.1931	0.6375	13.76751	-1.7132
0.66	9.90541444	-2.58588	0.66	16.9844	-1.90875
0.6825	14.13422112	-2.78646	0.6825	20.24422	-2.1089
0.705	18.06558141	-2.98704	0.705	23.48863	-2.30905
0.7275	22.07443129	-2.97777	0.7275	26.55955	-2.18471
0.75	26.13157797	-2.9685	0.75	29.44347	-2.06037
0.7725	30.11229512	-0.16012	0.7725	32.17152	-2.49762
0.795	33.91385101	2.648253	0.795	34.80884	-2.93487
0.8175	37.45471615	2.621219	0.8175	37.39238	-2.86146
0.84	40.7161756	2.594185	0.84	39.81238	-2.78805
0.8625	43.67495201	2.445795	0.8625	41.91531	-2.89663
0.885	46.22670391	2.297404	0.885	43.51936	-3.0052
0.9075	48.27558998	2.290004	0.9075	44.49239	-2.86588
0.93	49.84083364	2.282603	0.93	44.92918	-2.72657
0.9525	50.96001764	1.657506	0.9525	45.01748	-0.43036
0.975	51.62909745	1.032409	0.975	45.0901	1.865842
0.9975	51.84259259	1.028211	0.9975	45.32087	2.060939
1.02	51.63090609	1.024013	1.02	45.1026	2.256036
1.0425	51.05830405	0.768363	1.0425	43.86235	2.068775
1.065	50.28862134	0.512712	1.065	41.94493	1.881513
1.0875	49.53864894	0.136321	1.0875	39.88268	1.52098
1.11	49.13743363	-0.24007	1.11	38.04029	1.160447
1.1325	49.39549551	-0.56377	1.1325	36.69097	0.886645
1.155	50.43699237	-0.88746	1.155	35.90985	0.612843
1.1775	52.3394914	-0.93528	1.1775	35.72252	0.773023
1.2	55.18055979	-0.98309	1.2	36.15458	0.933202

Table 8. Strain node 20

No wind condition (B-2NW)			Combined load condition (B-2AD)		
Frequency (rad/s)	RAO (μ /m)	Phase (rad)	Frequency (rad/s)	RAO (μ /m)	Phase (rad)
0.16	0.161363	-1.69197	0.16	0.981092	3.077901
0.17	0.174034	-1.50527	0.17	0.936422	3.055319
0.18	0.19489	-1.31856	0.18	0.886374	3.032738
0.19	0.22607	-1.14078	0.19	0.834884	2.992742
0.2	0.269712	-0.963	0.2	0.785888	2.952746
0.21	0.329315	-0.81555	0.21	0.741951	2.894588
0.22	0.413823	-0.6681	0.22	0.700155	2.83643
0.23	0.536504	-0.54132	0.23	0.655803	2.841179
0.24	0.722474	-0.41453	0.24	0.602568	2.845929
0.25	0.981703	-0.22354	0.25	0.535315	2.915757
0.26	1.251751	-0.03254	0.26	0.455311	2.985585
0.27	1.461028	0.194644	0.27	0.372652	2.913348
0.28	1.573789	0.421828	0.28	0.326347	2.84111
0.29	1.577806	0.558099	0.29	0.343494	2.614644
0.3	1.519087	0.69437	0.3	0.37465	2.388178
0.3225	1.370831	0.699805	0.3225	0.337143	0.817982
0.345	1.298653	0.70524	0.345	0.420579	-0.75221
0.3675	1.353133	0.712472	0.3675	0.875324	-0.00915
0.39	1.438919	0.719704	0.39	1.364362	0.733914
0.4125	1.456732	0.5983	0.4125	1.530113	0.795828
0.435	1.437524	0.476895	0.435	1.520101	0.857742
0.4575	1.43125	0.435602	0.4575	1.546219	0.906015
0.48	1.433633	0.39431	0.48	1.572718	0.954288
0.5025	1.43121	0.294847	0.5025	1.528363	0.835916
0.525	1.427996	0.195385	0.525	1.447623	0.717544
0.5475	1.430104	-0.13813	0.5475	1.380607	0.262852
0.57	1.434548	-0.47164	0.57	1.334293	-0.19184
0.5925	1.439441	-0.48201	0.5925	1.306137	-0.18251
0.615	1.456379	-0.49239	0.615	1.298648	-0.17318
0.6375	1.497521	-0.86893	0.6375	1.315558	-0.53784
0.66	1.563775	-1.24547	0.66	1.36042	-0.90251
0.6825	1.653574	-1.62593	0.6825	1.43723	-1.26812
0.705	1.766684	-2.00639	0.705	1.551937	-1.63372

0.7275	1.903685	-2.03516	0.7275	1.70775	-1.64258
0.75	2.067065	-2.06394	0.75	1.894964	-1.65144
0.7725	2.257932	0.508743	0.7725	2.103849	-2.19211
0.795	2.469959	3.081423	0.795	2.337502	-2.73278
0.8175	2.696066	3.040987	0.8175	2.598142	-2.73564
0.84	2.933586	3.000551	0.84	2.871654	-2.73851
0.8625	3.174236	2.792784	0.8625	3.139432	-2.9083
0.885	3.382857	2.585016	0.885	3.381242	-3.07809
0.9075	3.534291	2.63588	0.9075	3.580951	-2.98895
0.93	3.670259	2.686745	0.93	3.740466	-2.89981
0.9525	3.832693	1.760532	0.9525	3.871372	-0.64798
0.975	3.99751	0.834319	0.975	4.005916	1.603863
0.9975	4.12783	0.955712	0.9975	4.161898	1.764009
1.02	4.201613	1.077106	1.02	4.278653	1.924154
1.0425	4.208004	0.825505	1.0425	4.297957	1.710771
1.065	4.166055	0.573904	1.065	4.249816	1.497387
1.0875	4.100426	0.168563	1.0875	4.180971	1.129087
1.11	4.0283	-0.23678	1.11	4.116875	0.760787
1.1325	3.958347	-0.53128	1.1325	4.072187	0.500836
1.155	3.872666	-0.82579	1.155	4.03969	0.240886
1.1775	3.746712	-0.69149	1.1775	4.006698	0.420806
1.2	3.555944	-0.55718	1.2	3.960525	0.600727

Table 9. Pitch node 22

No wind condition (B-3NW)		
Frequency (rad/s)	RAO (deg/m)	Phase (rad)
0.16	0.266901	-1.47727
0.17	0.292592	-1.42379
0.18	0.323297	-1.3703
0.19	0.358642	-1.31143
0.2	0.398251	-1.25255
0.21	0.442319	-1.17658
0.22	0.493329	-1.10062
0.23	0.553005	-0.97749
0.24	0.617732	-0.85436
0.25	0.680198	-0.66533

0.26	0.723621	-0.4763
0.27	0.732712	-0.28375
0.28	0.707612	-0.09119
0.29	0.654447	0.067349
0.3	0.587853	0.225891
0.3225	0.446233	0.383078
0.345	0.335447	0.540264
0.3675	0.263199	0.689351
0.39	0.212107	0.838438
0.4125	0.163854	0.965207
0.435	0.121482	1.091977
0.4575	0.09191	1.425666
0.48	0.076224	1.759354
0.5025	0.073357	2.116126
0.525	0.079476	2.472898
0.5475	0.090318	2.52285
0.57	0.102677	2.572801
0.5925	0.114132	2.73513
0.615	0.124353	2.897458
0.6375	0.133404	2.804615
0.66	0.140838	2.711771
0.6825	0.146306	2.603773
0.705	0.150354	2.495775
0.7275	0.153556	2.571342
0.75	0.155687	2.646908
0.7725	0.156486	2.369058
0.795	0.156334	2.091208
0.8175	0.155671	2.109186
0.84	0.154534	2.127165
0.8625	0.152844	2.012826
0.885	0.15048	1.898487
0.9075	0.1474	1.911937
0.93	0.143925	1.925387
0.9525	0.140433	1.308163
0.975	0.137174	0.690938
0.9975	0.134335	0.680281
1.02	0.131988	0.669623
1.0425	0.130275	0.40839

1.065	0.129731	0.147157
1.0875	0.130862	-0.21925
1.11	0.133662	-0.58565
1.1325	0.137936	-0.87134
1.155	0.143248	-1.15703
1.1775	0.149098	-1.15409
1.2	0.15499	-1.15114

Resonance free model (RF model)

TFs are combined between simulation and experiment. The experiment TFs are given in the range of 4.83 until 10.47 rad/s.

Table 10. TFs at Model 1

Frequency (rad/s)	Wave number (rad/s)	RAO Pitch (rad/kA)	Phase Pitch (rad)	RAO Heave (mm/mm)	Phase Heave (rad)
3	1.615	1.03	1.568842	0.9762	-0.00061
3.2	1.715	1.03	1.568423	0.9732	-0.00073
3.4	1.865	1.029	1.567708	0.9682	-0.00094
3.6	1.995	1.029	1.566975	0.9635	-0.00115
3.8	2.129	1.028	1.566085	0.9582	-0.00138
4	2.269	1.027	1.565037	0.9524	-0.00161
4.2	2.412	1.026	1.563781	0.946	-0.00185
4.4	2.56	1.025	1.562315	0.9389	-0.00208
4.6	2.715	1.024	1.560569	0.9309	-0.00229
4.8	2.875	1.022	1.558527	0.9222	-0.00244
4.833219	2.902	1.187024	1.359693	1.152726	-0.12659
5.026548	3.064	1.104104	1.164803	1.041987	-0.2585
5.235988	3.247	1.053946	1.101703	0.961179	-0.21605
5.463639	3.456	0.914222	1.534093	0.828377	0.16311
5.711987	3.695	0.955919	1.000543	0.862631	-0.38509
5.983986	3.972	1.114268	1.208443	0.997798	-0.2181
6.283185	4.296	1.253377	1.121643	1.134591	-0.33498
6.613879	4.68	1.122564	1.377693	0.994205	-0.26841
6.981317	5.139	1.000368	1.281173	0.844097	-0.35956
7.391983	5.694	0.979204	1.377913	0.74671	-0.28609
7.853982	6.372	1.006539	2.219316	0.860647	0.244424

8.37758	7.206	0.961928	2.015943	0.659462	0.05017
8.975979	8.244	0.741425	2.494013	0.547764	0.3891
9.666439	9.544	0.511229	2.427578	0.394922	0.194985
10.47198	11.194	0.288657	2.738093	0.232289	0.1594
10.6	11.468	0.3713	1.462447	0.2863	0.682284
10.8	11.904	0.3396	1.499483	0.2687	0.756007
11	12.35	0.3102	1.542208	0.2522	0.833413
11.2	12.801	0.283	1.590606	0.2368	0.91457
11.4	13.262	0.2581	1.644415	0.2223	0.999219
11.6	13.731	0.2353	1.70346	0.2088	1.087306
11.8	14.208	0.2146	1.767548	0.1962	1.178709
12	14.699	0.1954	1.837379	0.1842	1.27458
13	17.2449	0.124	2.249364	0.136	1.794601
14	20	0.07984	2.761915	0.1015	2.389217
15	22.95918	0.06394	3.063613	0.08756	2.725944
16	26.12245	0.03496	-2.24676	0.05845	-2.5057

Table 11. TFs at Model 2

Frequency (rad/s)	Wave number (rad/m)	RAO Pitch (rad/kA)	Phase Pitch (rad)	RAO Heave (mm/mm)	Phase Heave (rad)
3	1.615	1.03	1.568842	0.9762	-0.00061
3.2	1.715	1.03	1.568423	0.9732	-0.00073
3.4	1.865	1.029	1.567708	0.9682	-0.00094
3.6	1.995	1.029	1.566975	0.9635	-0.00115
3.8	2.129	1.028	1.566085	0.9582	-0.00138
4	2.269	1.027	1.565037	0.9524	-0.00161
4.2	2.412	1.026	1.563781	0.946	-0.00185
4.4	2.56	1.025	1.562315	0.9389	-0.00208
4.6	2.715	1.024	1.560569	0.9309	-0.00229
4.8	2.875	1.022	1.558527	0.9222	-0.00244
4.833219	2.902	1.28E+00	1.57E+00	1.09E+00	5.16E-01
5.026548	3.064	8.39E-01	1.37E+00	1.15E+00	-7.12E-01
5.235988	3.247	9.05E-01	1.42E+00	9.72E-01	5.88E-02
5.463639	3.456	8.98E-01	1.93E+00	7.10E-01	2.73E-01
5.711987	3.695	9.07E-01	1.60E+00	8.01E-01	1.15E-01
5.983986	3.972	1.01E+00	1.73E+00	9.32E-01	8.60E-02
6.283185	4.296	1.15E+00	1.56E+00	1.02E+00	-3.18E-02

6.613879	4.68	1.05E+00	1.66E+00	9.25E-01	6.41E-02
6.981317	5.139	8.79E-01	1.64E+00	7.26E-01	4.25E-02
7.391983	5.694	8.18E-01	2.08E+00	6.67E-01	3.76E-01
7.853982	6.372	9.79E-01	2.44E+00	6.90E-01	6.26E-01
8.37758	7.206	7.11E-01	2.07E+00	5.19E-01	2.23E-01
8.975979	8.244	5.28E-01	2.34E+00	3.65E-01	3.26E-01
9.666439	9.544	2.67E-01	2.43E+00	1.92E-01	2.21E-01
10.47198	11.194	2.00E-01	2.09E+00	1.60E-01	-2.79E-01
10.6	11.468	0.3713	1.462447	0.2863	0.682284
10.8	11.904	0.3396	1.499483	0.2687	0.756007
11	12.35	0.3102	1.542208	0.2522	0.833413
11.2	12.801	0.283	1.590606	0.2368	0.91457
11.4	13.262	0.2581	1.644415	0.2223	0.999219
11.6	13.731	0.2353	1.70346	0.2088	1.087306
11.8	14.208	0.2146	1.767548	0.1962	1.178709
12	14.699	0.1954	1.837379	0.1842	1.27458
13	17.2449	0.124	2.249364	0.136	1.794601
14	20	0.07984	2.761915	0.1015	2.389217
15	22.95918	0.06394	3.063613	0.08756	2.725944
16	26.12245	0.03496	-2.24676	0.05845	-2.5057

Table 12. TFs at Model 3

Frequency (rad/s)	Wave number (rad/m)	RAO Heave acc (mm.rad2/mm.s2)	Phase Heave acc (rad)
3	1.615	8.7858	-0.00061
3.2	1.715	9.965568	-0.00073
3.4	1.865	11.19239	-0.00094
3.6	1.995	12.48696	-0.00115
3.8	2.129	13.83641	-0.00138
4	2.269	15.2384	-0.00161
4.2	2.412	16.68744	-0.00185
4.4	2.56	18.1771	-0.00208
4.6	2.715	19.69784	-0.00229
4.8	2.875	21.24749	-0.00244
4.833219	2.902	3.54E+01	0.5162
5.026548	3.064	2.47E+01	-0.71197
5.235988	3.247	1.67E+01	0.05876

5.463639	3.456	3.00E+01	0.2732
5.711987	3.695	2.71E+01	0.11505
5.983986	3.972	2.19E+01	0.08598
6.283185	4.296	4.59E+01	-0.03181
6.613879	4.68	3.10E+01	0.06408
6.981317	5.139	3.16E+01	0.042535
7.391983	5.694	3.15E+01	0.37601
7.853982	6.372	3.28E+01	0.625985
8.37758	7.206	2.70E+01	0.22322
8.975979	8.244	2.04E+01	0.325785
9.666439	9.544	1.10E+01	0.2211
10.47198	11.194	7.55E+00	-0.2785
10.6	11.468	32.16867	0.682284
10.8	11.904	31.34117	0.756007
11	12.35	30.5162	0.833413
11.2	12.801	29.70419	0.91457
11.4	13.262	28.89011	0.999219
11.6	13.731	28.09613	1.087306
11.8	14.208	27.31889	1.178709
12	14.699	26.5248	1.27458
13	17.2449	22.984	1.794601
14	20	19.894	2.389217
15	22.95918	19.701	2.725944
16	26.12245	14.9632	-2.5057

Model with resonance (WR model)

Simulated TFs are assumed.

Table 13. TFs at Model 1 and Model 2

Frequency (rad/s)	RAO Heave (mm/mm)	Phase Heave (rad)
3	1.01	-0.0722
3.2	1.01	-0.0834
3.4	1.01	-0.0956
3.6	1.01	-0.109
3.8	1.02	-0.125

4	1.02	-0.141
4.2	1.02	-0.159
4.4	1.03	-0.178
4.6	1.03	-0.2
4.8	1.04	-0.225
5	1.04	-0.251
5.2	1.05	-0.278
5.4	1.06	-0.308
5.6	1.07	-0.342
5.8	1.08	-0.381
6	1.09	-0.425
6.2	1.11	-0.466
6.4	1.13	-0.513
6.6	1.15	-0.565
6.8	1.18	-0.625
7	1.21	-0.697
7.2	1.26	-0.771
7.4	1.31	-0.846
7.6	1.37	-0.934
7.8	1.44	-1.04
8	1.53	-1.16
8.2	1.61	-1.32
8.4	1.72	-1.49
8.6	1.84	-1.69
8.8	1.92	-1.94
9	1.91	-2.22
9.2	1.8	-2.51
9.4	1.61	-2.77
9.6	1.39	-3
9.8	1.18	3.06
10	0.99	2.89
10.2	0.839	2.75
10.4	0.709	2.62
10.6	0.608	2.52
10.8	0.527	2.43
11	0.46	2.35
11.2	0.4	2.28
11.4	0.347	2.22

11.6	0.304	2.16
11.8	0.266	2.1
12	0.232	2.05

Table 14. TFs at Model 3

Frequency (rad/s)	RAO Heave acc (mm.rad2/mm.s2)	Phase Heave acc (rad)
3	9.09	-0.0722
3.2	10.3424	-0.0834
3.4	11.6756	-0.0956
3.6	13.0896	-0.109
3.8	14.7288	-0.125
4	16.32	-0.141
4.2	17.9928	-0.159
4.4	19.9408	-0.178
4.6	21.7948	-0.2
4.8	23.9616	-0.225
5	26	-0.251
5.2	28.392	-0.278
5.4	30.9096	-0.308
5.6	33.5552	-0.342
5.8	36.3312	-0.381
6	39.24	-0.425
6.2	42.6684	-0.466
6.4	46.2848	-0.513
6.6	50.094	-0.565
6.8	54.5632	-0.625
7	59.29	-0.697
7.2	65.3184	-0.771
7.4	71.7356	-0.846
7.6	79.1312	-0.934
7.8	87.6096	-1.04
8	97.92	-1.16
8.2	108.2564	-1.32
8.4	121.3632	-1.49
8.6	136.0864	-1.69

8.8	148.6848	-1.94
9	154.71	-2.22
9.2	152.352	-2.51
9.4	142.2596	-2.77
9.6	128.1024	-3
9.8	113.3272	3.06
10	99	2.89
10.2	87.28956	2.75
10.4	76.68544	2.62
10.6	68.31488	2.52
10.8	61.46928	2.43
11	55.66	2.35
11.2	50.176	2.28
11.4	45.09612	2.22
11.6	40.90624	2.16
11.8	37.03784	2.1
12	33.408	2.05